AN ACTIVE STIRLING THERMOCOMPRESSOR: DYNAMIC MODELING AND CONTROL

By

Benjamin Seth Thomas

Dissertation

Submitted to the Faculty of the

Graduate School of Vanderbilt University

in partial fulfillment of the requirements

for the degree of

DOCTOR OF PHILOSOPHY

In

Mechanical Engineering

May 31, 2022

Nashville, Tennessee

Approved:

Eric J. Barth, Ph.D.

Michael Goldfarb, Ph.D.

Douglas Adams, Ph.D.

Alvin Strauss, Ph.D.

James Van de Ven, Ph.D.

Table of Contents

List of Tables

List of Figures

Chapter I

Introduction

I.1 Motivation

According to a study sponsored by the U.S. Department of Energy's Industrial Technologies Program, it is estimated that between 20 to 50 % of the 23 quadrillion Btu of annual energy used by the United States' industrial sector is lost during manufacturing processes as waste heat [1]. Concurrently, roughly 10% of all electricity and roughly 16% of all motor system energy used in the manufacturing sector is used to drive compressed air systems [2]. With such a high energy requirement needed to run manufacturing-based pneumatic systems and an abundance of waste heat available at manufacturing sites, processes that make use of waste heat to power pneumatic processes could, in theory, boost overall production efficiency.

One technology capable of reclaiming waste heat to output pneumatic energy is a lesser-known class of the well-known Stirling engine: the Stirling Thermocompressor, though to date, few of these devices have been built and tested, and few models have been published and experimentally verified.

This dissertation will explore the Stirling thermocompressor's potential by (1) introducing a simple, third-order model for a prototype Stirling thermocompressor and validating the model against experimental evidence; (2) demonstrating how Stirling thermocompressors can increase efficiency by utilizing an active, controlled displacer piston; and (3) applying the model and active displacer control scheme to a proof-of-concept, multi-stage thermocompressor arrangement designed to raise air from ambient conditions to industry-standard pressures.

I.2 Background

I.2.1 Stirling Engines and Thermocompressors

Stirling engines have been around since the early 19th century when Robert Stirling first published his patent for a hot air engine and regenerator [3]. Designed to replace the volatile steam engine, Stirling engines did not see much use until advances in heat transfer and materials science

in the 20th century enabled designers to overcome power limitations by raising the working fluid's pressure. Since then, Stirling engines have experienced renewed interest into diverse applications such as automotive design [4], cryogenics and refrigeration [5], concentrated solar power [6], combined heat and power [7], and as power sources for spaceflight applications [8], engineered to replace inefficient thermoelectric generators.

A Stirling engine's basic operation is simple: a displacer piston shuttles a working fluid between hot and cold spaces inside a sealed engine section, inducing pressure oscillations which drive a mechanical power piston whose output can be converted further depending on the desired application. The Stirling thermocompressor is a variant of the Stirling engine and like traditional engines, it's fuel-flexible, virtually noiseless, and potentially highly efficient, requiring little maintenance. It's distinguishing feature is that it keeps its energy output within the pneumatic domain by replacing the traditional Stirling power piston with a pair of check valves, facilitating mass flow through the device.

The first patent for a Stirling thermocompressor was filed a century after Stirling's original [9], and though its design has benefited from the wider world of Stirling research, it has hitherto failed to find a niche market for broad use, though some have been proposed: early on, for instance, the thermocompressor was considered to be a potential platform to power an artificial heart [10]; later, a multi-stage device was projected to be an efficient, noiseless air compressor [11]; and recently, the thermocompressor has been investigated as an oscillating pressure source in pulse-tube refrigerators [12]. Nonetheless, relative to Stirling engines in general, very few devices have actually been built and tested (see [13-16] for examples) – and none as multi-stage architectures capable of compressing air from ambient conditions.

In terms of modelling thermocompressor behavior, Kornhauser [11] and Arques [17] laid much of the analytic groundwork for first-order modelling in the 1990s. More recently, Blagin, et. al. [18-19] proposed a non-traditional, non-isothermal third-order model for accurately designing thermocompressors, and Changzhao and Wang, et. al. [12, 20-21] used an experimentally-verified model to predict a thermocompressor's performance using different working fluids and operating conditions, and against different load arrangements in pulse-tube refrigeration - in this context, the thermocompressor is not a true pump in the way its inventor imagined it because mass flow between the thermocompressor and load requires only one path for both intake and outtake, rather than through separate inlet and outlet ports. Moreover, all mass is retained within the system in

these arrangements, like a traditional Stirling engine. Work remains in developing an experimentally-verified, third-order differential model predicting thermocompressor behavior within a pump arrangement.

I.2.2 Stirling Piston Arrangements

Though researchers have pursued many avenues in order to boost Stirling device performance, few perhaps have been as radical as challenging the piston arrangements themselves. Traditionally, the power and displacer pistons have been coupled by means of a flywheel, though alternative designs have been explored in order to boost efficiency or power output. In Ringbom engines [22], for example, the power piston is kinematically attached to a flywheel while the decoupled displacer actuates in response to changing pressure dynamics within the engine cylinder. Martini engines [23] are similar except the displacer piston is linked kinematically and the power piston dynamically reacts. The highly-successful free-piston engine [24], whose output mechanical power is typically transformed into electric power by means of a linear alternator, does away with traditional kinematic linkages entirely and both displacer and power piston move in response to changing engine dynamics.

Still more recent innovations have led to the development of an “active” or “driven” Stirling engine concept, whereby the displacer piston’s motion is independently controlled and can dictate the thermodynamics of the engine directly. This dynamic control method has had some success even as approaches vary as to how divergent the displacer’s motion path should look: for instance, Tavakolpour-Saleh et al [25-26] altered the frequency of a sinusoidal wave of a controlled displacer engine to better handle loading conditions and perform at resonance, while Briggs et al [27] augmented the traditional free-piston piston motion with 2nd and 3rd order harmonics, creating a non-sinusoidal waveform to increase performance. Gopal, Duke, and Clucas [28-29] proposed and experimentally demonstrated that adding dwell time to a displacer motion sequence (whereby the displacer piston remains motionless at its extreme positions for a small percentage of the operating period) increased work output at high operating frequencies. And Craun and Bamieh [30] modelled an ideal frequency and path for a displacer piston to follow in order to maximize net power in a specific beta-class Stirling arrangement: their resulting algorithm produced a square-wave displacer motion profile.

As the thermocompressor's mechanical displacer piston is naturally decoupled from the device's pneumatic output apparatus, it can be independently actuated and its motion profile easily shaped according to a designer's specifications, allowing researchers to further test the controlled-displacer concept on a novel platform.

I.3 Dissertation Contributions

The dissertation contains three chapters whose primary contributions are as follows:

Chapter 2 showcases the Stirling thermocompressor hardware and proposes a first-principles-based, third-order dynamic model for describing its behavior. A second mathematical derivation is proposed for estimating the device's potential work output based on the final pressures of its ancillary reservoirs. The capability of the thermocompressor's independently-actuated displacer piston to increase energy output using different motion profiles is also demonstrated, and the dynamic model is experimentally verified.

- Uses helium in a sealed, pre-pressured working thermocompressor system (a rarity in the literature) with an end application of establishing a pressure difference between two reservoirs.
- Proposes and experimentally validates a third-order model built from first principles to predict thermocompressor behavior under a variety of displacer motion profiles and frequencies.
- Demonstrates the active controlled displacer concept and its effects on enhancing enthalpy output using sinusoidal and square-wave motion profiles at uniform frequency.

Chapter 3 builds on the work on Chapter 2 by using the model to analyze the controlled displacer piston's output increase when actuating with square-wave motion profiles rather than with sinusoidal ones. Cyclic and periodic energy inputs and losses, enthalpy flow, and efficiency are computed for sinusoidal and square-wave motion profiles to explain the square-wave motion profile's advantage. Finally, the thermocompressor dynamics are augmented in hardware to restrict enthalpy loss to the device's return chamber (effectively dead volume), further experimentally-demonstrating the controlled displacer piston's advantage in reducing such losses.

- Uses the third-order model to simulate enthalpy flow within and without the device, highlighting the differences in occurrences and timing of enthalpy output between low-performing sinusoidal and high-performing square-wave controlled displacer motion profiles.
- Shows periodic energy losses relative to inputs, and computes the device's transient cyclic efficiency for both sinusoidal and square-wave displacer motion profiles.
- Experimentally demonstrates and models the effects of decreased enthalpy flow to the return chamber on overall energy output for both sinusoidal and square-wave displacer motion profiles using in-line return chamber offices of different sizes.

Chapter 4 tests the viability of a waste-heat-driven, multi-stage thermocompressor, experimentally and analytically. The single-stage thermocompressor and third-order model employed in the previous chapters are re-utilized in a proof-of-concept arrangement capable of raising filtered, dry air to 80 psig standards. The third-order model is further adapted to propose and evaluate multiple, plausible multi-stage thermocompressor arrangements based on a range of potential waste heat inputs and mass flow demands.

- Experimentally characterizes a single-stage thermocompressor using air within the pressure range of typical industrial air compressors, up to approximately 80 psig.
- Adapts the previously-developed third-order model for air at these pressures to show how the model and experimental data converge.
- Details the arrangements (the necessary number of stages, the operating frequency of each stage, etc.) and predicts the performance of multiple multi-stage systems based on the architecture of the experimental prototype, varying heat inputs, and various load demands.
- Compares the performance of an optimized set of multi-stage thermocompressor arrangements to the generalized performance of extant industrial air compressors.

Chapter II

Active Stirling Thermocompressor: Modelling and Effects of Controlled Displacer Motion Profile on Work Output

II.1 Preface

Portions of the text of this chapter appeared previously in:

> Thomas, S, & Barth, E J. (2019) *Stirling Thermocompressor: Lumped Parameter Modeling and Experimental impact of Displacer Motion Profile on Work Output*. Proceedings of the ASME/BATH 2019 Symposium on Fluid Power and Motion Control. ASME/BATH 2019 Symposium on Fluid Power and Motion Control. Longboat Key, Florida, USA. V001T01A040. ASME. https ://doi.org/10.1115/FPMC2019-1683

The text is under consideration for review and acceptance:

> Thomas, S and Barth, E. J. (2022) Active Stirling Thermocompressor: Modelling and Effects of Controlled Displacer Motion Profile on Work Output, ***Submitted to Applied Energy***

II.2 Introduction

Thermocompressors are Stirling devices capable of producing pneumatic power from a thermal input without the need for a transitional mechanical conversion. Thermocompressors share all the desirable qualities typical of Stirling engines: They're fuel flexible, as they only require heat to produce power. They're efficient, theoretically exceeding engine-driven compressors at high pressure ratios. And their virtually noiseless operation may make them preferable to conventional compressors in some applications, especially if multiple thermocompressors comprise a single, multi-stage compressor arrangement [11].

Despite their advantages, very little modelling and experimental work has been done to predict thermocompressor behavior when compared to the larger class of Stirling devices. Such modeling of Stirling machines is conventionally classified in orders of analysis [31]: first-order analyses, of

which Schmidt's analysis and the Beale number [32] are the most well-known, rely on many simplifying assumptions to arrive at either closed-form analytical solutions or back-of-the-envelope estimations to predict Stirling engine performance. For thermocompressors specifically, A. A. Kornhauser [11] and Arques [17] have laid sufficient groundwork for first order analyses. Second-order analyses may also rely on several simplifying assumptions but improve on first-order analyses by independently quantifying heat and power losses. Third-order analyses, like Urieli and Berchowitz's nodal model [33], rely on fewer assumptions and divide a Stirling device into multiple control volumes (or nodes) in order to numerically solve differential equations of energy and mass conservation. Analyses that make use of finite element analysis (FEA) and computational fluid dynamics (CFD) to arrive at device-specific performance predictions would also fall into this category, and while FEA and CFD tools are well-suited to predicting the performance of a specific device under as few assumptions as possible, simpler third-order analyses with fewer, lumped-parameter nodes can be applied to a wide range of devices and can be a crucial early step to evaluating a Stirling device's design. Such models are also computationally less expensive.

Only recently have researchers begun to apply third-order modelling principles to Stirling thermocompressors. Blagin, et. al. [18-19] proposed a non-traditional, non-isothermal model for more accurately designing thermocompressors, testing different design factors such as geometry, regenerator efficiency, operating frequency, and heat transfer capabilities. Changzhao and Wang, et. al. [12, 20-21] used an experimentally-verified model to predict a thermocompressor's performance using different working fluids and operating conditions, and against different load arrangements. Similarly, Lin, et. al. [34] proposed a third-order model to aid in the design and testing of an appropriate thermocompressor annular regenerator.

While some investigations into thermocompressor applications differ [35-36], most of the studies surveyed above focused on Stirling thermocompressors as part of a pulse-tube refrigeration or cryocooling system, with the thermocompressor replacing a traditional compressor piston to generate a pressure wave within the tube. In this arrangement, the thermocompressor is not a true pump in the way its inventor, V. Bush, imagined it [9], because mass flow between the thermocompressor and load requires only one path for both intake and outlet, rather than through separate inlet and outlet ports. Moreover, all mass is retained within the system in these arrangements. The arrangement studied in this paper is not a pulse-tube-based system, and

accounts for variable mass within the system as influenced by enthalpy input (low-pressure intake) and enthalpy output (high-pressure outlet).

Building from this scholarship, our work diverges in the following ways: 1) the thermocompressor examined here fits within a traditional compressor application, whereby mass is unilaterally pumped through the thermocompressor; consequently, as conditions in the load change (i.e., the receiving vessel starts to pressurize), the cycle-by-cycle behavior of the thermocompressor also changes as greater internal engine pressure is necessary before mass can escape the engine. 2). Lumped-parameter modelling is kept as simple as possible, with as few nodes as necessary (fewer than half a dozen in our model). 3). Solid elements such as the surrounding environs between the working fluid and heat source/sink are not explicitly modelled but become part of the overall heat source/sink parameters, following the assumption that for its operating time, the system is in relatively steady-state operation. 4). Most importantly, the model can incorporate a variety of unique frequencies and displacer waveforms, which allow for direct shaping of the thermocompressor's thermodynamics.

This latter aspect of our device's design and model has recently garnered interest within the broader Stirling community. The developing consensus is that more square-like displacer motion-paths are better suited to improving Stirling performance: for instance, Craun and Bamieh [30] used optimal periodic control theory to produce an ideal frequency and path for a displacer piston to follow in order to maximize net power from in a specific beta-class arrangement, and the algorithm produced a square-wave displacer motion profile. Briggs et al [27] augmented the traditional free-piston piston motion with 2^{nd} and 3^{rd} order harmonics, creating a non-sinusoidal waveform to increase performance. And Gopal, Duke, and Clucas [28-29] proposed and experimentally demonstrated that adding dwell time to a displacer motion sequence (whereby the displacer piston remains motionless at its extreme positions for a percentage of the operating period) increased work output.

To the authors' knowledge, the controlled displacer concept has not yet been experimentally validated on a thermocompressor platform; therefore, in this paper, we seek to corroborate the controlled displacer concept. We will first review how a thermocompressor differs from traditional Stirling engines and how energy output can be quantified using a thermocompressor setup. Next, we will present a mathematical model developed from first principles to predict and explain the results of our experiments. We will then describe and discuss our experimental results and draw

conclusions.

II.3 Thermocompressor Overview and Device Schematic

The primary difference between a Stirling thermocompressor and traditional Stirling engines is that in a thermocompressor, the power piston has been replaced by a pair of check valves coupled to reservoir tanks (Fig. II.1 and Fig. II.2). The pressure oscillations within the engine due to the displacer piston's motion pump mass from the low-pressure reservoir, through the device, and into the high-pressure reservoir, creating a pressure potential difference between the reservoirs. This pressure potential does not directly drive the displacer piston, which actuates independently via a separate mechanical arrangement, so the displacer and power output mechanisms of a Stirling thermocompressor are naturally decoupled.

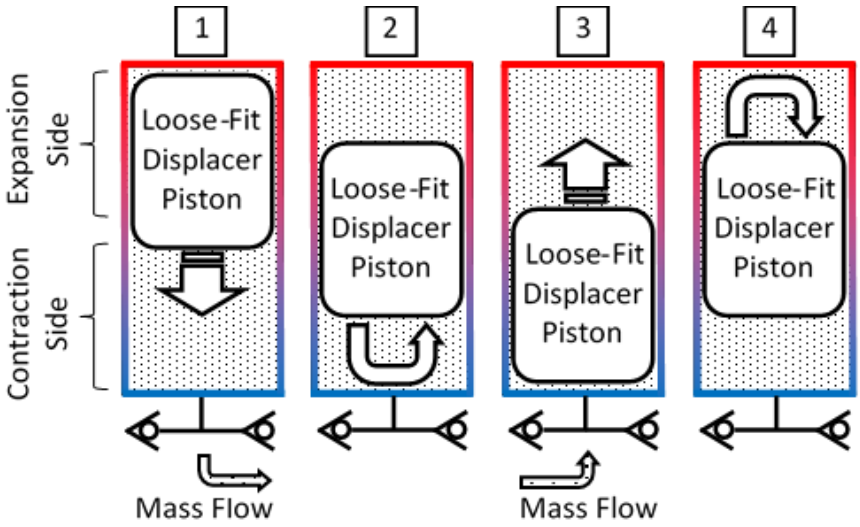

Fig. II.1. Thermodynamic cycle of a Stirling thermocompressor. As the displacer moves from top dead center towards bottom dead center, much of the working fluid is displaced from the contraction side to the expansion side and the temperature and pressure of the working fluid increases. When the pressure in the thermocompressor is greater than the pressure in the high-pressure reservoir, one check valve opens and working fluid flows into the high-pressure reservoir. Conversely, when the displacer piston moves from bottom dead center to top dead center, much of the working fluid is displaced from the expansion side to the contraction side and temperature and pressure of the working fluid decreases. When the pressure within the thermocompressor is lower than the pressure in the low-pressure reservoir, a second check valve opens and working fluid fills into the thermocompressor.

The device discussed in this paper (and outlined in greater detail in [15]) is composed of a sealed engine section, two pressure reservoirs, and a "return chamber" (Fig. II.2 and Fig. II.5). The return chamber houses the linear motor that drives the displacer piston. To overcome any significant pressure difference between the engine section and return chamber which might impede the linear motor's actuation, a small in-line orifice between the return chamber and engine section allows pressure-compensating mass flow between them. The orifice restricts flow so that the pressure in the return chamber nearly approximates the median pressure in the engine section, which allows the linear motor to efficiently drive the displacer piston despite the high pressure oscillations generated within the sealed engine section.

Cartridge heaters and a PID controller maintain the elevated temperature of the stainless steel heater head located at the top of the engine, and aluminum cooling fins disperse accumulated thermal energy at the bottom of the engine to maintain an appreciable temperature difference between the expansion and contraction sides. An Inconel cylinder together with the loose-fit displacer piston forms the regenerative channel wherein the working fluid (helium) deposits or absorbs thermal energy as it travels between the expansion and contraction sides. O-rings seal the engine section and return chamber.

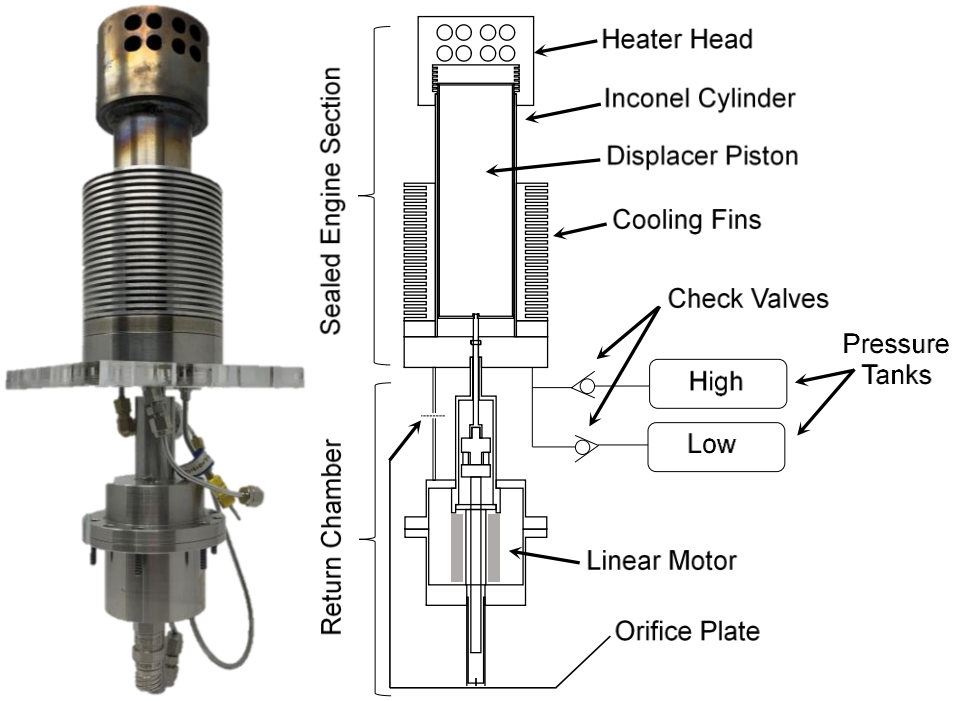

Fig. II.2. Photo (left) and schematic (right) of the Stirling thermocompressor.

The two pressure reservoirs are connected to the contraction side of the engine section via a tee-fitting and check valves, which ensure that a pressure difference between the two reservoirs develops as the pressure within the engine oscillates. How quickly this pressure difference is established depends on the amplitude of the pressure oscillations within the engine section, the size of the reservoirs, and characteristics of the check valves such as cracking pressure and discharge rate.

II.4 Enthalpy Work of Thermocompressor and Total Potential Work

The thermocompressor creates a potential energy difference between pressure reservoirs through enthalpy flow. This transient process can be modeled in the absence of heat flow or external work but once mass has been deposited into or withdrawn from a reservoir, heat transfer effects come into play and the masses within the reservoirs fall into isothermal equilibrium. The amount of potential energy stored in the system can be estimated from the known pressure difference between the two reservoirs and their respective volumes. Consider the following illustration (Fig. II.3): two reservoirs of known volumes (V_{high}, V_{low}) and different initial pressures (P_{high}, P_{low}) are located in close proximity. If an ideal, sealed piston is placed between the charged reservoirs and the piston's displacement volume, V_{piston}, is such that after actuating, the final pressures between the reservoirs are equal (P_{final}), then the amount of work necessary to move the piston is a function of the initial pressures and volumes of the reservoirs.

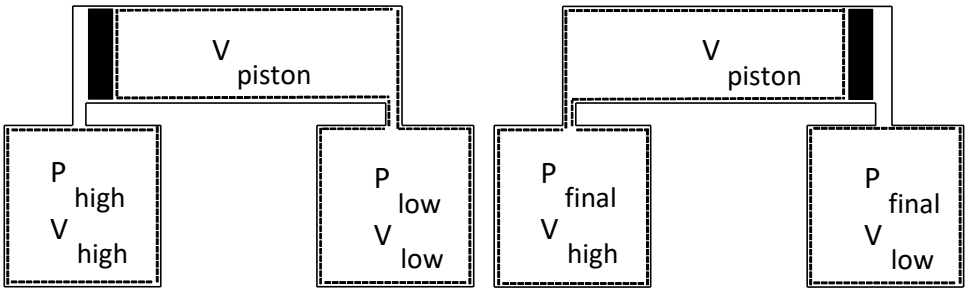

Fig. II.3. Idealized piston example. The left image shows the piston and high- and low-pressure reservoirs in an unactuated state, and the image on the right shows the piston and reservoirs in an actuated state.

If we assume that such a process is isothermal, then the relationship between the initial and final pressures and volumes of the reservoirs is as follows:

$$P_{high}V_{high} = K_{high} = P_{final}\left(V_{high} + V_{piston}\right) \tag{1}$$

$$P_{low}\left(V_{low} + V_{piston}\right) = K_{low} = P_{final}V_{low} \tag{2}$$

where P_{high} and P_{low} are the initial pressures of the high and low reservoirs, respectively; K_{high} and K_{low} are constants; and V_{high} and V_{low} are the volumes of the high and low reservoirs, respectively. The work done by the high-pressure reservoir on the piston (W_{high}) and the work done by the piston on the low-pressure reservoir (W_{low}) are:

$$W_{high} = \int P\, dV = K_{high} \int_{V_{high}}^{V_{high}+V_{piston}} \frac{1}{V} dV = P_{high}V_{high}\left(\ln\left(\frac{V_{high}+V_{piston}}{V_{high}}\right)\right) = P_{high}V_{high} \ln\left(\frac{P_{high}}{P_{final}}\right) \tag{3}$$

$$W_{low} = \int P\, dV = K_{low} \int_{V_{low}+V_{piston}}^{V_{low}} \frac{1}{V} dV = P_{low}V_{low}\left(\ln\left(\frac{V_{low}}{V_{low}+V_{piston}}\right)\right) = P_{low}V_{low} \ln\left(\frac{P_{low}}{P_{final}}\right) \tag{4}$$

The total available work is the sum of these two expressions (positive work from W_{high} and negative work from W_{low}). Using Equations (1) and (2), the following expression for P_{final} can be derived:

$$P_{final} = \frac{\left(V_{low}-V_{high}\right) \pm \sqrt{\left(V_{high}-V_{low}\right)^2 + 4\left(\frac{V_{low}}{P_{low}}\right)\left(P_{high}V_{high}\right)}}{2\left(\frac{V_{low}}{P_{low}}\right)} \tag{5}$$

Therefore, the total work available due to pressure difference between the reservoirs (W_{total}) is:

$$W_{total} = P_{high}V_{high}\ln\left(\frac{P_{high}}{P_{final}}\right) + P_{low}V_{low}\ln\left(\frac{P_{low}}{P_{final}}\right) \quad (6)$$

This relationship will serve to quantify the energy delivery of the thermocompressor.

II.5 Dynamic Model

In addition to the two pressure reservoirs, the Stirling thermocompressor can further be divided into three additional primary control volumes (Fig. II.4): the expansion- and contraction-side control volumes, separated by the displacer piston's known position, and the return chamber's control volume. The pressure dynamics within each of these control volumes are modeled from first principles, beginning with the first law of thermodynamics: the rate of change of a control volume's internal energy ($\dot{U}$) is equal to a summation of the change in enthalpy ($\dot{H}$), heat flow ($\dot{Q}$), and work ($\dot{W}$) done to the control volume:

$$\dot{U} = \dot{H} + \dot{Q} - \dot{W} \quad (7)$$

These terms can be expanded as follows [15]:

$$\dot{U} = \dot{m}(c_v)T + m(c_v)\dot{T} = \frac{1}{\gamma-1}\left(\dot{P}V + P\dot{V}\right) \quad (8)$$

$$\dot{H} = \sum \dot{m}(c_p)(T) \quad (9)$$

$$\dot{W} = P\dot{V} \quad (10)$$

The above expansion includes terms representing the control volume's mass (m), temperature (T), geometric volume (V), pressure (P), the particular working fluid's specific heat at constant pressure (c_p) and constant volume (c_v), as well as the ratio between the two (γ). Rearranging, the general form for the dynamics in each control volume becomes:

$$\dot{P} = \frac{\dot{Q}(\gamma-1)+\dot{m}T(\gamma R)-P\dot{V}(\gamma)}{V} \tag{11}$$

The particular forms of Equation 11 for each control volume (expansion and contraction control volumes within the sealed engine section denoted with subscripts "e" and "c", respectively; the return chamber control volume denoted with subscript "r"; and the control volumes within the high- and low-pressure reservoirs denoted with subscripts "high" and "low," respectively) are illustrated in Fig. II.4 below.

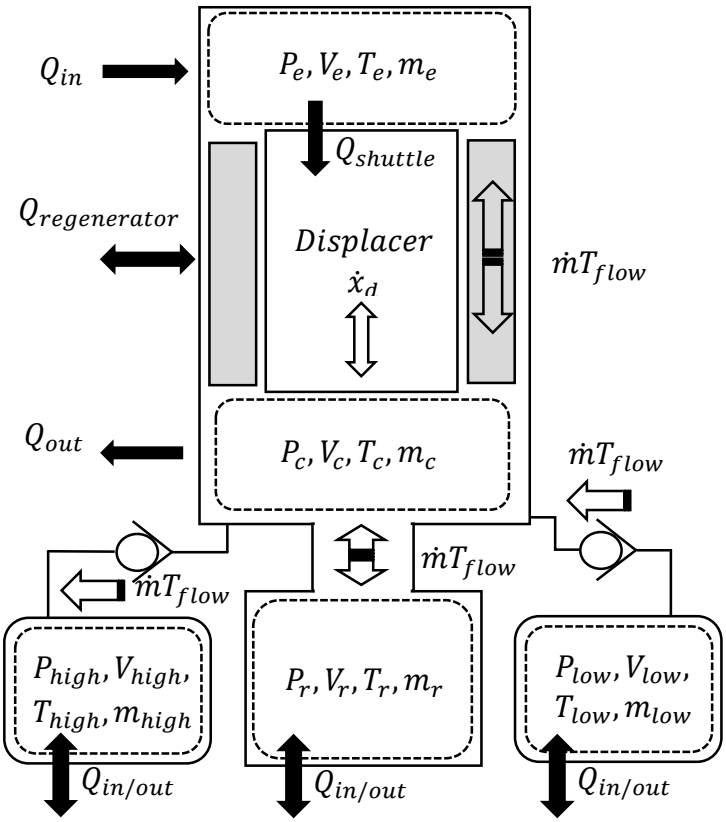

Fig. II.4. Illustrated control volumes and dynamic relationships.

The primary factors driving changes in pressure within each control volume are detailed as follows.

II.5.1. Changes in Volume

Whereas the volumes of the high- and low-pressure reservoirs remain constant, the volumes within the expansion and contraction sides of the engine and the return chamber change in proportion to the velocity of the displacer piston (in the latter case, the displacer's connecting rod extends through an O-ring and into the return chamber, causing minor volume fluctuations). The displacer piston's motion profile is the only independent input in our model.

II.5.2. Mass Flow

Mass flow within the system is divided into two types of flow: i) mass flow within the sealed engine section (between the expansion and contraction side volumes) and ii) between the sealed engine section and the return chamber through the orifice plate and between the sealed engine section and the high and low-pressure reservoirs through the check valves. Mass flow between the expansion and contraction sides of the engine around the displacer piston (annular in shape) is modeled according to a solution to the Navier Stokes equation [37]. The form of this solution is given in Equation 12 and its sign is dependent upon the velocity of the displacer piston and the difference in pressure between the expansion and contraction sides.

$$\dot{m}_{e/c} = \frac{2\pi\rho}{\ln(r_{cyl}/r_d)}\left[\frac{1}{2}\ln\left(r_d/r_{cyl}\right)r_d^2 + \frac{1}{4}\left(r_{cyl}^2 - r_d^2\right)\right](v_d) - \frac{\pi\rho}{8\mu l_d}\left[r_{cyl}^4 - r_d^4 - \frac{\left(r_{cyl}^2 - r_d^2\right)}{\ln(r_{cyl}/r_d)}\right](P_e - P_c) \quad (12)$$

The above expression includes terms representing the velocity of the displacer piston (v_d), and geometric constants representing the length (l_d) and radius (r_d) of the displacer piston, and the inner radius of the thermocompressor's Inconel cylinder (r_{cyl}). The working fluid's density (ρ) and dynamic viscosity (μ) were derived from the working fluid's pressure (measured in bar) and temperature (measured in Kelvin), as detailed in [38]:

$$\rho = 48.14\frac{P}{T}\left[1 + 0.4446\frac{P}{T^{1.2}}\right]^{-1} \quad (13)$$

$$\mu = \mathrm{T}^{0.7}(3.674 \times 10^{-7}) \tag{14}$$

Between the sealed engine section and the return chamber, mass flows through the orifice and the flow may be either choked or unchoked [39]. The critical pressure (P_{cr}) determining whether the flow is choked or unchoked is modeled as:

$$P_{cr} = \left(\frac{2}{\gamma+1}\right)^{\gamma/(\gamma-1)} \tag{15}$$

Accordingly, expressions for choked flow (Equation 16a) and unchoked flow through an orifice (Equation 16b) are given as:

$$\dot{m} = A_{orifice} C_d C_1 \frac{P_{upstream}}{\sqrt{T_{flow}}} \tag{16a}$$

if $P_{downstream}/P_{upstream} \leq P_{cr}$, and

$$\dot{m} = A_{orifice} C_d C_2 \frac{P_{upstream}}{\sqrt{T_{flow}}} \left(\frac{P_{downstream}}{P_{upstream}}\right)^{1/\gamma} \times \sqrt{1 - \left(\frac{P_{downstream}}{P_{upstream}}\right)^{\gamma-1/\gamma}} \tag{16b}$$

if $P_{downstream}/P_{upstream} > P_{cr}$.

In addition to the area of the orifice ($A_{orifice}$) and the discharge coefficient (C_d), the constants C_1 and C_2 are defined as:

$$C_1 = \sqrt{\frac{\gamma}{R}\left(\frac{2}{\gamma+1}\right)^{(\gamma+1)/(\gamma-1)}} \tag{17}$$

$$C_2 = \sqrt{\frac{2\gamma}{R(\gamma-1)}} \tag{18}$$

Above, R represents the working fluid's unique gas constant. Flow can be modeled similarly between the sealed engine section and the reservoirs, with the inclusion of a flow condition where no flow occurs if the pressure difference between the upstream and downstream pressures is less than the minimum cracking pressure (P_{min}) needed to overcome the check valves.

II.5.3. Heat Flow

Energy absorbed from the heater head's inner surface area at the expansion side control volume leaves the control volume by means of enthalpy flow and shuttle loss. Shuttle loss refers to energy absorbed by the displacer piston when the displacer rests at the top-dead-center position that is deposited within the regenerative channel and contraction side control volume as the displacer moves to the bottom-dead-center position. From observation of several Stirling devices, this heat loss is classically modeled as [32]:

$$\dot{Q} = \frac{0.4 l_{stroke}^2 k_{He} d_d (T_e - T_c)}{S l_d} \tag{19}$$

where, in addition to the temperature difference between the expansion and contraction control volumes ($T_e - T_c$), the stroke length (l_{stroke}), diameter of the displacer (d_d), length of displacer (l_d), thermal conductivity of the working fluid (k_{He}), and radial gap (S) between the Inconel cylinder and displacer are also factors.

Within the expansion and contraction control volumes, the primary mode of heat-transfer between the working fluid and the surrounding wall surface is forced convection. Using Newton's Law of Cooling, the rate of energy transfer is modeled linearly:

$$\dot{Q} = hA_{wall}(T_{wall} - T_{fluid}) \tag{20}$$

The convection coefficient (h) above can be very difficult to measure or estimate in all but very simple geometries, but because the motion of the displacer piston within the surrounding Inconel resembles a gas spring or traditional automotive piston (even granting that mass intentionally flows around the displacer, the gap between the displacer and Inconel is very small and consequently, the piston experiences significant resistance when compressing a control volume), we have elected

to model the convection coefficient after Hohenberg's expression for heat transfer in an internal combustion engine's pistons [40]:

$$h = K_1 V^{-0.06} P^{0.8} T^{-0.4} \left(\bar{v}_p + K_2\right)^{0.8} \tag{21}$$

Above, V is the volume of the expansion or contraction side (meters^3), P is the pressure in the volume (bar), T is the mean gas temperature (degrees Kelvin), and $\bar{v}_p$ is the mean piston speed (meters/second). The constants K_1 and K_2 are tunable though we decided to use the original author's values for simplicity [40]: K_1 = 130, K_2 = 1.4. Heat flow out of the return chamber and reservoir tanks is also modeled using Newton's Law of Cooling using a typical value for unforced convection [41]: $h_{unforced}$ = 22 (Watts/meter^2 degrees Kelvin). The walls of all control volumes are modelled as steady-state heat sinks or sources.

II.5.4. Regenerative Channel

Mass flowing within the regenerative channel between the expansion and contraction control volumes will deposit or absorb energy to/from the walls of the regenerative channel and the displacer piston as it shuttles from one volume to the other. The amount of energy absorbed or removed correlates to the change in enthalpy in the working fluid from when the fluid enters and exits the channel. The effectiveness (ε) of this process can be modeled as follows:

$$\boldsymbol{\varepsilon} = \frac{\text{actual enthalpy change}}{\text{maximum theoretical enthalpy change}} \tag{22}$$

Given that the specific enthalpy of a working fluid can be expressed as $h = c_p T$, the temperature of the gas as it leaves the regenerative channel (T_{reg}) can be linearly approximated as

$$T_{reg} = T_e + \varepsilon(T_c - T_e) \tag{23}$$

when mass flows from the expansion control volume to the contraction control volume, and

$$T_{reg} = T_c + \varepsilon(T_e - T_c) \tag{24}$$

when mass flows from the contraction control volume to the expansion control volume. At low displacer frequencies, mass flow speeds within the engine section are much slower than the heat transfer dynamics within the channel, so the regenerator's effectiveness was modelled ideally at 100% effectiveness.

With the exception of temperature and pressure (and hence, mass) which change depending on the desired user specifications, the parameters of our model are presented below (Table II.1).

TABLE II.1
SUMMARIZED MODELLING PARAMETERS

Expansion Side Initial Volume	V_e	35.8 cm^3
Contraction Side Initial Volume	V_c	11.3 cm^3
Return Chamber Volume	V_r	17.0 cm^3
High Pressure Reservoir Volume	V_{high}	1,024 cm^3
Low Pressure Reservoir Volume	V_{low}	523 cm^3
Specific Heat at Constant Pressure, Helium	c_p	5.19 J/g K
Specific Heat at Constant Volume, Helium	c_v	3.12 J/g K
Specific Heat Ratio, Helium	γ	1.67
Ideal Gas Constant, Helium	R	2.08 J/g K
Helium, Conductivity	k_{He}	0.18 W/m K
Orifice - Orifice Area	$A_{orifice}$	8.04E-08 mm^2
Check Valve - Orifice Area	A_{check}	4.52E-06 mm^2
Orifice - Discharge Coefficient	$C_{d,orifice}$	0.81
Check Valve - Discharge Coefficient	C_d	1.13
Displacer Piston Length	l_d	14.6 cm
Displacer Piston Radius	r_d	2.38 cm
Inconel Cylinder Radius	r_{cyl}	2.42 cm
Radial Gap between Inconel and Displacer	S	0.4 mm
Stroke Length	l_{stroke}	2.26 cm
Hohenberg's Expression, Constant 1	K_1	130
Hohenberg's Expression, Constant 2	K_2	1.4
Heat Transfer Coefficient for Unforced Convection	$h_{unforced}$	22 W/m^2 K
Regenerator Effectiveness	ε	1.00
Ambient Temperature	$T_{wall,amb}$	298.1 K
Check Valve - Cracking Pressure	P_{min}	13.8 kPa
Expansion Side-Source Heat Transfer Area	$A_{wall,e}$	52.7 cm^2
Contraction Side-Sink Heat Transfer Area	$A_{wall,c}$	52.7 cm^2
Return Chamber-Ambient Heat Transfer Area	$A_{wall,r}$	172 cm^2
High Pressure Reservoir -Ambient Heat Transfer Area	$A_{wall,high}$	712 cm^2
Low Pressure Reservoir -Ambient Heat Transfer Area	$A_{wall,low}$	674 cm^2

For each control volume, the relevant states (pressure, mass, volume, and temperature) are monitored throughout a simulation. Changes in a control volume's pressure are a result of the aforementioned volumetric changes (corresponding directly to the displacer piston's motion), mass flow, and heat flow dynamics as applied to Eqn. 11. The results of Eqn. 11, together with any mass flow into and out from a control volume, are integrated using an ODE solver to produce the pressure and mass states. Temperature can then be computed using the ideal gas law.

II.6 Experimental Setup and Model Validation

Fig. II.5 below shows the Stirling thermocompressor's experimental setup. The setup and instrumentation used for the validation of the dynamic model of the device apart from the reservoir tanks are described in [15] with one variation: the needle valve used in [15] was replaced by an orifice with an approximate 0.32 mm opening diameter.

To facilitate flow from the engine to the reservoirs, a tee-fitting connected the contraction side of the engine section to the check valves, which were then connected to the reservoir tanks through 1/4-inch and 1/8-inch aluminum tubing. The check valves had a cracking pressure of at least 0.07 bar (1 psi) and a flow coefficient (C_V) of 0.22. The high- and low-pressure reservoirs were a pair of double-ended cylinders with volumes of 1000 cm^3 and 500 cm^3, respectively, each equipped with a pressure transducer. The reservoirs were connected at one inlet to the check valves and at the other inlet to each other via a ball valve. When closed, the ball valve prevented flow between the tanks and maintained the tanks' pressure difference while the engine was in operation. Opening the valve enabled the reservoirs to exchange working fluid when resetting the device between data sets. For data acquisition, Matlab Simulink was used in conjunction with a Real-Time Windows target machine.

During setup, the thermocompressor's mean operating pressure was set to an approximate target value using a source tank, and the pressure transducers were calibrated by filling the device from known atmospheric conditions to the target value and comparing the pressure transducer outputs to a reference. Setting the thermocompressor's mean operating pressure resulted in all control volumes being at the same pressure (including the high and low pressure reservoirs).

The heater head was tuned to a target temperature by means of a PID controller and thermocouple attached to the top surface of the heater head. A second thermocouple was also located internally within the contraction side of the engine, and data from this thermocouple was

recorded. Because the external thermocouple used to regulate power to the heater cartridges could not accurately represent the internal working fluid's temperature on the engine's expansion side, the temperature of the expansion side was estimated using the thermocouple data from the contraction side. In other words, given the measured temperature on the contraction side, the temperature of the expansion side was posited using an estimated temperature difference. This estimation was then validated against the experimental data using the model.

The position of the linear motor was dictated by an analog voltage command sent to the motor's controller (from the same manufacturer as the motor). The motor's position (i.e., the displacer's position) was recorded using software from the manufacturer, and this position data was time-matched to the data collected from the pressure transducers and thermocouple from the thermocompressor. Electromagnetic interference was apparent in the pressure sensor data while the motor was in operation but upon examination of recorded data taken when the motor was switched off, the difference between signal and noise is plainly apparent.

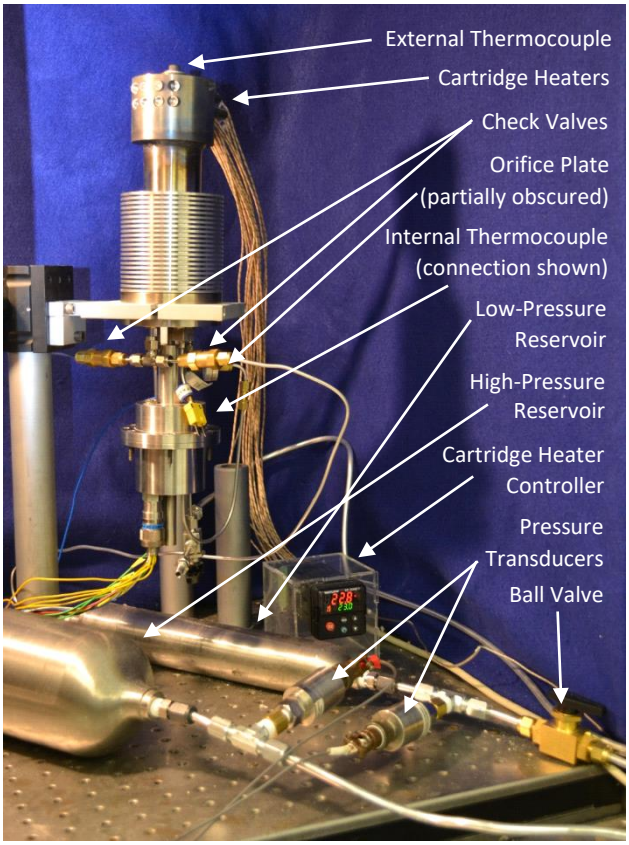

Fig. II.5. Experimental setup.

The lumped-parameter model was validated for traditional sinusoidal and novel square-waveform displacer motion profiles operating at 1, 1.5, and 2 Hz. The operating pressure was set to approximately 21 bar and the temperature difference between the expansion and contraction sides of the engine was estimated to be approximately 185 K. Shown below, the resultant pressure differences between the reservoirs and work outputs of the Stirling thermocompressor were compared for the different motion profiles and operating frequencies.

II.6.1 Experiment and Model Convergence

To set up each experiment, the heater head was turned on and allowed to reach steady-state temperature, the system was pressurized with helium using a regulated supply, and the ball valve between the reservoirs was opened. To start each experiment, data acquisition started, the linear motor was actuated at the appropriate motion profile and frequency, and the ball valve was subsequently closed. Approximately 180 seconds of data were taken in each experimental data set. The motor began operating at approximately 10 seconds into an experiment and the ball valve was closed at approximately 20 seconds. Data was recorded for an additional 20 seconds after the motor shut off. Sample plots of sinusoidal and square-wave motion profile data are shown below (Fig. II.6 and Fig. II.9). As demonstrated, the motor-controlled displacer piston closely tracked the desired position when actuated with a sinusoidal motion command input.

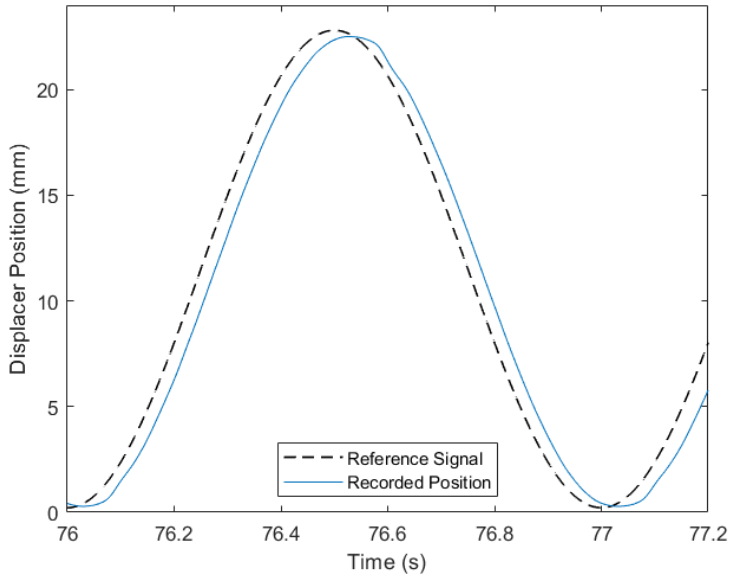

Fig. II.6. Sample sinusoidal displacer motion profile (1 Hz) with transmitted reference signal and recorded displacer position shown.

For each experiment, the measured displacer position data was fed into the dynamic model as presented above. The pressure states of the model were then compared to the measured reservoir pressure data. The model matches the experimental data very closely for sinusoidal displacer motion profiles with regards to both the final pressure developed within the pressure reservoirs and the trajectory the dynamics take to get there (Fig. II.7). Both the model and the data show a high mass-flow output at the beginning of the sequence, when the ball valve is closed and the reservoirs become isolated from each other.

In terms of potential energy stored (potential work output), sinusoidal waves tended to level-off after 40 seconds of operation (Fig. II.8). And as expected, while energy continues to accumulate, power output drops as an overall pressure difference develops between the reservoirs and more energy is needed for subsequent pressure-difference gains. Though accurate, the model tends to slightly undershoot the high-pressure reservoir's dynamics at the beginning of the sequence but more-precisely estimates the final-state pressure. The model is therefore predicting that greater amounts of heat are escaping from the high-pressure reservoir than may actually be true, which indicates that the modelled convective heat coefficient within the high-pressure reservoir is slightly too high at the beginning of the sequence. Using a dynamic convective heat coefficient could solve this modelling problem at the expense of model simplicity. Finally, the fact that the model accurately predicts the final-state conditions lends credence to the posit that the overall temperature difference within the device is estimated correctly.

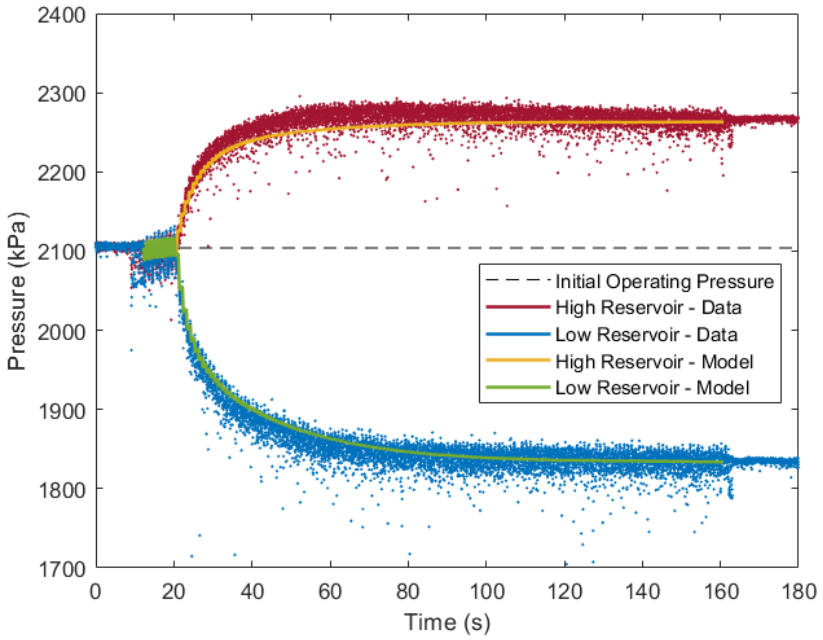

Fig. II.7. Filtered experimental data (high reservoir – red, top and low reservoir – blue, bottom) resulting from a 1 Hz sinusoidal displacer motion profile, shown together with simulation results (high reservoir – yellow, top and low reservoir – green, bottom). Operating conditions were approximately 21 bar mean operating pressure and 185 K temperature difference between the expansion and contraction sides of the engine section.

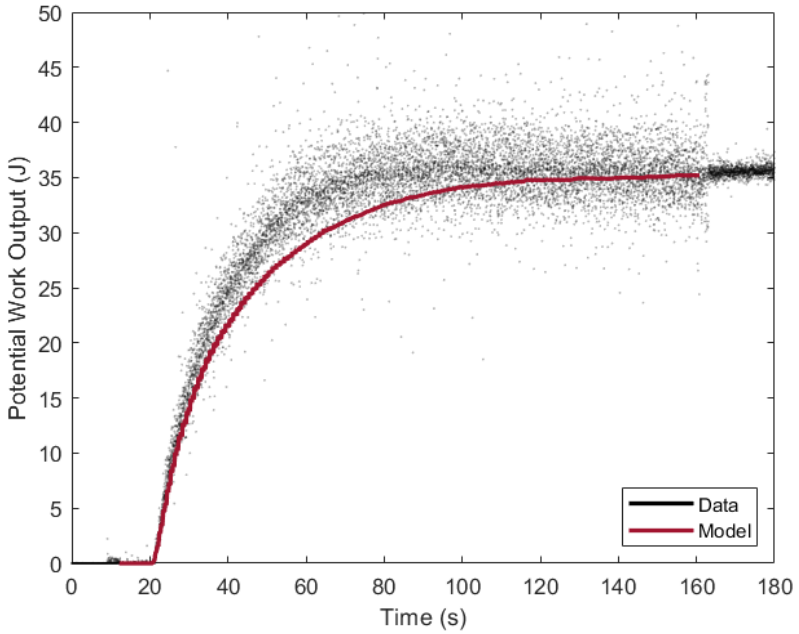

Fig. II.8. Calculated stored potential energy resulting from a 1 Hz sinusoidal displacer motion profile (experimental and simulated results shown). Operating conditions were approximately 21 bar mean operating pressure and 185 K temperature difference between the expansion and contraction sides of the engine section.

In contrast to the motor's response to sinusoidal commands, the motor had greater difficulty accurately following square-wave reference signals in part due to signal processing at the motion controller (Fig. II.9) and in part due to friction from the O-ring separating the engine and return chamber sections through which the displacer's rod actuates. The effect is more pronounced at higher operating frequencies (Fig. II.16), as will be discussed further.

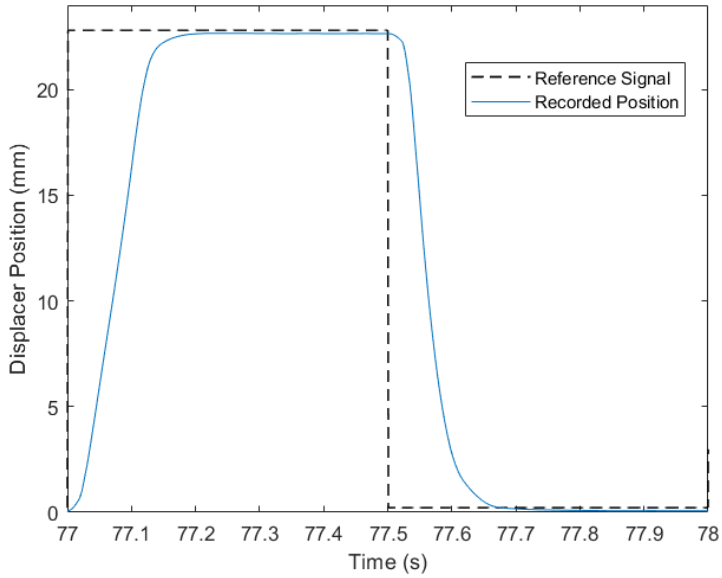

Fig. II.9. Sample square-wave displacer motion profile (1 Hz), with transmitted reference signal and recorded displacer position shown.

As in the case of data sets utilizing sinusoidal displacer motion profiles, the model accurately predicts the dynamics and final-state reservoir pressures for data sets using measured square-wave displacer motion profiles (Fig. II.10). Power output remains high early in the sequence and continues to slowly diminish before potential energy stored (potential work output) levels off late in the sequence (Fig. II.11). With regards to the dynamics in the high-pressure reservoir, the model slightly overshoots the experimental data at the beginning of the sequence before slightly undershooting the data at the end of the sequence, not unlike sinusoidally-driven data sets. As before, adjusting the value of the (constant) convective coefficient could eliminate one of these modelling deficiencies but not both, and modelling with a dynamic convective coefficient would require a more complex model.

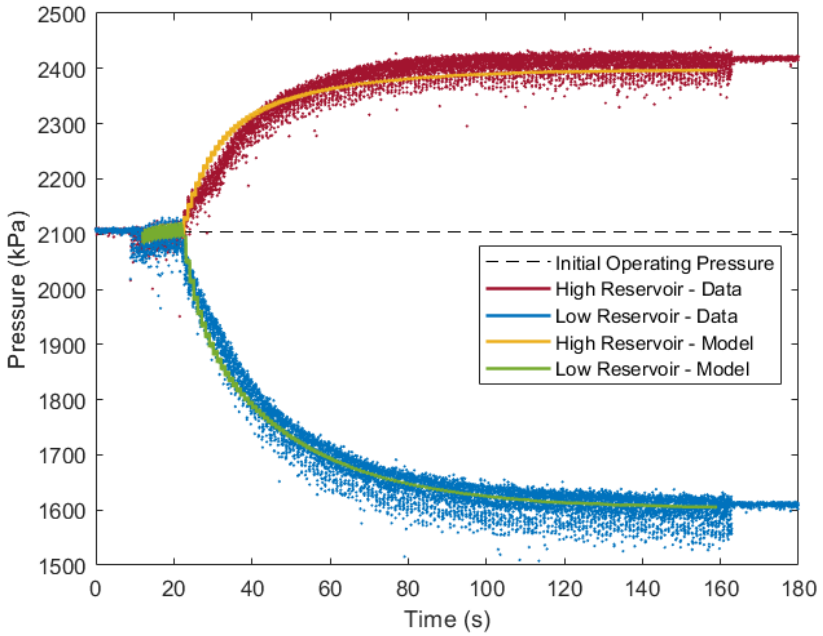

Fig. II.10: Filtered experimental data (high reservoir – red, top and low reservoir – blue, bottom) resulting from a 1 Hz square-wave displacer piston motion profile, shown together with simulation results (high reservoir – yellow, top and low reservoir – green, bottom). Operating conditions were approximately 21 bar mean operating pressure and 185 K temperature difference between expansion and contraction sides of the engine section.

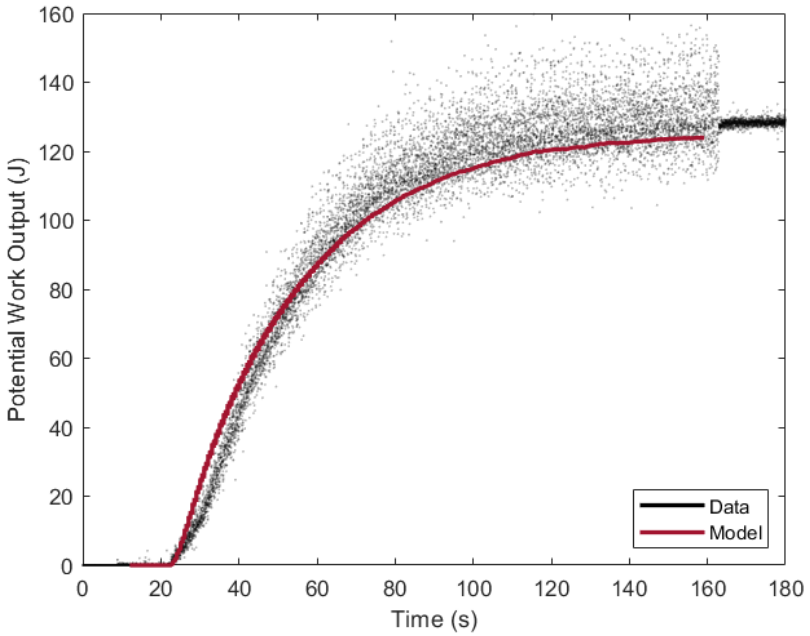

Fig. II.11. Calculated stored potential energy resulting from a 1 Hz square-wave displacer motion profile (experimental and simulated results shown). Operating conditions were approximately 21 bar mean operating pressure and 185 K temperature difference between the expansion and contraction sides of the engine section.

II.6.2 Sinusoidal Vs. Square-Wave Motion Profiles

The summary findings of reservoir pressure differences for 6 data sets (sinusoidal and square-wave displacer piston motion at 1, 1.5, and 2 Hz) are given in the following table. Note that the difference between simulated and experimental values is very small, within 2% of the experimental values.

TABLE II.2
SUMMARY OF FINAL RESERVOIR PRESSURE DIFFERENCES USING SINUSOIDAL AND SQUARE-WAVE DISPLACER MOTION PROFILES AT VARYING FREQUENCIES

Frequency	Sinusoidal Motion		Square-Wave Motion	
	Data	Model	Data	Model
1 Hz	432.4 kPa	429.3 kPa	808.7 kPa	791.3 kPa
1.5 Hz	544.9 kPa	539.5 kPa	798.9 kPa	796.2 kPa
2 Hz	552.6 kPa	542.6 kPa	718.2 kPa	720.3 kPa

Overall, data sets using square-wave displacer motion profiles resulted in larger pressure differences between the reservoirs and greater amounts of stored potential energy than data sets using sinusoidal displacer motion profiles. Fig. II.12 and Fig. II.13 further illustrate this conclusion for the sample 1 Hz data set.

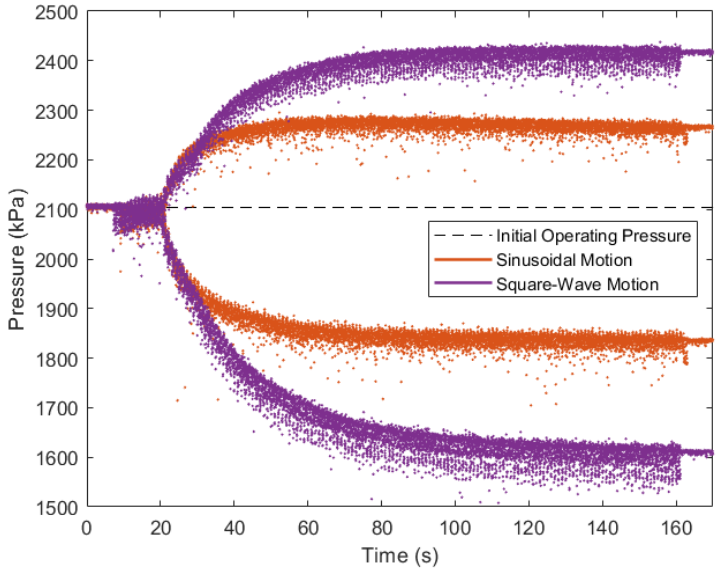

Fig. II.12. Reservoir pressure comparison of 1 Hz data sets actuated by sinusoidal and square-wave displacer motion profiles.

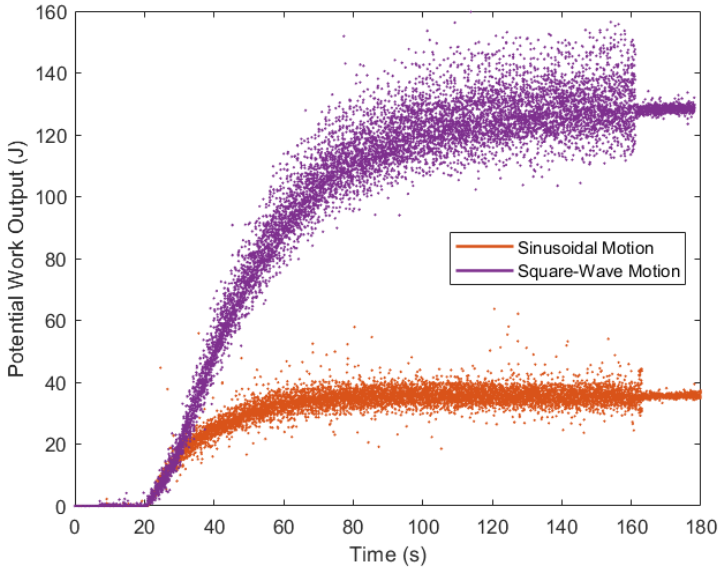

Fig. II.13. Potential work output comparison of 1 Hz data sets actuated by sinusoidal and square-wave displacer motion profiles. Maximum computed power output averaged over one period: 2.83 watts for the sinusoidal data set and 4.12 watts for the square-wave set.

II.6.3 Observed Effects of Frequency on Work Output

In the case of data sets using sinusoidal displacer motion profiles, the device's performance,

as measured in total work output, increases with greater frequency. Though our device's frequency is limited to 2 Hz, the data suggests that there is a limit to how far increased frequency can boost performance (Fig. II.14). At higher frequencies, the magnitude of the displacer piston's tracking response to a sinusoidal input was observed to decrease slightly, diminishing the device's stroke length, and likely contributing to limited potential work output.

In the case of data sets using square-wave displacer motion profiles, results indicate that the total work output is higher compared to a sinusoidal-wave profile, at every frequency tested. The data also indicates that increased frequency of requested square-waves actually has a reverse effect: greater frequency leads to less overall stored energy than lower frequencies of square-waves. This counter tendency can be explained by examining the recorded displacer motion data in response to sinusoidal and square-wave reference signals. In the case of sinusoidal references, waves of greater than 1 Hz frequency continue to match the reference signal closely (Fig. II.15); however, in the case of square-wave signals, increased operating frequency adds to the deterioration of the motion profile (Fig. II.16), which is associated with a negative effect on performance at increased frequencies due to the response being "less square". However, responses to square profiles result in higher overall work output compared to the same frequency of a sinusoidal displacement profile. The overall conclusion is that the more "square" a profile is, the better.

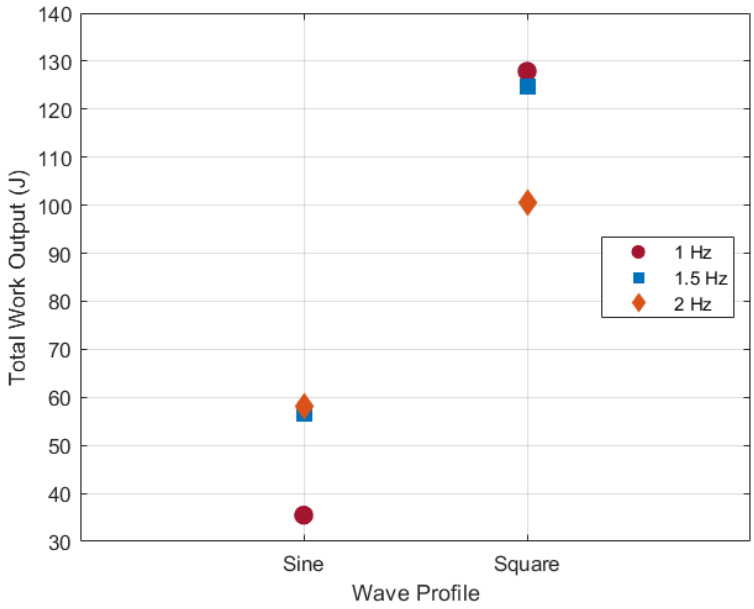

Fig. II.14. Total work output comparison of data sets of varying frequency, actuated by sinusoidal and square-wave displacer motion profiles.

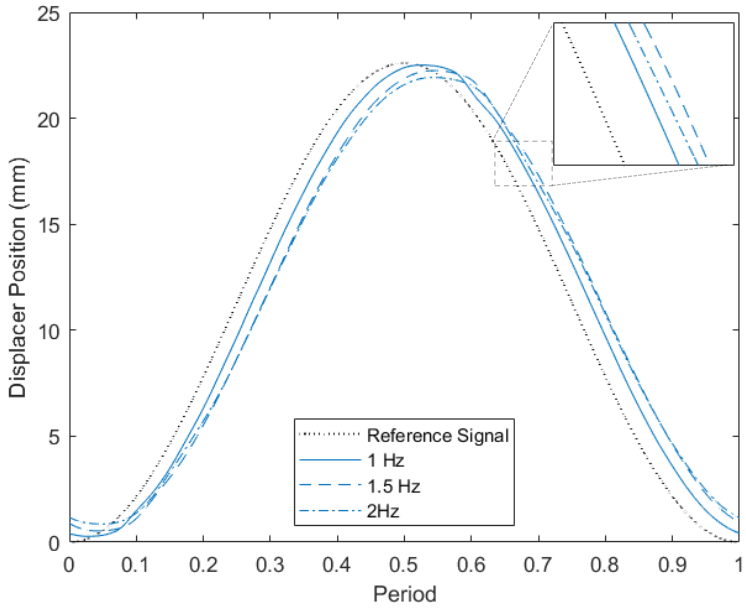

Fig. II.15. Sample comparison of recorded displacer motion data in response to sinusoidal reference signals of varying frequencies.

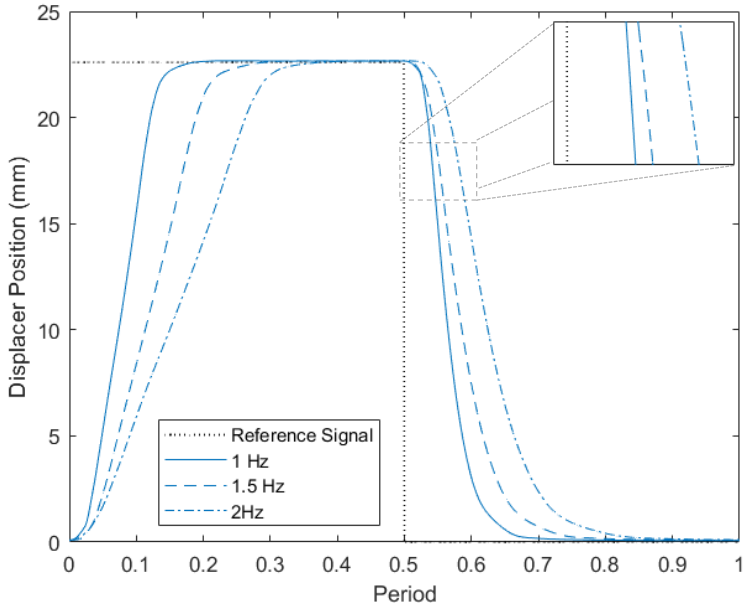

Fig. II.16. Sample comparison of recorded displacer motion data in response to square-wave reference signals of varying frequencies.

II.6.4 Corrected Square-Wave Displacer Motion Profiles and Elevated Performance at Increased Frequencies

The recorded displacer position data in response to a 1 Hz square-wave reference signal (the least-deteriorated waveform from Fig. II.16) was replicated at 1.5 Hz and 2 Hz frequencies, creating "corrected" square-wave displacer position data without further deterioration of the motion path. Using this position data and the model, simulations predict that increasing cycle frequency will also lead to increased thermocompressor performance in square-wave-driven devices (Fig. II.17), in consonance with observed device performance as actuated by sinusoidal displacer motion signals at increasing frequencies.

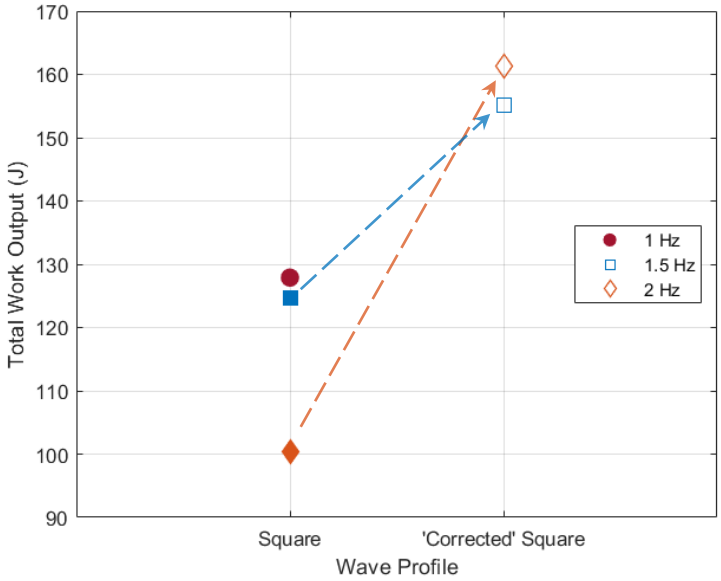

Fig. II.17. Predicted total work output of the thermocompressor if actuated by corrected 1.5 Hz and 2 Hz square-wave displacer motion profiles, which exhibit no deterioration in their motion paths from that of a recorded displacer position response to a 1 Hz reference signal.

II.7 Conclusion

The controlled displacer piston concept has been implemented in a low-frequency Stirling platform. Also, the design, first-principles dynamic model, and experimental setup of a Stirling thermocompressor has been described and the proposed dynamic model has been validated with experimental data. The model closely matches experimental data for sinusoidal and square-wave

displacer motion profiles and because the model is able to incorporate an arbitrarily-specifiable displacer motion profile, it can be used to optimize such motion with respect to desired thermocompressor power, efficiency, or other performance metrics Using a controlled displacer piston profile, we have experimentally demonstrated 1.45X higher peak cycle power, 3.6X higher work output and 1.9X higher pressure delivery. The experimentally validated, first-principles model presented in this paper can be used to optimize the future design and displacer control of active thermocompressor devices of a similar design.

II.8 Acknowledgements

This work was funded in part by a National Science Foundation Engineering Research Center (Grant Number: EEC-0540834).

Chapter III

Active Stirling Thermocompressor: Enthalpy, Efficiency and Dead Volume as a Function of Displacer Motion Profile

III.1 Preface

The text of this chapter is pending submission and review:

> Thomas, S. and Barth, E. J. (2022) Active Stirling Thermocompressor: Enthalpy, Efficiency and Dead Volume as a Function of Displacer Motion Profile Active Stirling Thermocompressor: Modelled Enthalpy, Efficiency and Dead Volume Mitigation, ***In Preparation for Applied Energy***

III.2 Introduction

Optimizing Stirling device performance has long been an active field of research and consequently, a wide range of strategies has been explored for improving device performance. One line of inquiry challenges the traditional Stirling piston arrangement, which has historically been a coupled pair of sinusoidally-actuating pistons (a displacer and a power piston) linked kinematically to one another by means of a flywheel [41]. Alternative designs include the Ringbom, Martini, and free-piston engines. In a Ringbom engine [22], the power piston is kinematically attached to a flywheel while the decoupled displacer actuates in response to changing pressure dynamics within the engine cylinder. Martini engines [23] are similar except the displacer piston is linked kinematically and the power piston dynamically reacts. The highly-successful free-piston engine [24], whose output mechanical power is typically transformed into electric power by means of a linear alternator, does away with traditional kinematic linkages entirely and both displacer and power piston move in response to changing engine dynamics.

While much work has been done to improve the performance of these passive, uncoupled piston arrangements (e.g., adjusting the dynamics of linear alternators to control the free-piston engine's power piston's stroke length to match desired voltage outputs [42-44]), more recent innovations have led to the development of an "active" or "driven" Stirling engine concept, whereby the displacer piston's motion is independently controlled and can dictate the

thermodynamics of the engine directly. In some instances, the controlled displacer piston retains the fundamental sinusoidal nature of the traditional displacer path: for example, Tavakolpour-Saleh et al [25-26] altered the sinusoidal frequency of a controlled displacer engine to better handle loading conditions and perform at resonance.

Other researchers challenge the sinusoidal motion path (itself a design compromise [45]) altogether. The developing consensus is that more square-like (hereafter simply referred to as "square-wave") displacer motion-paths are better suited to improving Stirling performance: Craun and Bamieh [30] used optimal periodic control theory to compute an ideal frequency and path for a displacer piston to follow in order to maximize net power from in a specific beta-class arrangement, and the algorithm produced a square-wave displacer motion profile. Briggs et al [27] augmented the traditional free-piston piston motion with 2^{nd} and 3^{rd} order harmonics, creating a non-sinusoidal waveform to increase performance. And Gopal, Duke, and Clucas [28-29] proposed and experimentally demonstrated that adding dwell time to a displacer motion sequence (whereby the displacer piston remains motionless at its extreme positions for a percentage of the operating period) increased work output.

A key assumption behind the work presented in these publications is that the theoretical and experimental platforms reflect situations where Stirling engines operate at high frequencies. In Gopal, Duke, and Clucas' work, for instance, momentarily suspending the displacer piston's motion allows the working fluid to interact with greater amounts of heat, whose flow dynamics ordinarily have less time to occur when competing with the velocity of the displacer piston. At low operating speeds where heat flow occurs much more quickly relative to the displacer's velocity, this presupposition does not hold and augmenting the displacer piston's motion path may not necessarily be beneficial. Though not common, such low-frequency engines are useful in low-temperature-difference (LTD) applications (for instance, power generation using solar, geothermal, or waste-heat sources), which require Stirling engines to have large surface areas (and large volumes) to effectively make use of all available heat [46]. The moving elements of these Stirling engines must also be larger and consequently must operate at lower frequencies. Anecdotally, a survey of the few LTD Stirling systems that have actually been built with power outputs greater than just a few watts found that the engines presented operated at frequencies less than 3 Hz [47].

In a previous work, the authors experimentally validated the active Stirling engine concept on a low-frequency Stirling platform, the lesser-known Stirling thermocompressor [48]. There it was shown (Figs. III.2 and III.3 below) that actuating the device with square-wave displacer motion profiles at low frequency resulted in greater energy output than by actuating the device with sinusoidal displacer motion profiles at the same frequency. Using the first-principles, third-order differential model presented in that work, we will further examine the implications of those general findings in terms of the thermocompressor's periodic energy inputs and losses, cyclic efficiency, and enthalpy output. Further, we will experimentally-show that the controlled displacer piston concept can be further exploited to retain Stirling thermocompressor performance in light of necessary dead volume.

III.3 Modelled Square-Wave Displacer Motion Advantage

Though classified as a Stirling device due to its capacity to drive pressure oscillations by shuttling working fluid between hot and cold sides of an engine, the thermocompressor (Fig. III.1) differs from traditional Stirling engines in one crucial respect: it's output isn't mechanical but pneumatic as a pair of check valves connected to high- and low-pressure reservoirs replaces the usual power piston, facilitating mass flow through the device. Furthermore, the device's displacer piston is decoupled from the device's work output apparatus and independently actuated using a separate linear electric motor, allowing operators to further shape the device's thermodynamic cycle and overall performance.

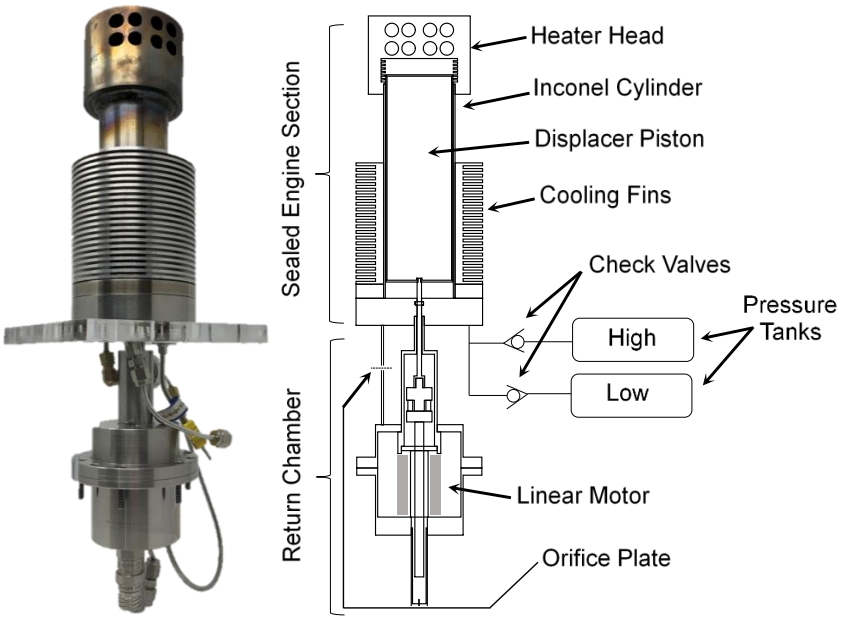

Fig. III.1. Photo (left) and schematic (right) of the Stirling thermocompressor (check valves and pressure tanks are not included in the photo). Pressure oscillations within the sealed engine section due to the displacer piston shuttling mass between the hot and cold sides of the engine result in mass transferring from the low-pressure to high-pressure reservoir tanks.

A third-order model was proposed and experimentally validated on the thermocompressor platform and the authors demonstrated in simulation and experiment that at uniform operating frequencies (1-2 Hz), novel displacer motion profiles, namely, the square-wave motion profile, greatly increased device performance. Figs. III.2 and III.3 are reproduced from [48] as representative samples of the conclusions from that work.

Figs. III.2 and III.3 show that greater amounts of energy are transferred to the high-pressure reservoir tank from the thermocompressor when the device's displacer piston is actuated by square-wave motion profiles than when actuated by sinusoidal motion profiles, as evident by higher theoretical work output and a greater pressure difference established between the reservoirs using square-wave displacer motion profiles. The following analysis using the validated, first-principles model demonstrates the differences between thermocompressors employing either sinusoidal and square-wave displacer motion profiles at uniform operating frequency (1 Hz) by exploring enthalpy flow between the thermocompressor and reservoirs, cyclic energy inputs and outputs, overall cyclic efficiency, and enthalpy flow timing during the expansion and contraction phases.

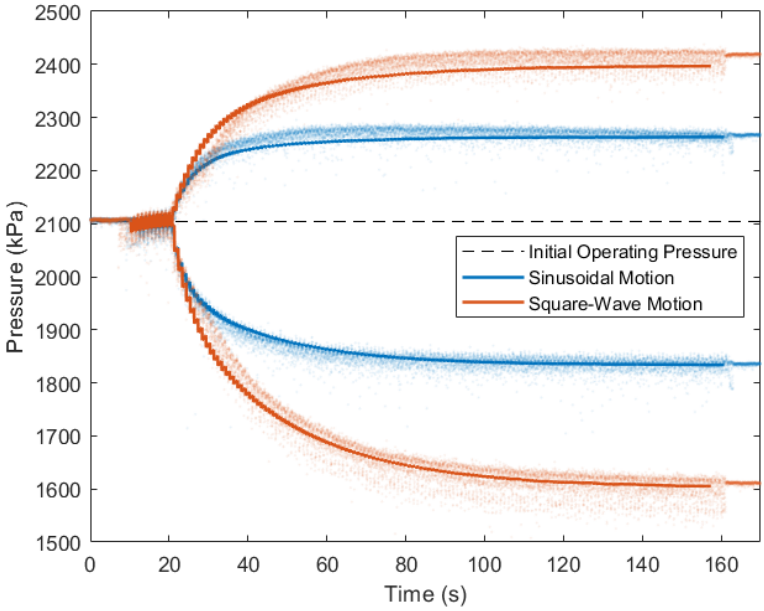

Fig. III.2. Measured (faded scatter) and modelled (bolded line) pressure within the high- and low-pressure reservoirs over time for a 1 Hz sequence driven by sinusoidal or square-wave displacer motion profiles. Starting engine pressure was roughly 21 bar, the working fluid was helium, and the temperature difference across the device was approximately 185 degrees K. Further operating conditions are described in [48].

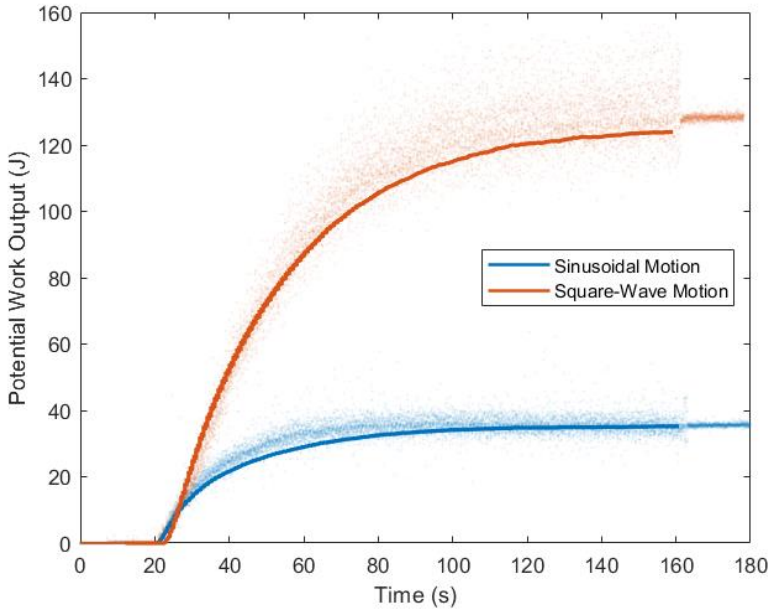

Fig. III.3. Potential work output comparison of 1 Hz data sets actuated by sinusoidal and square-wave displacer motion profiles. Starting engine pressure was roughly 21 bar, the working fluid was helium, and the temperature difference across the device was approximately 185 degrees K. Further operating conditions and details of the potential work calculation are described in [48].

Using the geometry and overall model parameters from [48], idealized representative initial conditions were chosen for the analysis under consideration in order to broadly describe the trends observed in the experimental data, though differences in loading pressure, engine temperature difference, displacer motion profile precision, etc. can influence the model's specific results. Consequently, the mean operating pressure and temperature difference of the simulation were set to 20 bar (Helium) and 150 degrees Kelvin, respectively, wherein the actual pressure and temperature varied by a trivial amount in the actual experiments presented in Figs III.2-III.3. The sinusoidal displacer motion path was modelled perfectly given the amplitude of the stroke length and an operating frequency of 1 Hz. The square-wave displacer motion profile was produced using a representative recorded response of the motor and displacer piston to a square-wave reference command, and replicating that response over the length of the simulation (175 cycles). A variable-step solver was used, with a maximum step size set at 0.1 milliseconds.

III.3.1. Engine-Reservoir Enthalpy Flow

Enthalpy flow from the engine is the only meaningful energy contribution to the high pressure reservoir; therefore, it follows that for the same amount of time, square-wave displacer motion profiles should be able to generate greater enthalpy flow to and from the reservoirs than sinusoidal displacer motion profiles. (That square wave displacer motion profiles should have a bidirectional enthalpy flow advantage is evident from a higher final high-reservoir pressure and lower final low-reservoir pressure resulting from square-wave displacer motion profiles than for corresponding sinusoidal displacer motion profiles.)

The following figures (Figs. III.4 and III.5) illustrate simulated instances of enthalpy flow between the engine and the reservoir tanks, represented by the product of the x- and y-axes (mass flow and specific heat capacity, and flow temperature, respectively). The check valves in the experimental setup prevent continuous flow between the reservoirs and the engine section, so each data point presented corresponds to an instant of enthalpy flow, usually lasting for less than a millisecond: in Fig. III.4, the average modelled duration of *output* flow for 42 instances of flow resulting from sinusoidal displacer motion was 0.96 ± 0.01 milliseconds; for 152 instances of *output* flow resulting from square-wave displacer motion, the average duration of flow was 0.61 ± 0.02 milliseconds. In Fig. III.5, the average modelled duration of *input* flow for 19 instances of flow resulting from sinusoidal displacer motion was 0.88 ± 0.02 milliseconds; for 90 instances of

input flow resulting from square-wave displacer motion, the average duration of flow was 0.69 ± 0.02 milliseconds.

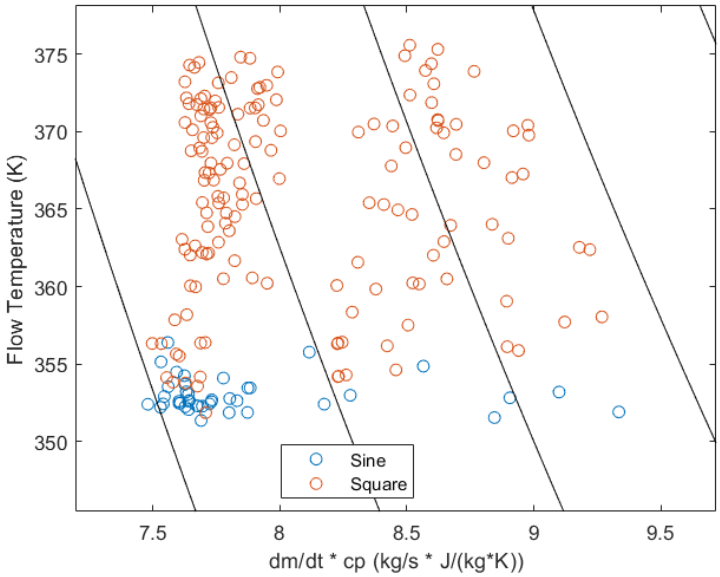

Fig. III.4: Enthalpy flow from engine to reservoirs (positive mass flow is mass entering the high pressure reservoir). Shown also are lines of constant enthalpy flow at 250 J/s apart. There were 42 instances of flow for the sinusoidal wave profile, and 152 instances for the square-wave profile. The plot shows a higher modeled flow temperature for the square-wave profile, signaling a better heat transfer mechanism and hence better performance.

From Fig. III.4, the range of positive enthalpy flow from the thermocompressor to the high-pressure reservoir for simulations resulting from sinusoidal and square-wave displacer motion profiles very nearly overlap, despite the fact that instances of output enthalpy flow generally have higher temperatures when generated by square-wave displacer motion profiles. On average, instances of enthalpy flow generated by square-wave displacer motion profile have slightly higher power delivery (2,950 ± 10 J/s) than those generated by sinusoidal profiles (2,840 ± 70 J/s). But more tellingly, the number of modelled instances of enthalpy flow generated by square-wave displacer motion profiles overshadows the number of instances generated by sinusoidal profiles: though time is not reflected in Fig. III.4-III.5, the square-wave motion profile continues to pump mass through the thermocompressor long after the flow resulting from a sinusoidal motion profile has ceased. Because the average enthalpy delivered per instance of flow is very similar between the two displacer motion profiles, the greater number of enthalpy flow events generated by square-wave displacer motion profiles in the same amount of time equates to a greater total amount of energy imparted to the high-pressure reservoir.

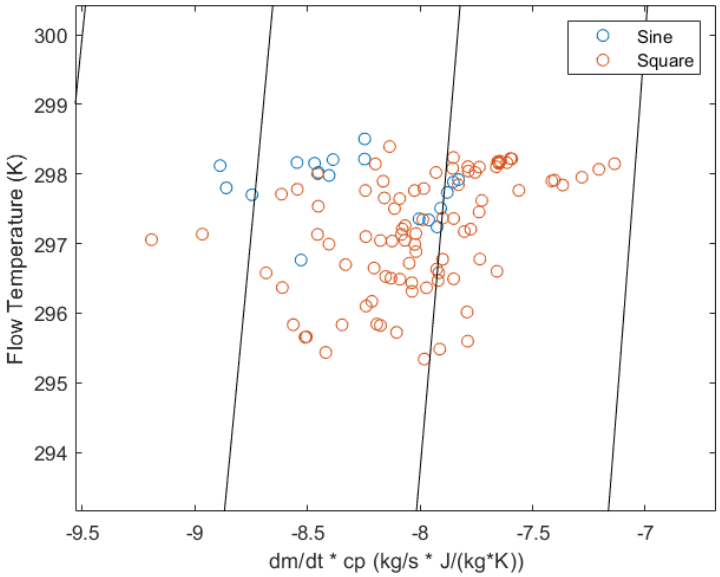

Fig. III.5. Enthalpy flow from reservoirs to engine (negative mass flow is mass leaving the low pressure reservoir). Shown also are lines of constant enthalpy flow at 250 J/s apart. There were 19 instances of flow for the sinusoidal wave profile, and 90 instances for the square-wave profile. The model shows slightly better heat rejection for square-waves and hence better low pressure intake performance.

Fig. III.5 illustrates enthalpy flow moving from the low-pressure reservoir to the thermocompressor's engine section. Here, the range of positive enthalpy flow for simulations resulting from sinusoidal displacer motion profiles is slightly smaller than the range resulting from square-wave displacer motion profiles, though on average, instances of enthalpy flow generated by square-wave displacer motion profile have slightly lower power delivery (2,380 $\pm$ 10 J/s) than those generated by sinusoidal profiles (2,470 $\pm$ 10 J/s). Once again, because the average enthalpy extracted from the low-pressure reservoir per instance of flow is very similar between the two displacer motion profiles, the greater number of enthalpy flow events generated by square-wave displacer motion profiles in the same amount of time results in a greater total amount energy extracted from the low-pressure reservoir. Like Fig. III.4, the square-wave motion profile continues to pump mass through the thermocompressor long after the flow resulting from a sinusoidal motion profile has ceased

III.3.2. Cyclical Energy Inputs

The fact that bidirectional enthalpy flow events happen for longer (as the reservoir tanks continue to differ in pressure) in simulations involving a square-wave actuated displacer piston implies that in these cases, the thermocompressor's oscillating internal energy more often exceeds the high and low energy thresholds of the high- and low-pressure reservoirs, maintained by the check valves. This could be accomplished if the thermocompressor absorbs more cyclic input energy during square-wave-actuated displacer sequences than sinusoidal ones, but the model suggests this isn't the case (Figs. III.6-III.9).

Energy imparted to the thermocompressor's working fluid comes in three forms: heat absorbed by the expansion side and regenerative channel, work done on the working fluid by the loose-fit displacer piston, and enthalpy flow coming from the low-pressure reservoir. Fig. III.6 below accounts for the total heat absorbed by the working fluid over each of the thermocompressor's contraction-expansion cycles, for simulations utilizing sinusoidal or square-wave displacer motion profiles. For reference, a cycle's contraction phase is characterized by a decrease in engine pressure as the displacer piston moves from bottom-dead-center to top-dead-center, and a cycle's expansion phase is just the opposite: an increase in engine pressure as the displacer piston moves from top-dead-center to bottom-dead-center.

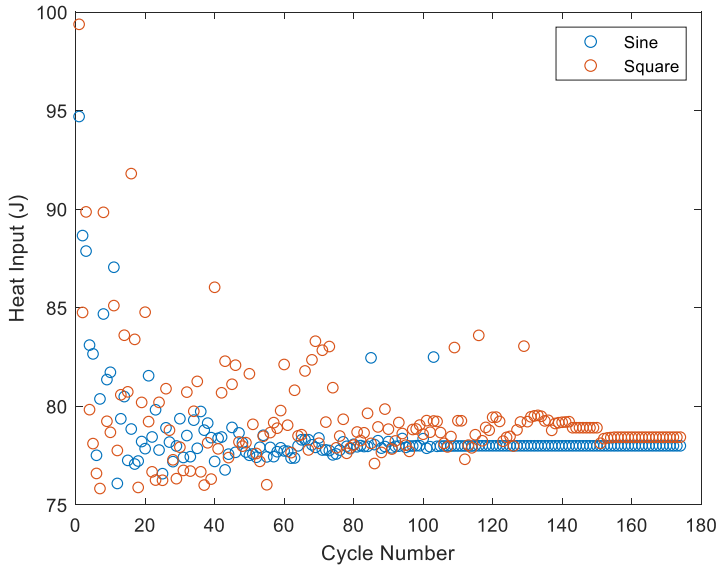

Fig. III.6. Total heat imparted to the working fluid for each cycle in a 175-cycle sequence for models incorporating a 1 Hz sinusoidal and square-wave displacer motion profile. Absorption of heat similar for both profiles. This furthers the case that higher performance resulting from square waves is due to better usage of the absorbed heat.

As the model shows, using a sinusoid-actuated displacer piston and a square-wave actuated displacer piston, the amount of heat absorbed by the working fluid for each cycle is very similar over time for both sequences. Though there is some variability at the beginning of the 175-cycle sequence for each displacer motion profile, a final input heat amount is achieved once the sequence achieves steady-state operation (78.0 J and 78.4 J, for sinusoidal and square-wave sequences, respectively). Fig. III.7 below shows a histogram of the input heat energy distribution among the cycles, showing that the average heat absorbed by both sinusoidal and square-wave sequences are very similar, with a cyclic difference of roughly one Joule, insufficient to account for the overall differences in work output between sinusoidal-motion and square-wave motion sequences.

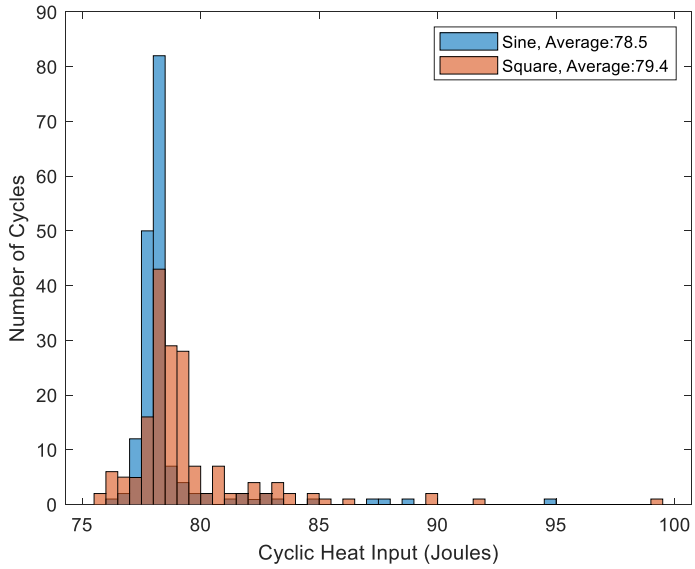

Fig. III.7. Distribution of the total heat imparted to the working fluid for each cycle in a 175-cycle sequence for models incorporating a 1 Hz sinusoidal and square-wave displacer motion profile. The bin width shown is 0.5 Joules. As in Fig. III.6, the total heat imparted to the working fluid under both motion sequences is nearly equal, implying that a square-wave motion profile's advantage lies in its better usage of the absorbed heat.

Fig. III.8 shows the cyclic work done by the displacer piston on the working fluid. Though there are clear differences between the energy imparted from the displacer piston to the working fluid for sinusoidal-motion sequences (0.06 J) and square-wave motion sequences (0.25 J) – in the latter case, a higher work contribution is correlated to the higher energy necessary to actuate the displacer through a square-wave sequence – the overall scale of the displacer piston's input energy contribution is minimal when compared to the heat and enthalpy inputs.

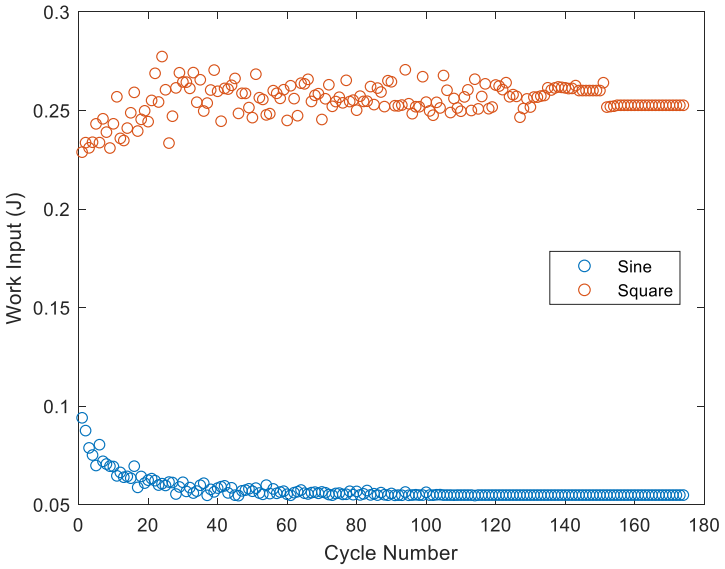

Fig. III.8. Total work imparted to the working fluid for each cycle in a 175-cycle sequence for models incorporating a 1 Hz sinusoidal and square-wave displacer motion profile. Though a clear difference between the work input absorbed by sinusoidal and square-wave motion profiles exists, the amounts are trivial compared to other energy input quantities per cycle.

As noted in Fig. III.5, the number of instances of modelled enthalpy flow between the reservoirs and the engine varies between sequences actuated by sinusoidal or square-wave displacer motion profiles. Consequently, enthalpy flow is not a consistent energy input for every cycle. According to the data presented in Fig. III.9, total input enthalpy is higher for early cycles than for later ones, for both sinusoidal and square-wave sequences, but long-term input enthalpy levels out at approximately 2 Joules for both sequences. The average enthalpy input for the simulation conditions under investigation for sinusoidal displacer motion is 2.9 ± 0.3 J for 14 cycles exhibiting flow, and 3.3 ± 0.4 J for 43 cycles exhibiting flow for square-wave displacer motion. While enthalpy input represents an energy input an order of magnitude over the displacer's work contribution, it is far less than the heat imparted to the working fluid through the heater head and regenerative channel, the annular space between the device's Inconel cylinder and inner displacer piston, connecting the hot and cold sides of the engine.

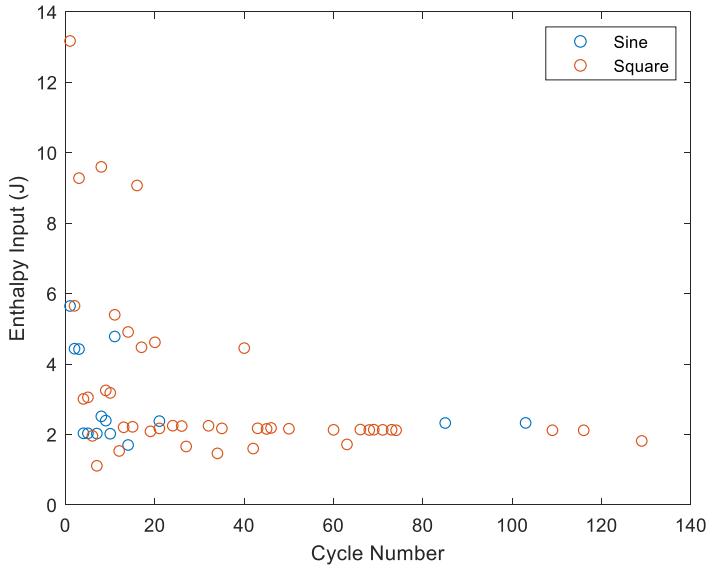

Fig. III.9. Total enthalpy imparted to the working fluid for each cycle in a 175-cycle sequence for models incorporating a 1 Hz sinusoidal and square-wave displacer motion profile.

III.3.3. Cyclical Efficiency

When output enthalpy events occur, sequences utilizing square-wave displacer motion profiles exhibit overall greater cyclic efficiency than their sinusoidal counterparts. In this discussion, efficiency is defined as the thermocompressor's (engine + return chamber) cyclic useful energy output (enthalpy flow to the high-pressure reservoir) per the thermocompressor's total cyclic energy input (heat input, work input, and enthalpy input from the low-pressure reservoir). Fig. III.10 plots the cyclic efficiency of the simulated sinusoidal and square-wave displacer motion sequences – cycles with zero efficiency (i.e., no output enthalpy flow) are not shown.

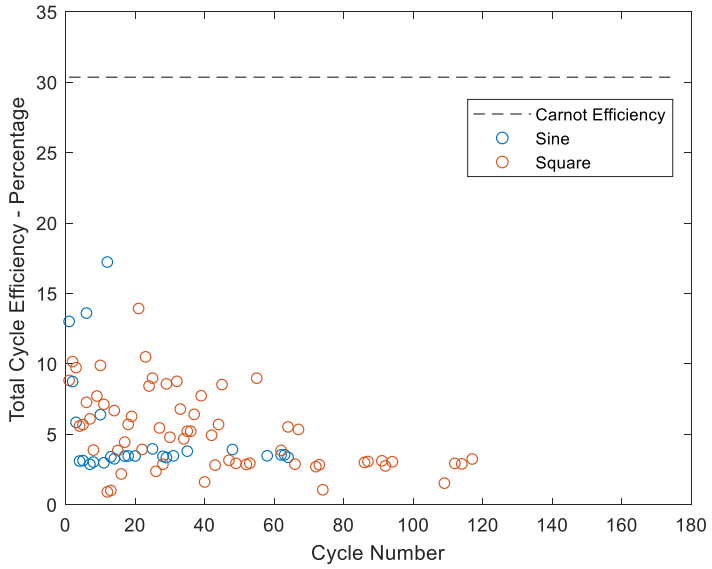

Fig. III.10. Thermocompressor efficiency for a sequence of 175 cycles, actuated by either a sinusoidal or square-wave displacer motion profile. Theoretical Carnot efficiency is also shown, given the temperature conditions specified.

The efficiencies of both sinusoidal and square-wave sequences vary widely during the earlier cycles of the sequence before reaching a steadier value. Neither sequence exhibits more than a few outlier cycles that show efficiencies above 13% (Fig. III.11), and after removing those outliers from consideration, the average sinusoidal sequence efficiency is 3.9 ± 0.3 % for 23 cycles exhibiting enthalpy output. The average square-wave sequence efficiency is 5.1 ± 0.3 % for 61 cycles exhibiting enthalpy output. Though square-wave sequences tend to be more efficient than sinusoidal ones, the greater number of cycles in the square-wave sequence that exhibit meaningful enthalpy output is more highly correlated with greater modelled and experimentally-validated energy output.

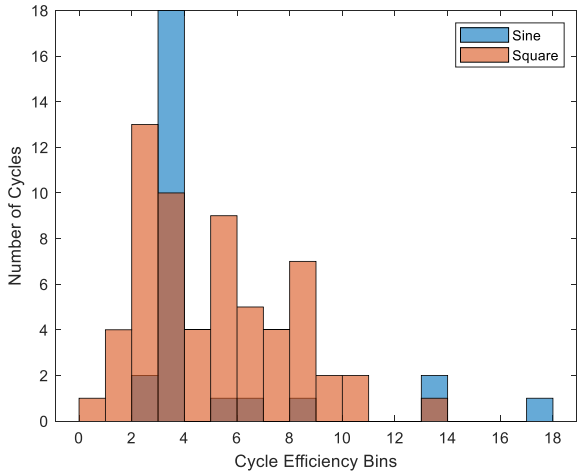

Fig. III.11. Histogram distribution of thermocompressor efficiency for a sequence of 175 cycles, actuated by either a sinusoidal or square-wave displacer motion profile.

III.3.4. Output-Input Enthalpy Flow Timing

In addition to examining sinusoidal and square-wave sequences on a cycle-by-cycle level, the model is also able to glean insights into the conditions leading up to an engine enthalpy output or input event, further delineating the advantages of square-wave displacer motion profiles from sinusoidal ones. Sequences using a square-wave displacer motion profile not only exhibit more instances of enthalpy flow than their sinusoidal counterparts, but enthalpy flow also occurs earlier within a period for square-wave sequences, both for output enthalpy flow (during the expansion cycle, from half of the period until the end of the period – Fig. III.12) and input enthalpy flow (during the contraction cycle, from the beginning of the period until half of the period – Fig. III.13). As shown below, output flow events occur on average at 0.57 ± 0.00 of the period for square-wave sequences, as opposed to 0.85 ± 0.01 of the period for sinusoidal sequences. Input flow events occur on average at 0.07 ± 0.00 of the period for square-wave sequences, as opposed to 0.29 ± 0.02 of the period for sinusoidal sequences.

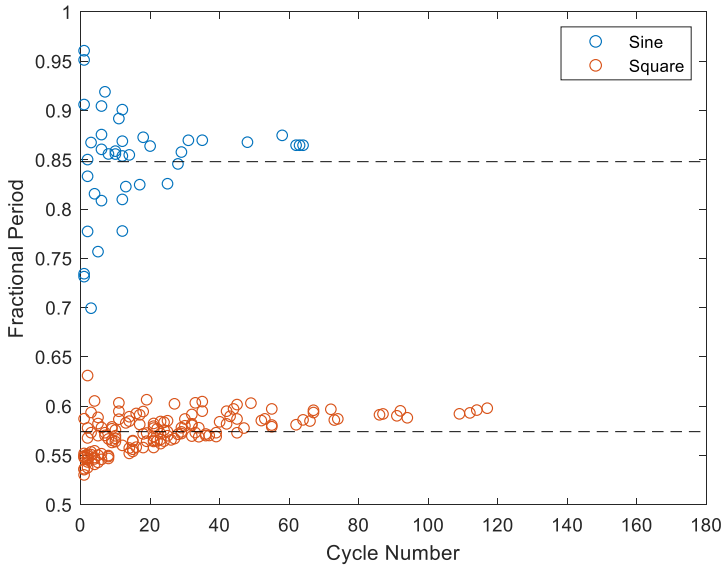

Fig. III.12. Occurrence of output enthalpy flow events within a cycle's expansion phase relative to the cycle's period and cycle sequence number. Enthalpy flow occurs sooner within a square wave's period, when pressure is still relatively high within the engine, leading to more enthalpy flow events.

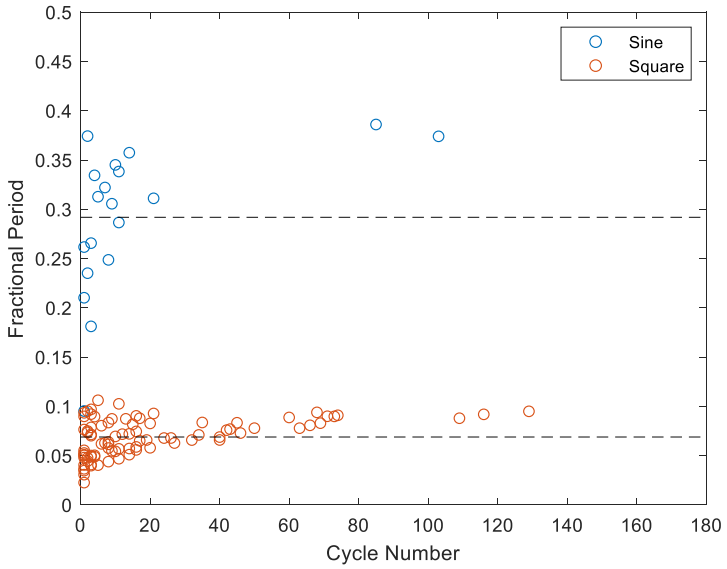

Fig. III.13. Occurrence of input enthalpy flow events within a cycle's contraction phase relative to the cycle's period and cycle sequence number. Enthalpy events occur sooner for square wave motion profiles, relative to sinusoidal ones, as the temperature in the engine cools quicker, and pressure drops lower, encouraging more enthalpy flow events for square waves.

Enthalpy output occurs when the pressure within the thermocompressor's engine section exceeds the pressure of the high pressure reservoir and the cracking pressure of the reservoir's check valve. This ascendant engine pressure is aided by power inputs (primarily, heat inputs) and hampered by power losses (heat flow out and enthalpy flow from the engine section to the return chamber). For energy to accumulate and pressure to rise, input power must be temporarily greater than power losses, in anticipation of an output enthalpy flow event. Figs. III.14 and III.15 show the primary power inputs and outputs for the expansion phase of a late-sequence cycle for sinusoidal and square sequences, when enthalpy flow between engine and reservoirs is minimized. Such late-sequence dynamics represent the thermocompressor's potential performance, after maximum and minimum pressures have been achieved. Consequently, the dynamics present underlie the transitory dynamics of earlier, intermediate cycles and are well representative of the overall mechanisms leading up to enthalpy flow. Also plotted are the average enthalpy output event periods from Fig. III.12, for sinusoidal and square-wave sequences.

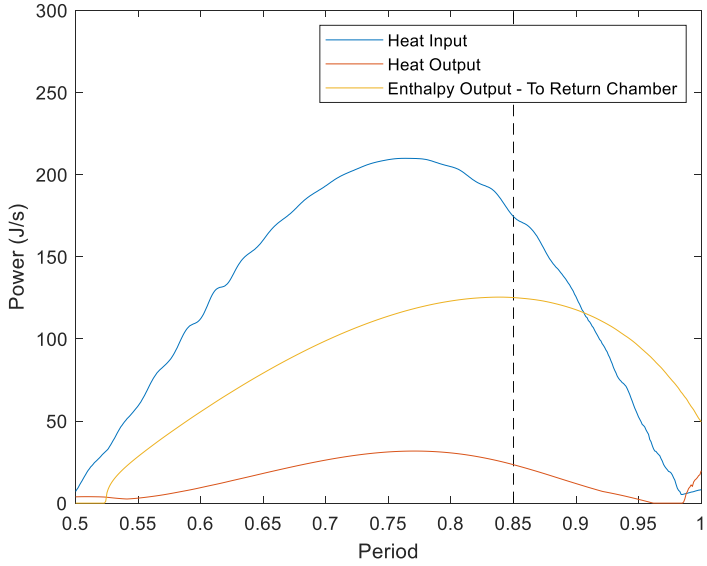

Fig. III.14. Heat input, heat output, and enthalpy output to the return chamber for the thermocompressor's engine section during the expansion phase of a late-sequence cycle for a sinusoidal displacer motion profile sequence, shown together with the average enthalpy output flow period (the vertical dotted line). Not shown are minor power inputs or losses due to the displacer piston or resulting from flow around the displacer piston.

During the expansion phase, pressure rises within the engine section as mass is shuttled from the engine's cold side to the hot side. As Fig. III.14 shows, the rate of heat input during this time increases, but so do power losses like output heat and flow from the engine section to the return chamber. The combined losses don't match or exceed the input until just before or just after the expected output (to the high-pressure reservoir) enthalpy flow event occurs, at which point pressure begins to drop within the engine. Compared to Fig. III.15, however, the rate of heat input far exceeds power losses in the case of square-wave sequences, much more than in sinusoidal ones. This is due primarily to the displacer piston's speed: mass is quickly shuttled from the cold side to the hot side before enthalpy flow or heat loss can proportionally compensate, so energy is allowed to accumulate to greater heights before an anticipated output enthalpy flow event. More energy is then allowed leave the engine as enthalpy output, rather than as heat loss or unproductive enthalpy flow to the return chamber. In the case of sinusoidal sequences, peak pressure is limited because losses rise much more in line with input increases.

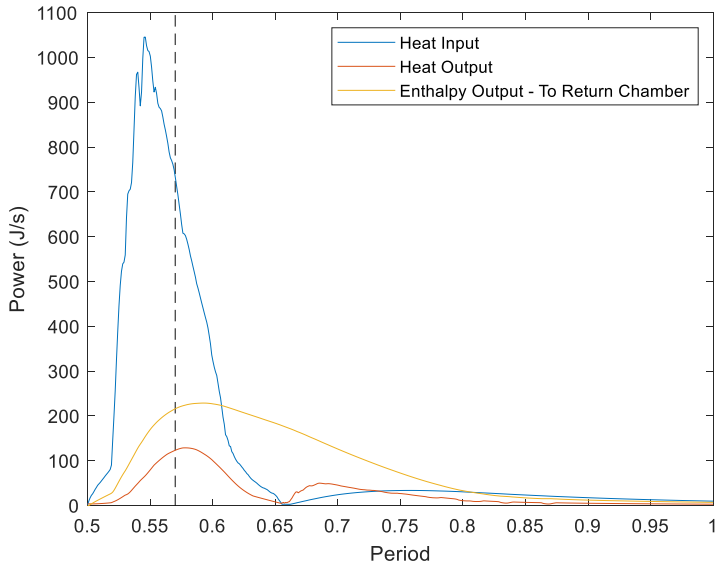

Fig. III.15. Heat input, heat output, and enthalpy output to the return chamber for the thermocompressor's engine section during the expansion phase of a late-sequence cycle for a square-wave displacer motion profile sequence, shown together with the average enthalpy output flow period (the vertical dotted line). Not shown are minor power inputs or losses due to the displacer piston or resulting from flow around the displacer piston.

Similar behavior is observed during the sequences' contraction phase (Figs. III.16 and III.17), where the working fluid loses energy as it shuffles from the hot side of the engine to the cold side, and heat losses are the primary factor in lowering the working fluid's pressure. Further heat input and enthalpy flow from the return chamber inhibit this process. Consistent with the expansion phase, the rate of loss-to-input is higher for square-wave displacer motion profiles than for sinusoidal ones before an anticipated input enthalpy flow (from the low-pressure reservoir) event, allowing the working fluid to achieve an otherwise lower pressure in order to draw in more mass from the low-pressure reservoir.

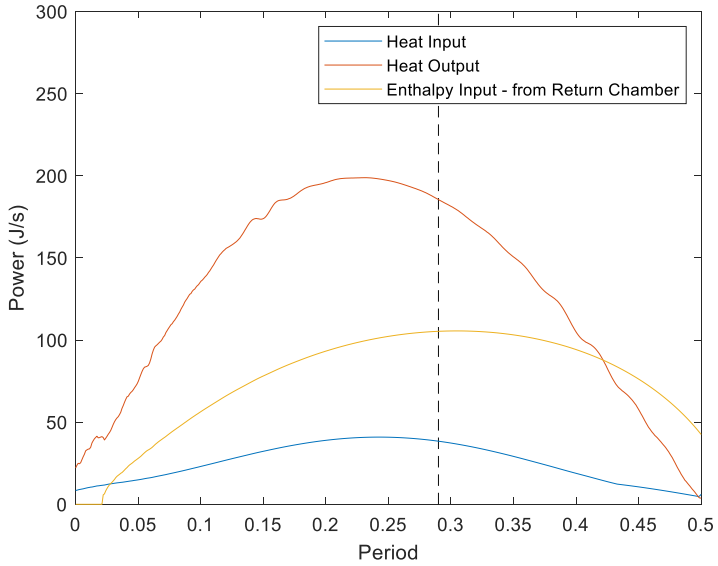

Fig. III.16. Heat input, heat output, and enthalpy output to the return chamber for the thermocompressor's engine section during the contraction phase of a late-sequence cycle for a sinusoidal displacer motion profile sequence, shown together with the average enthalpy output flow period (the vertical dotted line). Not shown are minor inputs or losses due to the displacer piston or resulting from flow around the displacer piston.

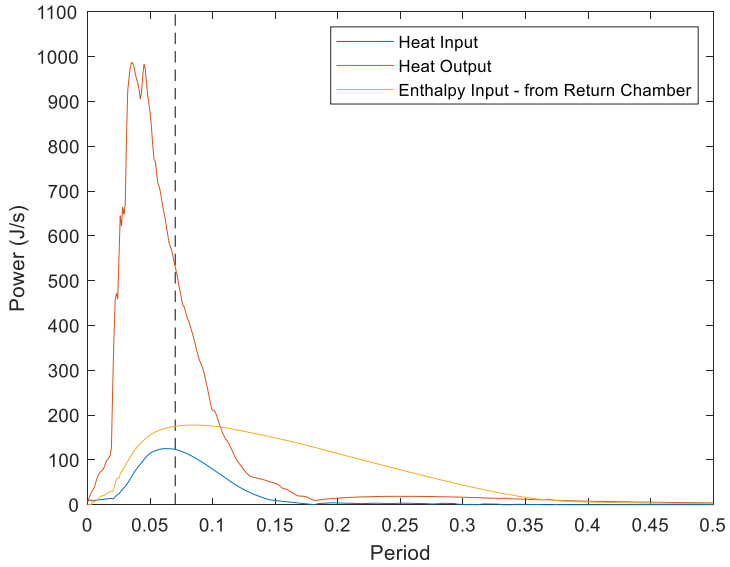

Fig. III.17. Heat input, heat output, and enthalpy output to the return chamber for the thermocompressor's engine section during the contraction phase of a late-sequence cycle for a square-wave displacer motion profile sequence, shown together with the average enthalpy output flow period (the vertical dotted line). Not shown are minor inputs or losses due to the displacer piston or resulting from flow around the displacer piston.

In summary, the rapid input of heat during a square-wave sequence's expansion phase (which significantly overshadows its power losses), and the rapid output of heat during a square sequence's expansion phase (which significantly outruns further power inputs) result in greater energy oscillation potential within the engine, and more opportunities for enthalpy flow events to occur when compared to sinusoidal sequences.

III.4 Engine-Return Chamber Enthalpy Loss Mitigation using variable Orifice Sizes

Enthalpy flow from the engine section to the return chamber removes energy from the engine and lower's the working fluid's peak pressure during the expansion phase, lessening the chances of an output enthalpy event to occur. Similarly, during the contraction phase, enthalpy flow from the return chamber to the engine section raises the working fluid's minimum pressure, further inhibiting thermocompressor-reservoir enthalpy exchange.

Such flow between the engine section and the return chamber is necessary in order to minimize the pressure difference across the motor through which the motor must actuate in order to move the displacer. This continuous, oscillating enthalpy flow ensures that the pressure within the return chamber roughly equals the engine section's average pressure.

The return chamber therefore represents necessary dead volume. And while other thermocompressor designs may be feasible which prevent engine-return chamber enthalpy exchange while still minimizing the pressure difference across the displacer's actuator, it isn't certain if such an arrangement would be an unalloyed gain in all thermocompressor applications. The author's in [49], for instance, posit that a return chamber may continue to be necessary in a multi-stage arrangement. Even so, the flow dynamics between the return chamber and engine section can be altered to increase performance without sacrificing functionality.

The flow dynamics between the engine section and return chamber are governed by an orifice plate situated in-line between the two volumes (Fig. III.18). By altering the size of the orifice plate's opening, the model and experimental evidence demonstrate that device performance can be improved by limiting the effects of dead volume. However, for the operating frequencies and orifice diameters considered, the evidence suggests that the controlled displacer piston concept has a greater impact on device performance than reducing the effects of dead volume alone.

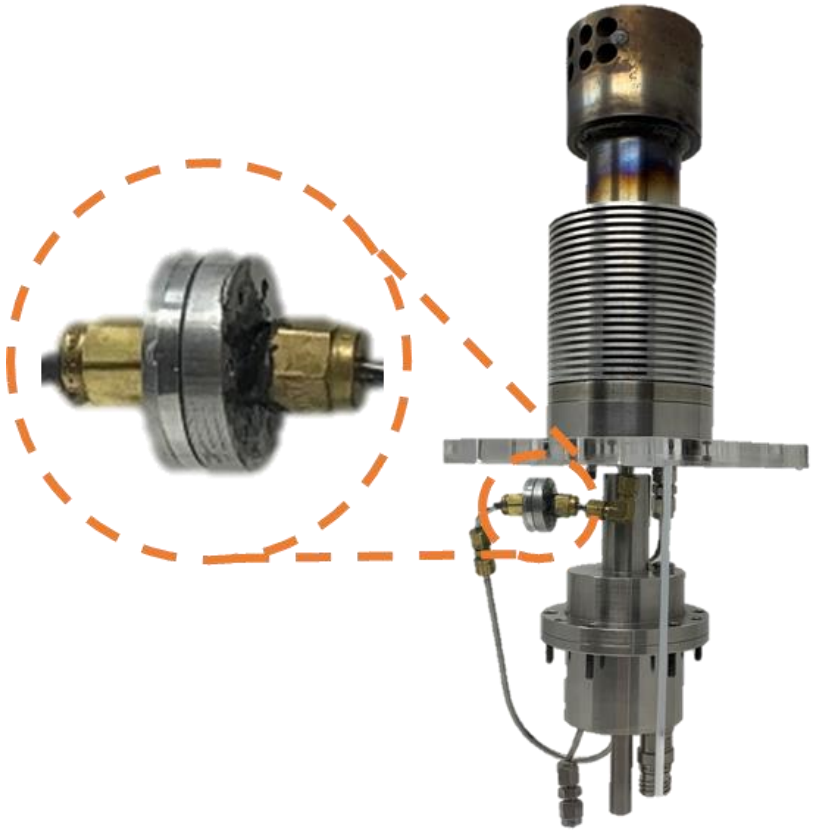

Fig. III.18. Orifice coupling installed inline between the thermocompressor's engine section and return chamber. The orifice plates fabricated with different orifice diameters were interchanged between the coupling faces.

III.4.1 Experimental Setup

Multiple orifice plates were fabricated with different orifice diameters ranging from 0.32mm to 0.20mm. A "null-flow" case was also examined, whereby the mass flow through the orifice was prevented using a solid orifice plate and the return chamber was pressurized using a separate feedline. The thermocompressor operated with an approximate 150 degrees Kelvin temperature difference between the expansion and contraction chambers, and a loading pressure of approximately 20 bar (helium). Sinusoidal and square-wave displacer motion profiles were tested at 1 and 2 Hz frequencies (three trials for each frequency and waveform) for each of the fabricated orifice plates. Pressure transducers recorded the instantaneous pressure readings in the reservoirs as a pressure difference developed between them. Further operating conditions and model parameters are outlined in [48]. The modelled and experimentally-determined final pressure differences between the reservoirs are presented in Figs. III.19-III.22 below.

III.4.2 Experiment and Modelled Results and Discussion

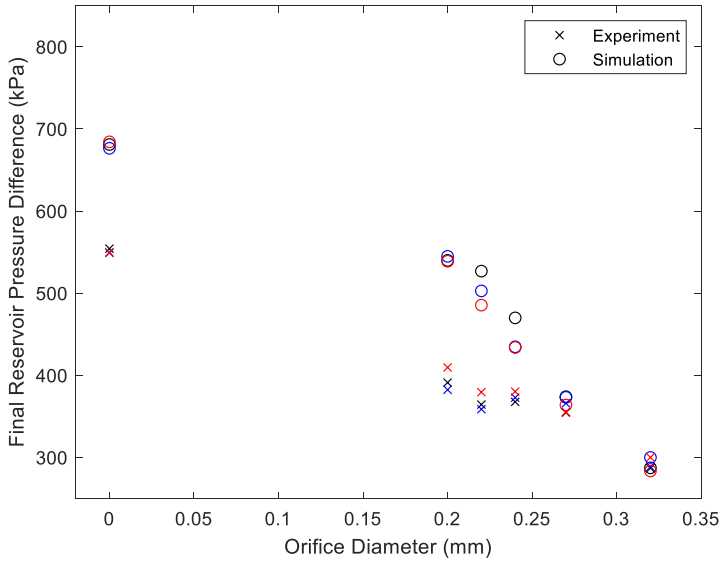

Fig. III.19. Final reservoir pressure differences of the thermocompressor system with orifices of various diameters, operating with a 1 Hz sinusoidal displacer piston motion profile. Three experimental trials for each orifice size were taken and the recorded displacer position data was fed into the model to produce the simulated results displayed.

The data taken when the device was actuated using a 1 Hz sinusoidal displacer motion profile (Fig. III.19) shows that as flow to the necessary dead volume is steadily restricted or eliminated, the overall work output of the device increases, consistent with the long-held design presupposition that dead-volume is best reduced in most circumstances. Experimentally, a 0.32 mm-diameter orifice results in an approximate 300 kPa pressure difference between the reservoirs, while when flow to the return chamber is completely eliminated, this final pressure difference nearly doubles to approximately 550 kPa. The same trend is apparent in the system's modelled response to a 1 Hz sinusoidal input, though the model overestimates the engine's output for each of the cases considered in Fig. III.19. A deviation in the data's overall trend from the 0.22 mm diameter data to the null-flow case (0 mm diameter) is likely indicative of minor manufacturing errors in the orifice plate's fabrication as well as unexpected heat-flow dynamics (especially in the null-flow case) and is consistent across all displacer motion profile regimes presented here.

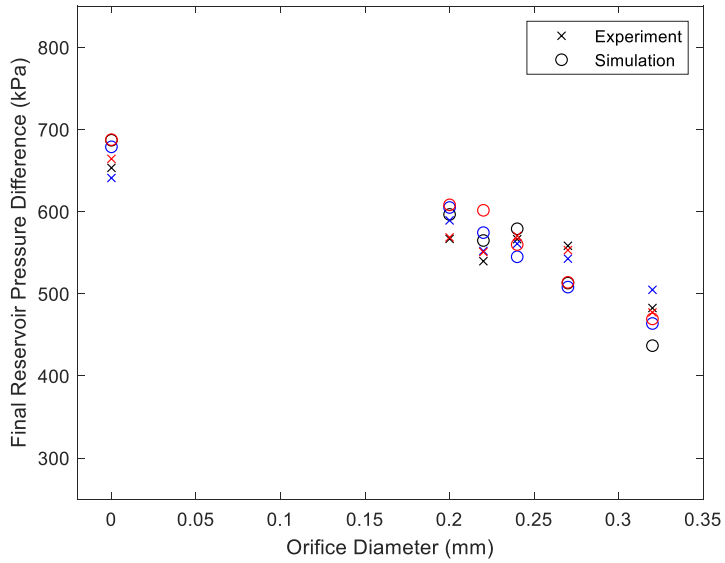

Fig. III.20. Final reservoir pressure differences of the thermocompressor system with orifices of various diameters, operating with a 2 Hz sinusoidal displacer piston motion profile. Three experimental trials for each orifice size were taken and the recorded displacer position data was fed into the model to produce the simulated results displayed.

Raising the displacer's sinusoidal actuation frequency to 2 Hz increases overall work output for all orifice diameters considered (Fig. III.20). Consistent with the developed theory, the average displacer velocity increases with increasing frequency, decreasing the available time for dead-volume enthalpy flow to negatively impact the engine's dynamics, resulting in overall greater pressure oscillations. Even at these speeds, dead volume is still a contributing factor to decreased

performance and reducing or eliminating dead volume increases work output, though the effect is not as pronounced as in the 1 Hz sinusoidal data – the measured final reservoir pressure difference with a 0.32 mm-diameter inline orifice plate is only approximately 150 kPa less than the scenario where mass is prevented from flowing to the return chamber (compared to approximately 250 kPa less using a 1 Hz sinusoidal displacer motion profile). There is also closer agreement between the model and experimental data in this and subsequent data sets.

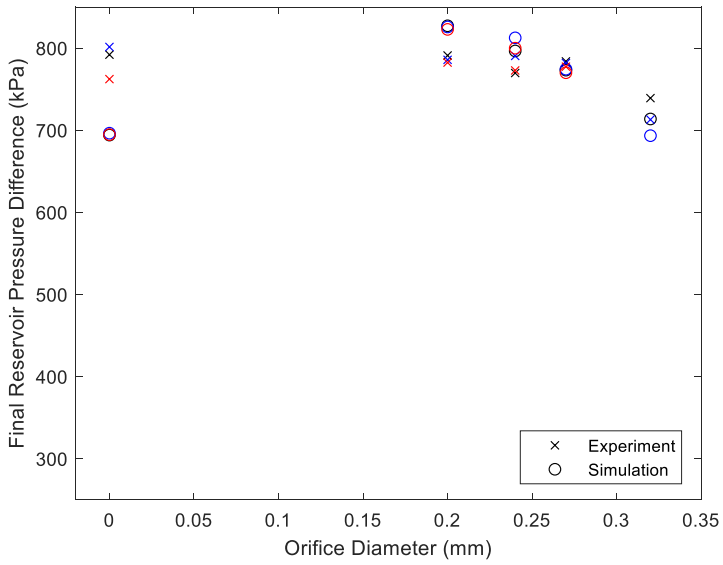

Fig. III.21. Final reservoir pressure differences of the thermocompressor system with orifices of various diameters, operating with a 1 Hz square-wave displacer piston motion profile. Three experimental trials for each orifice size were taken and the recorded displacer position data was fed into the model to produce the simulated results displayed.

Actuating the displacer piston with a square-wave motion profile (Figs. III.21 and III.22) produced the highest levels of work output across all orifice sizes under investigation. While there is some marginal improvement in eliminating flow to dead volume, work output remains high under this control scheme for the orifice sizes under consideration. The model also closely follows the experimental data with one notable exception: when flow to the return chamber is blocked entirely.

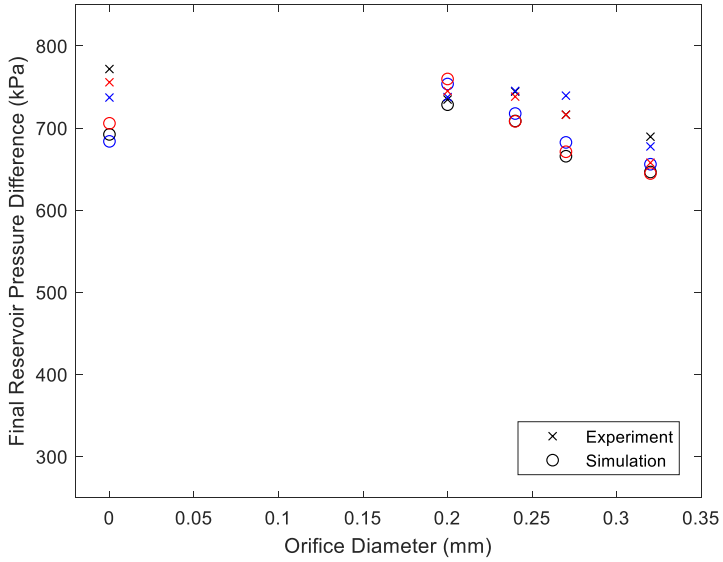

Fig. III.22. Final reservoir pressure differences of the thermocompressor system with orifices of various diameters, operating with a 2 Hz square-wave displacer piston motion profile. Three experimental trials for each orifice size were taken and the recorded displacer position data was fed into the model to produce the simulated results displayed.

Using a 2 Hz square-wave displacer motion profile, the thermocompressor exhibited similar behavior compared to the same profile at 1 Hz, albeit with a very slight decrease in work output across the varied orifice diameter configurations. This decrease is likely due to deteriorated wave profile forms (i.e., the motor and displacer's response to a 2 Hz square-wave reference command resembles a sinusoidal wave rather than a square one), as described in detail in [48]. Experimentally, dead volume is less of a problem when the thermocompressor operates with square wave displacer motion profiles overall, though the model in Figs. III.21 and III.22 above would suggest some modest performance gains could occur from minimizing (but not eliminating) dead volume. Similar to Fig III.21, model and experimental data diverge when predicting the devices performance when flow to the return chamber is eliminated.

In all cases where null flow is considered, the model predicts similar reservoir-pressure outcomes regardless of the displacer motion profile or frequency used, for the profiles and frequencies considered. However, the experimental evidence shows that displacer motion profile remains the strongest factor in raising the device's performance even when dead volume enthalpy flow is eliminated. From a modelling standpoint based on the power input and power loss analysis, the discrepancy between model and experiment likely indicates hitherto unaccounted-for heat transfer effects, dominant when dead-volume flow is significantly reduced. Such effects warrant

further investigation.

III.5 Conclusions

The validated, first-principles model shows that actuating the low-frequency Stirling thermocompressor with a square-wave displacer motion profile results in increased average cycle efficiency, though higher instances of enthalpy output resulting from square-wave displacer motion profiles are more significantly associated with increased device performance when compared to actuating the thermocompressor's displacer with a sinusoidal displacer motion profile. This preponderance of numerous enthalpy flow events is associated with high power inputs/outputs relative to power losses before a probable enthalpy flow event in the case of square-wave displacer profiles. Furthermore, when dead volume enthalpy flow losses are reduced or eliminated, the controlled displacer piston's capability has been experimentally shown to maintain a performative edge. Such conclusions further bolster the case that, just as in high-frequency Stirling devices, low-frequency Stirling devices can also benefit from a controlled displacer piston's functionality.

One question not answered by this study is whether a square-wave profile promotes a better or worse regenerator effectiveness. It can be said that experimental results indicate no degradation of regenerator effectiveness, at least at the frequencies tested. Overall, the conclusion of this study is that a more square-wave-like displacer motion profile utilizes the heat better than a sinusoidal motion profile; the device does this by using the heat to promote an inter-engine enthalpy flow event before the heat is lost to other factors (such as heat transfer loss or enthalpy loss to dead volume), in the face of a constant regenerator effectiveness.

Chapter IV

Multi-Stage Stirling Thermocompressor: Experimental and Analytical Proof-of-Concept

IV.1 Preface

Conceptual groundwork for this chapter previously appeared in:

> Thomas, S, & Barth, E J. (2017) *Multi-Stage Modeling of a Stirling Thermocompressor*. Proceedings of the ASME/BATH 2017 Symposium on Fluid Power and Motion Control, ASME/BATH 2017 Symposium on Fluid Power and Motion Control. Sarasota, Florida, USA. V001T01A060. ASME. https://doi.org/10.1115/FPMC2O17-4320

The text of this chapter is pending submission and review:

> Thomas, S. and Barth, E. J. (2022) Multi-Stage Stirling Thermocompressor: Experimental and Analytical Proof-of-Concept, ***In Preparation for Applied Energy***

IV.2 Introduction:

Approximately one third of total global energy use is consumed by the world's industrial sectors [50], and a large fraction of this energy is lost to the environs as waste heat: in the US, for example, estimates assessing the total amount of waste heat range from at least 20% to as high as 50% [1] or 60% [51] of supplied industrial-sector energy; in the EU, industrial waste heat amounts to roughly 800 TWh/year (approximately 2.7 quadrillion Btu/year) [52]. And while technologies exist to reclaim some of these losses [53], much of this potential energy source remains unrecovered: between 5 and 13 quadrillion Btu/year of waste heat energy in the US alone [1].

Technologies used to recover waste heat energy vary depending on their arrangements, the temperature of the waste heat being recovered, and in terms of their end-use output. Technologies which transform heat input into mechanical power output make use of thermodynamic cycles, such as the Rankine [52] or Kalina cycles [1]. Other methods derive electric power from waste heat sources using thermoelectric, thermo-photovoltaic, thermionic, and piezoelectric generators [54]. Still other technologies reuse waste heat to pre-heat gasses or liquids for combustion or steam-

generation, increasing overall plant efficiency. Certain waste heat recovery technologies of this type (for example, hybrid pneumatic power systems in engines [55] and air preheaters [54]) produce pressurized air as the desired output, but the end product is used to aid immediately in combustion cycles, not for general pneumatics use.

Like the copious amounts of available waste heat, the need for compressed air is present in a wide range of industrial settings. Worldwide, compressed air systems consume an average of 10%-20% of the total electricity used across manufacturing sectors [56] (among major economies, this figure is roughly 10% in the U.S. [57], the E.U. [58, 59], and China [59, 60]). In the U.S., specifically, 16% of all motor energy is dedicated to compressed air systems [61, 62]. Similarly, compressed air energy consumption plays a modest or outsized role in numerous industrial sectors, from lower demand in the iron, steel and non-ferrous metal production industries, to higher demand in the non-metallic mineral production, glass production, machinery, and transport industries [62, 63]. Compressed air systems are often notoriously inefficient, and increasing the efficiency of such systems is an active area of research [64].

To address, simultaneously, the need for greater efficiency in industrial settings, the desire to utilize abundant waste heat, and the high demand for industrial pneumatic power, the authors propose a device capable of converting heat directly into compressed air – the Stirling thermocompressor (also referred to as an oscillating thermocompressor [49]). The Stirling thermocompressor is a variant of the Stirling engine capable of producing pneumatic power directly from heat energy by replacing the Stirling engine's traditional mechanical power piston with a pair of check valves (Fig. IV.1). Due to pressure oscillations induced within the device by the thermocompressor's displacer piston which shuttles a working fluid between two volumes held at different temperatures, mass can be pumped through the device via the check valves and stored in reservoirs. The displacer piston's mechanical motion is naturally decoupled from the pneumatic power output, allowing designers to shape the device's thermodynamics directly by dictating customized displacer motion profiles at varying frequencies [15, 48].

The first patent for a Stirling thermocompressor was filed a century after Robert Stirling's original [9], and though its design has benefited from the wider world of Stirling engine research, it has hitherto failed to find a niche market for broad use, though some have been proposed: early on, for instance, the thermocompressor was considered to be a potential platform to power an artificial heart [10]; later, a multi-stage device was projected to be an efficient, noiseless air

compressor [11]; and recently, the thermocompressor has been investigated as an oscillating pressure source in pulse-tube refrigerators [12]. Nonetheless, relative to Stirling engines in general, very few devices have actually been built and tested (see [13, 15, 16] for examples) – and none as multi-stage architectures capable of compressing air from ambient conditions. Though A. A. Kornhauser [11] projected that a multi-stage device could outperform traditional compressors in minimizing noise output, but would probably not compress air efficiently enough to replace traditional compressors, recent interest in modelling and experimentally characterizing a multi-stage device has heightened [14, 48, 49]. To the authors' knowledge though, no experimental data for a multi-stage Stirling thermocompressor using air has been published.

In this paper, the authors will experimentally characterize a single-stage thermocompressor using air within the pressure range of typical industrial air compressors, up to approximately 80 psig. The authors will adapt a previously-developed third-order model [48] for air at these pressures and show how the model and experimental data converge. Using the model, the authors will predict the performance of a multi-stage system based on the architecture of the experimental prototype and discuss the appropriateness of such technology in producing pneumatic power from waste heat in industrial settings. Specific operating parameters within a multi-stage arrangement (e.g., the number of necessary stages and the operational frequency of each stage, etc.) will be produced and optimized according to arrangements requiring the least displacer-driving power input.

IV.3 Thermocompressor Platform and Model

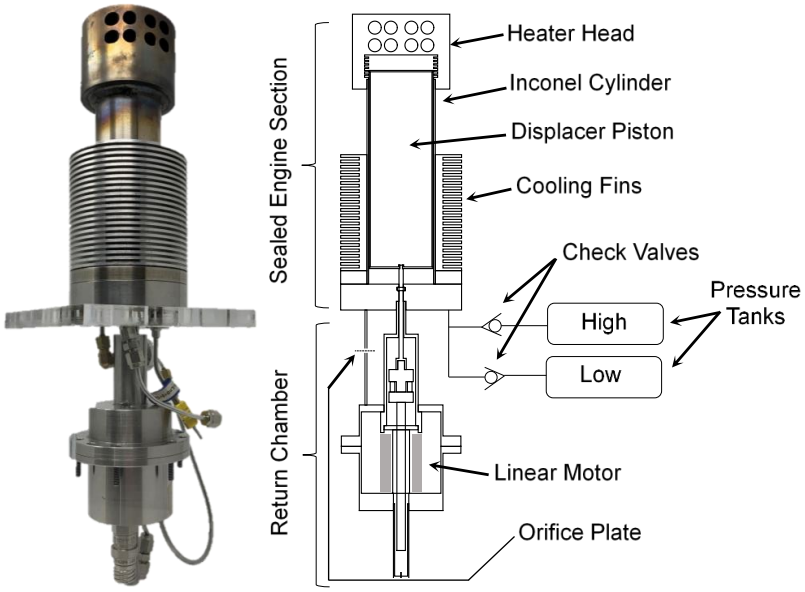

Fig. IV.1: Thermocompressor platform and design schematic

The Stirling thermocompressor platform is presented in Fig. IV.1. The heat required for producing the temperature difference which drives mass flow is generated using eight heater cartridges located within a steel heater head on the thermocompressor's expansion (hot) side. An Inconel cylinder spans the expansion and contraction (cold) sides of the sealed engine section, enclosing the loose-fit displacer piston and enclosed by aluminum cooling fins. A second chamber, dubbed the "return chamber," houses the displacer piston's linear motor. A small feed line and in-line orifice plate connects the return chamber to the sealed engine section so that the pressure within the return chamber approximates the pressure within the engine, allowing the displacer to be actuated despite high pressure fluctuations within the engine section. The linear motor drives the displacer piston along a user-defined path and frequency, not limited solely to traditional sinusoidal motion profiles. As it travels the stroke length, mass is shuttled around the loose-fit displacer piston back and forth between the expansion and contraction sides of the engine section, producing pressure oscillations. Check valves attached to a feed line at the thermocompressor's expansion side facilitate mass flow to and from the thermocompressor and external reservoirs as the pressure difference between the thermocompressor and each of the reservoirs rises and falls, dependent upon the displacer piston's position. To provide a sense of scale, a summary of the thermocompressor's primary geometric parameters is presented below (Table IV.1).

Table IV.1
Summarized Thermocompressor Geometry

Parameter Name	Value
Sealed Engine Section Volume	47.1 cm^3
Return Chamber Volume	17.0 cm^3
Upstream (Low) Reservoir Volume	1,024 cm^3
Downstream (High) Reservoir Volume	523 cm^3
Displacer Piston Area	14.6 cm
Stroke Length	2.26 cm
Inconel Cylinder Inner Diameter	4.83 cm
Orifice Plate Hole Diameter	0.20 mm
Displacer Piston Mass	205 grams

IV.3.1 Mathematical Model

The lumped-parameter, first-principles-based, third-order model consists of five primary control volumes delineated within the modelled thermocompressor's expansion and contraction sides, return chamber, and upstream and downstream reservoirs. The pressure dynamics within each of the control volumes are determined by computed heat and mass transfer rates between the control volumes and heat/mass sources, and the change in volume within those control volumes affected by the displacer piston's motion. The governing equations of these volumetric, heat flow, and mass transfer dynamics are described in greater detail in [48]. Aside from specific model parameters such as the temperature difference across the thermocompressor, geometric dimensions, and supply or starting pressure, the displacer position's motion path and frequency is the only varying input to the model – such input may be simulated or derived from recorded data from the linear motor's controller.

Critical changes to the model parameters presented in [48] are restricted to the use of air as the thermocompressor's working fluid. Relevant model constants are summarized below in Table IV.2, while the density and dynamic viscosity of the working fluid were computed continuously using (model-generated) temperature and pressure states of specific control-volumes along with a 2-dimensional look-up table.

Table IV.2
Summarized Modelling Parameters - Air

Parameter Name	Value
Specific Heat at Constant Pressure, C_p, for Air	1013 J/kg K
Specific Heat at Constant Volume, C_v, for Air	726 J/kg K
Specific Heat Ratio, Gamma, for Air	1.39
Ideal Gas Constant, R, for Air	287 J/kg K
Thermoconductivity of Air	32.35 mW/m K

IV.4 Experiment and Verification

The experimental setup was in accordance with Fig. IV.2: dry, compressed air was regulated down to a desired operating pressure and then fed into the reservoir tank on the upstream side of the thermocompressor. As the thermocompressor's displacer piston oscillated (shuttling mass between the expansion and contraction sides of the sealed engine section, thereby inducing pressure oscillations within the engine), air flow commenced from the upstream reservoir, through check valves, and into the downstream reservoir. A ball valve between the reservoirs was used to isolate the reservoirs from each other when closed or reset the circuit for additional experimental trials when opened. Additional ball valves (not shown) regulated the overall air supply into and out of the circuit. When the reservoirs were isolated from each other, the pressure within the downstream reservoir would increase, dependent upon the frequency of the displacer piston's oscillations, the system's initial source pressure, and the temperature of the thermocompressor's expansion side. Meanwhile, air would continually replenish the upstream reservoir from the dry air supply. Modelled flow resistance in the supply line was estimated using the line's length and diameter.

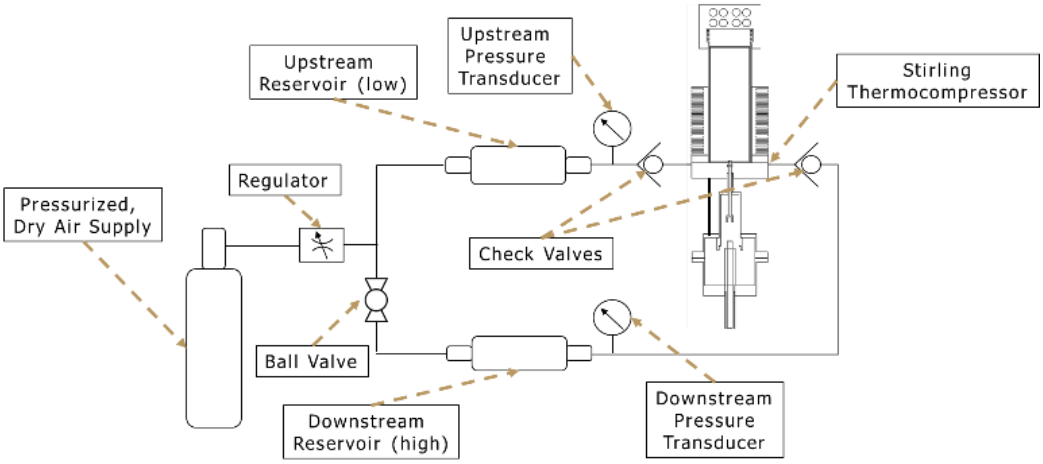

Fig. IV.2: Single-stage thermocompressor experimental setup

Multiple experimental runs were recorded, measuring the single-stage thermocompressor's response to user-defined displacer motion inputs for a given source pressure and temperature difference parameter set. Source pressure was set to approximately 25, 40, and 60 psig while an operating temperature of approximately 330 degrees C was developed at the expansion side of the thermocompressor using the cartridge heaters and a PID controller. On the contraction (cold) side, a 12-watt fan was switched on and off intermittently to keep the cold side's temperature (as measured by the engine's internal thermocouple) stable around 40 degrees C. The displacer was actuated using sinusoidal motion profiles at 1-2 Hz and square-wave motion profiles at 1 Hz. Pressure transducers on the upstream and downstream reservoir tanks recorded the real-time pressure dynamics within the reservoirs, and a thermocouple within the engine section's contraction side recorded in-engine temperature dynamics. The expansion side's temperature was estimated from data from the contraction-side thermocouple together with the model. In post processing, the displacer piston's motion data was also recorded and fed into the mathematical model together with the known starting states of the system. Furthermore, noise from the reservoirs' pressure transducer data was filtered out and a running average was applied to the raw data for presentation. Fig. IV.3 below illustrates a sample experimental run and corresponding model results.

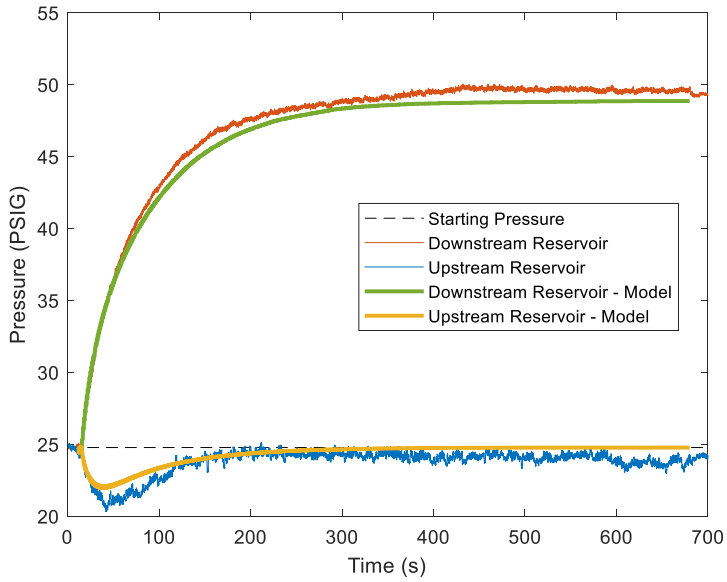

Fig. IV.3: Sample experimental data for a single-stage thermocompressor's response to a 1 Hz sinusoidal displacer motion input, at approximately 25 psig starting pressure and an expansion side temperature of approximately 370 degrees C, shown together with the model's predicted performance, showing a strong correlation between model and experiment.

Fig. IV.3 shows a typical experimental response and modelled response to a 1 Hz sinusoidal displacer motion profile. When the ball valve between the reservoirs is closed, the pressure in the downstream reservoir increases as air moves from source, through the upstream reservoir, through the thermocompressor, and into the downstream reservoir, as managed by the check valves. The pressure in the upstream reservoir initially decreases in response to increased demand for mass flow downstream but later recovers, reverting back to the starting (source) pressure as the overall dynamics approach steady-state performance. The highest power output, as shown by the steepest part of the downstream reservoir dynamics, occurs early, when the downstream reservoir has achieved less than two-thirds of its final, steady-state pressure. At higher downstream pressures, mass flow output from the thermocompressor slows considerably. The model matches the data very well, showing high power output at the beginning of the experimental run and lower power output at the end, and approaching steady-state pressures in-line with the recorded data.

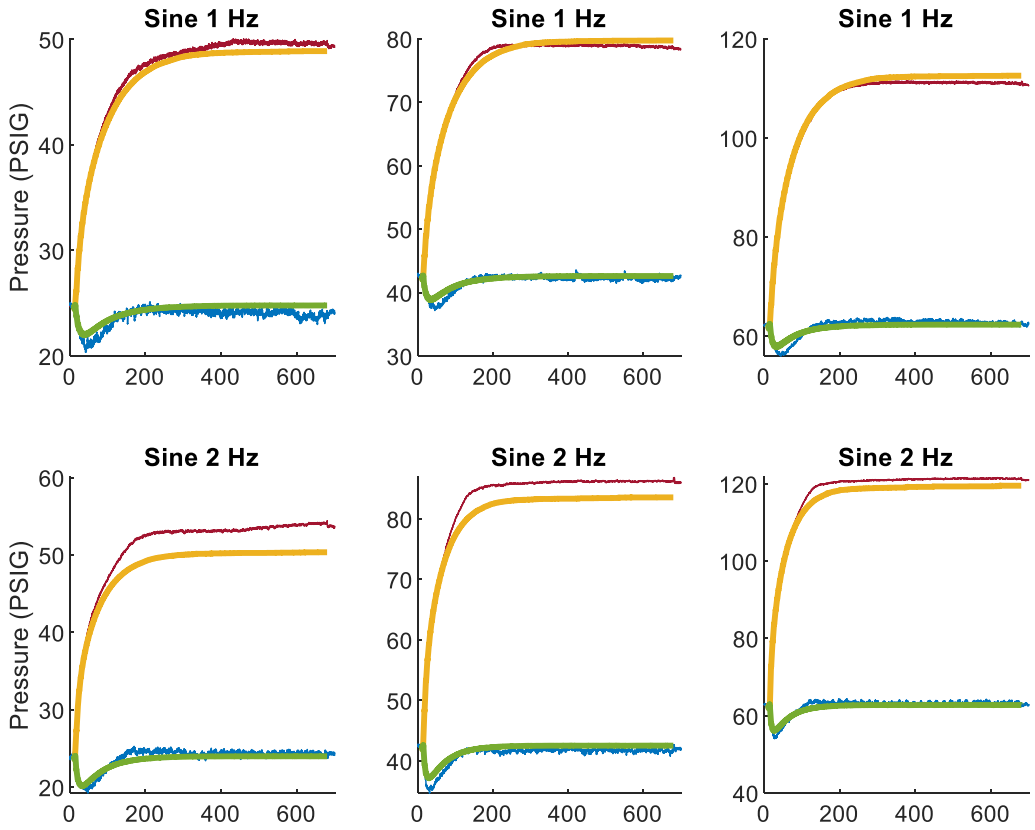

Fig. IV.4: Sample experimental data for a single-stage thermocompressor's response (blue – upstream reservoir; red – downstream reservoir) to a 1 and 2 Hz sinusoidal displacer motion input, at (from left to right) approximately 25, 40, and 60 psig starting pressure and an expansion side temperature of approximately 370 degrees C, shown together with the model's predicted performance (green – modelled upstream reservoir and yellow – modelled downstream reservoir) as functions of time.

Fig. IV.4 shows multiple experimental runs at varying starting pressures, with displacer motion restricted to 1-2 Hz sinusoidal waveforms, together with the model's expected performance. In each case, the model tracks the actual run data well, though the final steady state pressure is overestimated slightly by the model in the case of 2 Hz sine waves at low starting pressures. This is likely due to slight inaccuracies in estimating the amount of dead volume present in the device, which contributes slightly more to 2 Hz sinusoidal motion profiles whose stroke length is slightly attenuated when compared to 1 Hz sinusoidal motion profiles, due solely to the dynamics within the motor's motion controller. When considering all of the experimental data sets, the starting and ending reservoir pressures of each experiment overlap, indicating that a multi-stage thermocompressor is possible at least in the pressure range observed (Fig. IV.6).

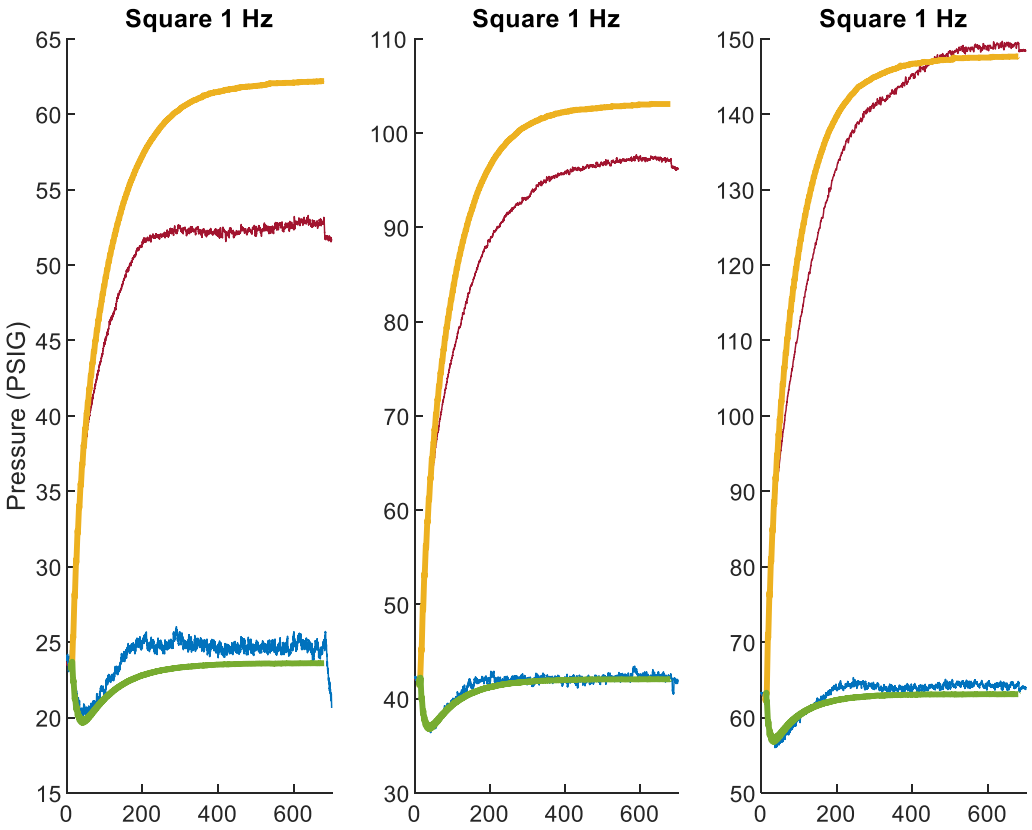

Fig. IV.5: Sample experimental data for a single-stage thermocompressor's response (blue – upstream reservoir; red – downstream reservoir) to a 1 Hz square-wave displacer motion input, at (from left to right) approximately 25, 40, and 60 psig starting pressure and an expansion side temperature of approximately 370 degrees C, shown together with the model's predicted performance (green – modelled upstream reservoir and yellow – modelled downstream reservoir) as functions of time.

The model exhibits more difficulty in representing the performance of low-starting-pressure, square-wave-displacer motion-profile data sets (Fig. IV.5), likely due to the overestimated regenerator's efficiency. The regenerative column connecting the expansion and contraction sides is modelled perfectly, which holds up well with high-performing working fluids (i.e., helium) with high thermal conductivity. Air is less efficient and due to the speed the displacer needs to reach under a square-wave displacer motion command, the regenerator's efficiency is likely overestimated in these cases. The discrepancy is magnified at low starting pressures when the overall mass of the working fluid is less, and thus the working fluid's temperature and pressure are more sensitive to energy inputs (including from the regenerator). A more accurate regenerator efficiency calculation accounting for the speed of the displacer would enhance the model's accuracy.

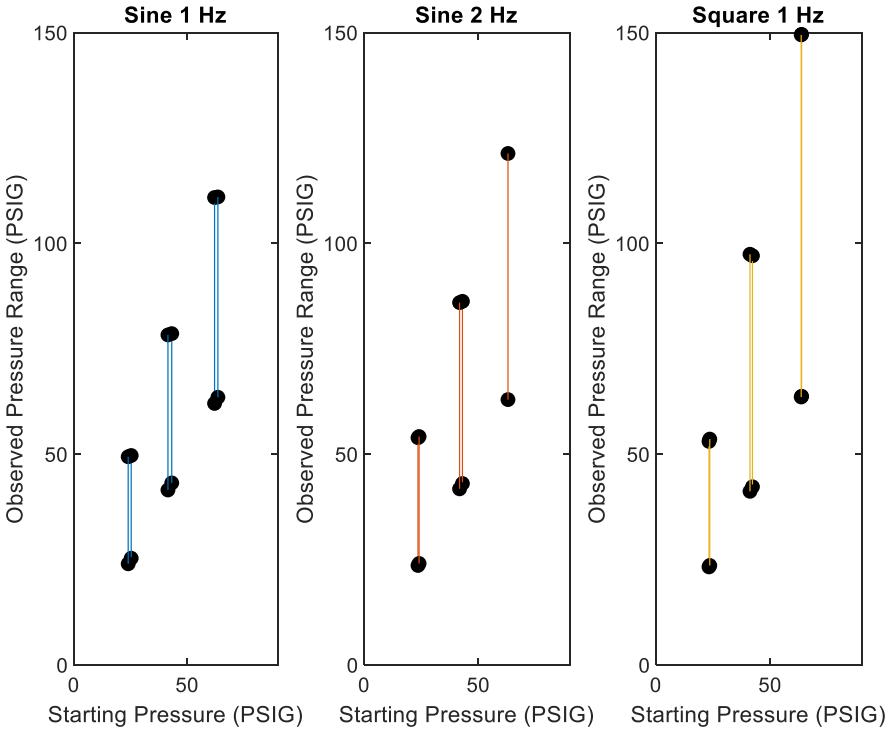

Fig. IV.6: Observed pressure ranges for 17 experimental runs in response to 1-2 Hz sinusoidal displacer motion inputs and a 1 Hz square-wave displacer motion input (6 experimental runs at 1 Hz sine, 5 at 2 Hz sine, and 6 at 1 Hz square) with an expansion side temperature of approximately 370 degrees C and starting pressures from 25-60 psig. For each range, the minimal pressure indicates the supplied source pressure while the maximum pressure indicates the steady-state downstream reservoir pressure, representative of the single-stage thermocompressor's maximum pressure ratio at these operating conditions.

The pressure ratio is defined in this work as the ratio of the pressure immediately downstream from a thermocompressor compared to its starting pressure, and the observed maximum pressure ratios (when mass flow through the thermocompressor has effectively ceased) for the data sets shown in Fig. IV.6 are presented below (Fig. IV.7).

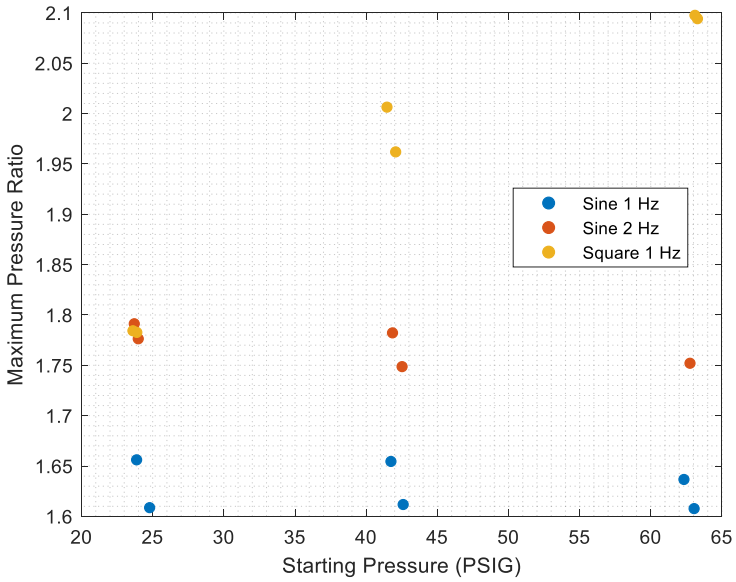

Fig. IV.7: Maximum achieved pressure ratio plot for a single-stage thermocompressor's response to 1-2 Hz sinusoidal displacer motion inputs and a 1 Hz square-wave displacer motion input, and an expansion side temperature of approximately 370 C, with varying starting pressures.

From Fig. IV.7, the maximum pressure ratio is nearly constant for sinusoidal displacer motion data sets, at approximately 1.6-1.65 and 1.75-1.8 for 1 Hz and 2 Hz data sets, respectively, and increases for 1 Hz square-wave displacer motion data sets, from approximately 1.8 at 25 psig starting pressure to 2.1 at approximately 60 psig starting pressure. The square-wave data is consistent with general Stirling engines whose overall output increases with greater starting pressures, though it's possible that with a low-performing working fluid (air), such gains can only be realized at higher minimum displacer speeds; hence, low frequency sinusoidal waves don't experience an overall performance boost as starting pressure increases, as shown. Though the experimental data doesn't extend to lower pressures below 25 psig, if the minimum maximum pressure ratio recorded holds for lower starting pressures then no fewer than five stages would be required to compress air from atmospheric conditions to over 80 psig under these operating conditions. At a maximum pressure ratio however, mass flow under such an arrangement would be limited, as the data in Fig. IV.3 implies.

IV.5 Summary Model

In order to assess the tradeoffs in the design and operation of several thermocompressor acting in concert, the first-principles dynamic model of our prior work needs to be summarized as a time-independent, input-output model. The third-order, first-principles dynamic model [48] is able to predict the performance of a single-stage thermocompressor accurately, but there are drawbacks to applying the model to a multi-stage arrangement (Fig. IV.8 below), especially for preliminary design and feasibility studies. Such studies would require considering multiple arrangements of a multi-stage system of varying parameters: specifically, the number of stages needed to reach a target output pressure and the frequency each stage would need to actuate at in order to deliver a desired mass-flow rate. Even if all thermocompressors of every stage are geometrically identical [49] and held at a uniform temperature difference, each additional stage compounds the field of possible configurations, which can be computationally daunting. Moreover, as the model's various control volumes are dynamically linked, a full multi-stage calculation using the model won't be able to distinguish if one or more stages may be operating sub-optimally.

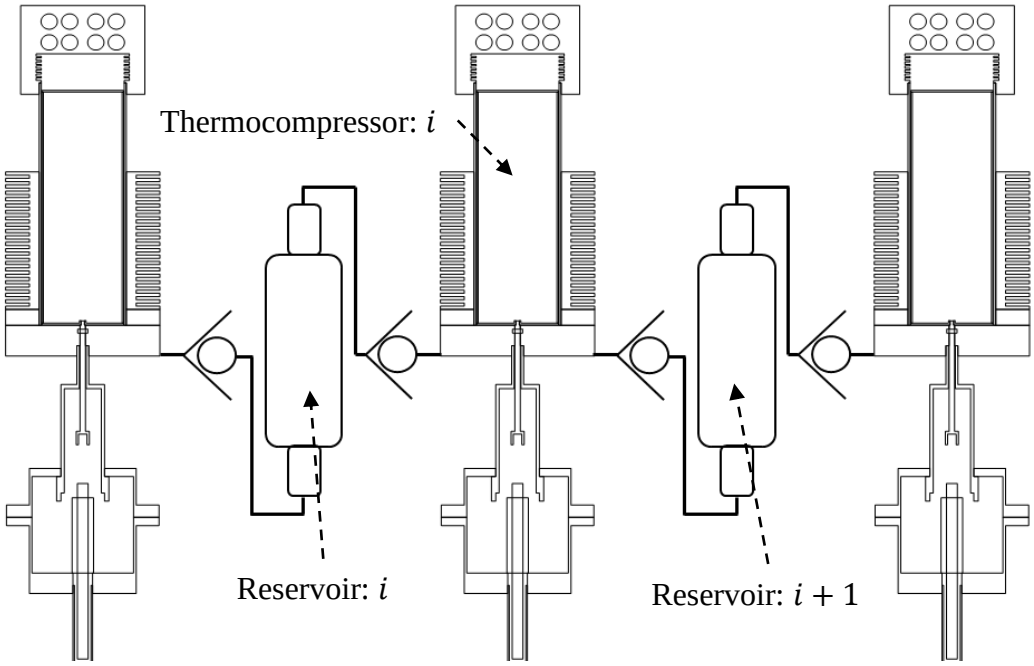

Fig. IV.8: Multi-stage Stirling thermocompressor concept showing multiple thermocompressor units in series with intermediate reservoirs. Upstream reservoirs set the starting pressure for subsequent downstream thermocompressors.

Preliminary design considerations could benefit from a simplified model that relates the output mass-flow, source pressure, expansion-contraction temperature difference, displacer operational frequency, and the pressure ratio (the ratio of subsequent downstream reservoir pressure to source pressure) of a single thermocompressor stage within a multi-stage arrangement. Such a simplified model would quickly consider the effects of altering the inputs of the system (the driving frequency of each particular stage, and the temperature that provides the heat input to the system) on the overall mass-flow rate and the total number of stages necessary to achieve a target pressure, and would also predict the response of the system to changes in mass-flow demand.

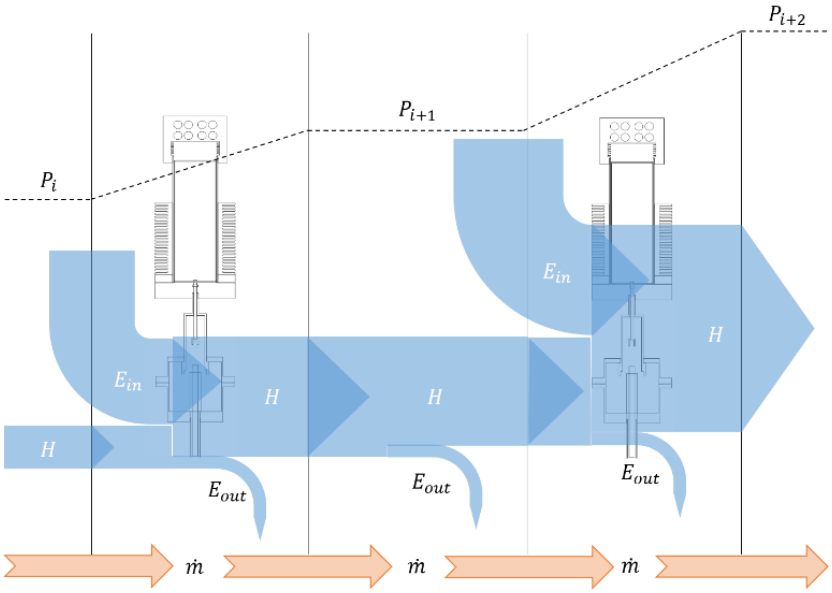

Fig. IV.9: Multi-stage thermocompressor conceptual flow chart illustrating that pressure (P) increases from stage to stage ($i, i+1,\ i+2$) due to influxes of energy (E_{in}) on each thermocompressor's expansion side, which, together with the displacer piston motion, induces enthalpy flow (H). Though energy is gained and lost (E_{out}) through flow resistance and heat transfer, mass flow ($\dot{m}$) remains uniform and conserved.

Several principles guide the development of a simplified model: 1) at steady-state operation, mass flow is uniform and continuous across all thermocompressor stages (Fig. IV.9); 2) as the experimental evidence indicates (Fig. IV.3), there is an inherent tradeoff between high mass flow rates and high pressure ratios such that when the pressure ratio is low (i.e., the subsequent downstream reservoir's pressure isn't much greater than the stage's source pressure) mass flow rates are high, and when the pressure ratio is high (i.e., the subsequent downstream reservoir's pressure significantly exceeds the source pressure), mass flow rates are low; 3) the specifics of the relationship between mass flow and pressure ratio vary depending on operational parameters (the

temperature difference across the thermocompressor, the stage's particular source pressure, and the frequency at which the thermocompressor is actuated); and 4) a stage's subsequent downstream pressure as determined by the pressure ratio becomes the source pressure of the subsequent stage – hence, high pressure ratios necessitate fewer overall stages to achieve a desired final pressure, but come at the cost of low mass-flow output.

In developing a simplified model, the full experimentally-validated, third-order model was simulated for a single stage of the thermocompressor connected between a source and reservoir via modelled check valves (illustrated in Fig. IV.10 below). The model's displacer operational frequency, source pressure, and overall temperature difference were varied in order to determine a relationship between a single stage's mass flow rate and downstream pressure ratio, under the varying operating conditions. The assumptions underlying the field of possible operating conditions (operational frequency, source pressure, and temperature) are as follows: (a) the frequency of the displacer piston can increase to at least 10 Hz while retaining the stroke length, which is presently impossible with the prototype's linear motor though is realistically conceivable with relatively simple changes (replacing the linear motor with a rotary model and slider-crank mechanism, for example); (b) the expansion side temperature can increase to at least 650 degrees C, the high end of the "mid-grade" temperature range for industrial waste heat [1] and approaching the temperature limit of our aluminum cooling fins; (c) the contraction side's temperature can be kept relatively constant, near 80 degrees C, consistent with observations from the prototype (Fig. IV.7); and (d), the existing prototype geometry is retained though the simulated tubing lines between the source, thermocompressor, and reservoir were shortened for simplicity.

From these assumptions, single-stage simulations were conducted for combinations of different operating conditions: varying source pressures from 0 to 80 psig, at 10 psi increments; varying expansion side temperatures from 350 degrees C (consistent with our experiments) to 650 degrees C, at 100-degree increments; and varying sinusoidal displacer frequencies from 1 Hz to 10 Hz, at 1 Hz increments.

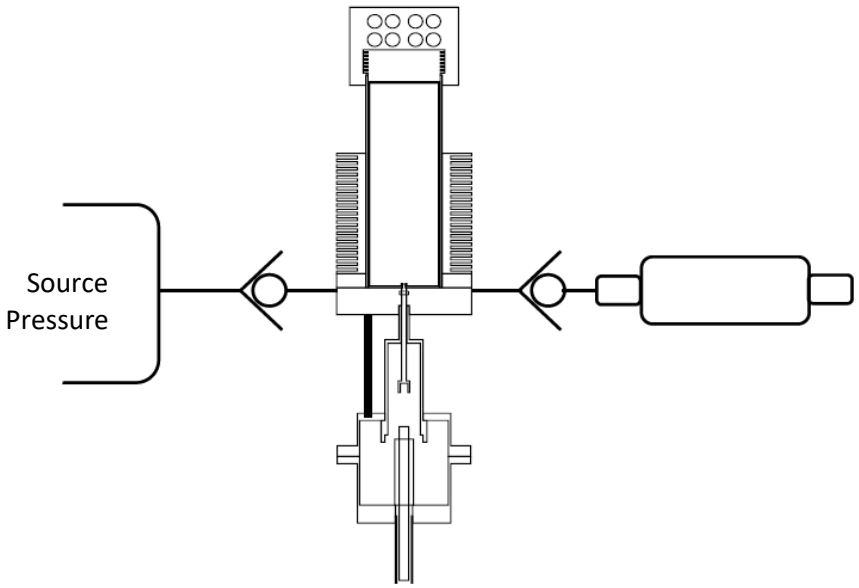

Fig. IV.10: Single-stage simulation diagram showing a source held at constant pressure, a single thermocompressor whose input and output are managed by check valves, and a subsequent (closed) downstream reservoir.

IV.5.1 Relationship Between Mass Flow and Downstream Pressure Ratio

Fig. IV.11 shows the mass flow and the downstream pressure ratio as functions of time for a typical single-stage simulation. As pressure builds within the downstream reservoir, mass flow from the thermocompressor to the reservoir is simultaneously restricted. With the independent time variable subsumed, Fig. IV.12 shows that the relationship between mass flow and the pressure ratio is highly linear: any increase in subsequent-stage pressure corresponds to a near-uniform decrease in the output mass flow rate. At different simulated expansion-side temperatures, source pressures, and displacer frequencies, the slope and y-intercept of the pressure-ratio-mass-flow curve are different but the mostly-linear character of the correlation remains. Therefore, the third-order modelled relationship between mass-flow and downstream pressure ratio can be simplified to a linear estimation:

$$\dot{m} = c_1 PR + c_2 \tag{1}$$

where $\dot{m}$ is the output mass flow (kg/s), PR is the pressure ratio, and c_1 and c_2 are parameters that are functions other operational inputs: source pressure, expansion-side temperature, and the displacer piston's operational frequency. Though the source pressure and expansion-side

temperature of a particular in-series thermocompressor stage aren't usually directly controllable (dependent upon the quality of the external heat source or the dynamics of other upstream thermocompressors), the stage's displacer operating frequency is controllable and affects the overall performance of the multi-stage device. It is therefore necessary to model the c_1 and c_2 parameters as explicit functions of operational frequency.

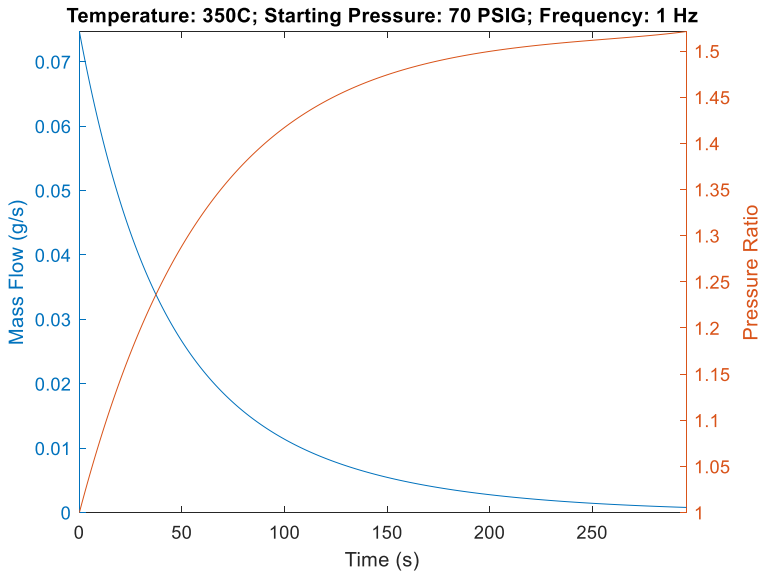

Fig. IV.11: Mass flow rate and downstream pressure ratio as functions of time for a representative sample simulation.

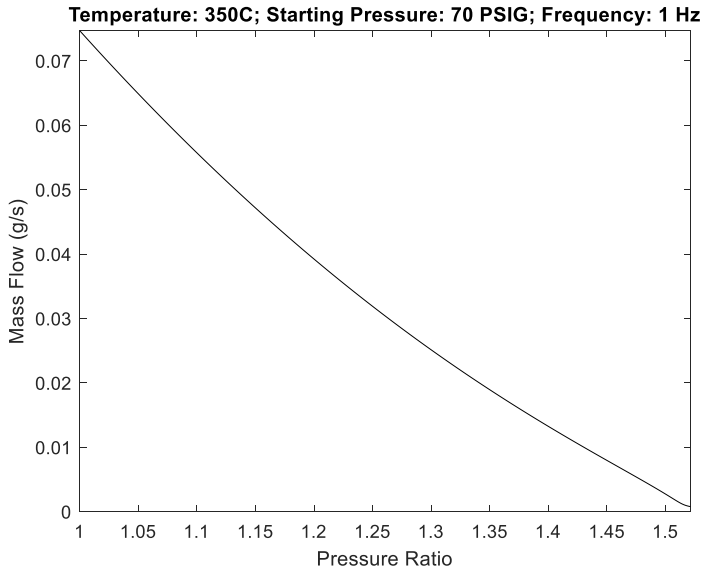

Fig. IV.12: Mass flow rate as a function of the downstream pressure for a representative sample simulation.

Fig. IV.13 illustrates how the c_1 and c_2 parameters (as estimated from the third-order model's simulations) change with increasing operational frequency for a selected simulation set in which the other operational inputs (source pressure and expansion-side temperature) are held constant. As illustrated, the parameters exhibit a highly linear correlation for the range of frequencies considered. This linear correlation persists across simulations sets at different source pressures and expansion side temperatures, so Equation 1 can be re-written with operational frequency as an independent input.

$$\dot{m} = (\alpha_1 F + \alpha_2)PR + (\alpha_3 F + \alpha_4) \tag{2}$$

where $\dot{m}$ is the output mass flow (in kg/s), PR is the pressure ratio, and F is the displacer piston's operational frequency (in Hz). The remaining parameters α_{1-4} are functions of the remaining operational inputs (source pressure and expansion-side temperature), though an additional linear estimate or otherwise simple mathematical relationship was not found to accurately predict their values. Therefore, the values for those parameters are produced from an interpolated two-dimensional lookup table composed of data produced by the full model over the field of simulations. The values for the interpolated look up table for parameters α_{1-4} can be found in Appendix A. A sample of the summary model's estimation of the full, third-order model's simulation is shown in Fig. IV.14 below.

Due to the linear nature of the terms, Equation 2 can be easily rearranged to solve for a stage's operational frequency or the pressure ratio, given a known mass flow. At zero mass-flow, the maximum compression ratio for a known starting pressure, expansion-side temperature, and displacer frequency can be computed:

$$PR_{max} = -(\alpha_3 F + \alpha_4)/(\alpha_1 F + \alpha_2) \tag{3}$$

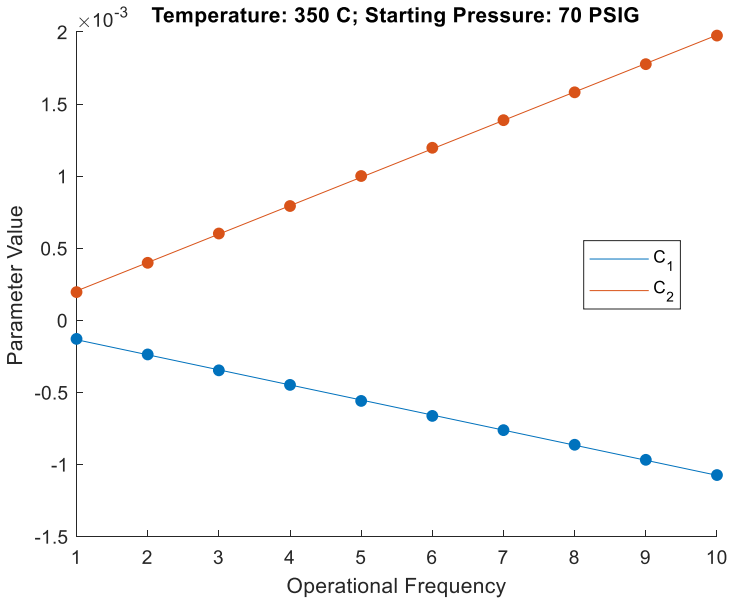

Fig. IV.13: Equation 1 parameters as functions of operational frequency, with linear trend-line estimates, for a sample simulation set.

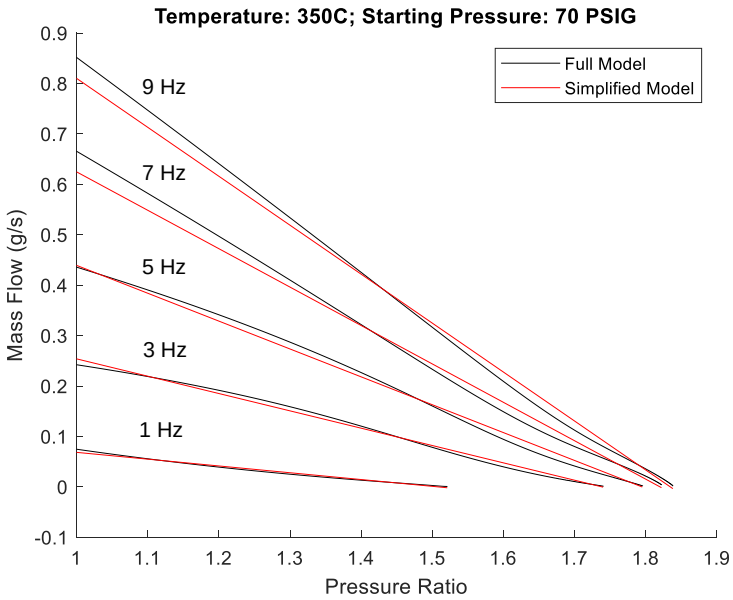

Fig. IV.14: Sample comparison between the full and simplified models with regards to changing frequency for a fixed pressure and expansion-side temperature simulation set. At increasing frequencies, the maximum compression ratio and maximum mass flow rate increase.

The applicability of Equation 2 is limited to scenarios whose operational parameters fall within the source pressure, expansion-side temperature, and displacer operational frequency bounds specified above, and scenarios that retain the same geometry and contraction-side temperature as outlined in the simplified model's guiding principles. The simplified model's goodness-of-fit was

compared to the full, third-order modelled mass-flow vs. pressure-ratio simulations (Fig. IV.15) and the full and simplified models show a high degree of agreement.

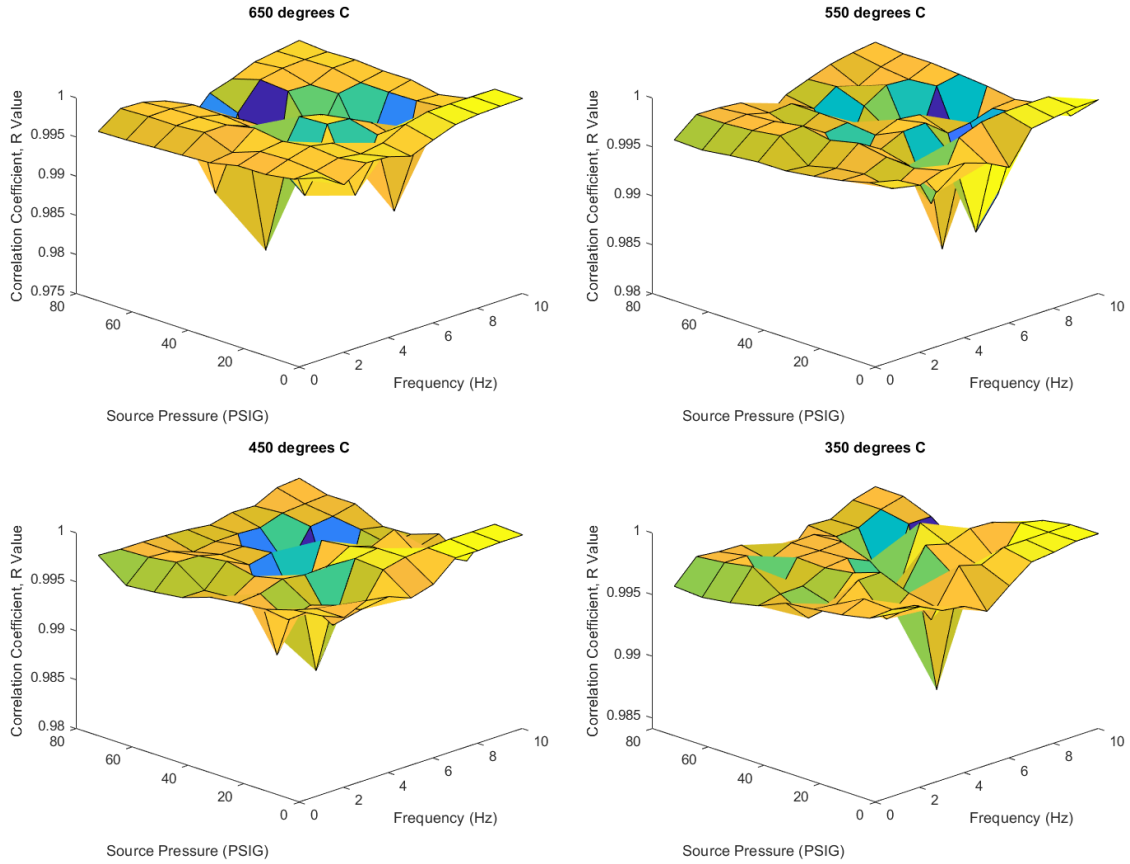

Fig. IV.15: Goodness-of-fit estimation of the mass flow vs. pressure ratio relationship between the full, third-order model and simplified model using the Pearson correlation coefficient, R, for various expansion-side temperature data sets comprised of varying source pressures and displacer operational frequencies

IV.5.2 Relationship Between Displacer Power and Downstream Pressure Ratio

The power necessary to move the displacer piston was derived from the third-order model which calculated the forces applied to the displacer piston while following a sinusoidal trajectory at a given operational frequency. From observations over the full field of the third-order model's results, the relationship between required displacer motor power and the pressure ratio can be approximated as a 3-degree polynomial (Eqn. 4 and Fig. IV.16):

$$W_{displacer} = \beta_1 PR^3 + \beta_2 PR^2 + \beta_3 PR + \beta_4 \quad (4)$$

where $W_{displacer}$ is the power required (in Watts) to move the displacer piston along a sinusoidal motion path of tunable frequency, and PR is the pressure ratio. The values for the parameters β_{1-4} depend on the operational inputs but unlike the case in Fig. IV.13, no simple mathematical relationship relating the displacer operational frequency, source pressure, or the expansion-side temperature to the required displacer motor power was found to sufficiently predict the values of the coefficients of the 3-degree polynomial. As before, the values for those parameters are therefore produced from an interpolated three-dimensional lookup table composed of data produced by the full model over the field of simulations. The values for the interpolated look up table for parameters β_{1-4} can be found in Appendix B. Similar to Fig. IV.15, the simplified model's predictions for the required displacer motor power under a range of operating conditions matches the full model's results well (Fig. IV.17), so the simple model can be used to estimate the total power consumed by a multi-stage device operating within the operational bounds as specified.

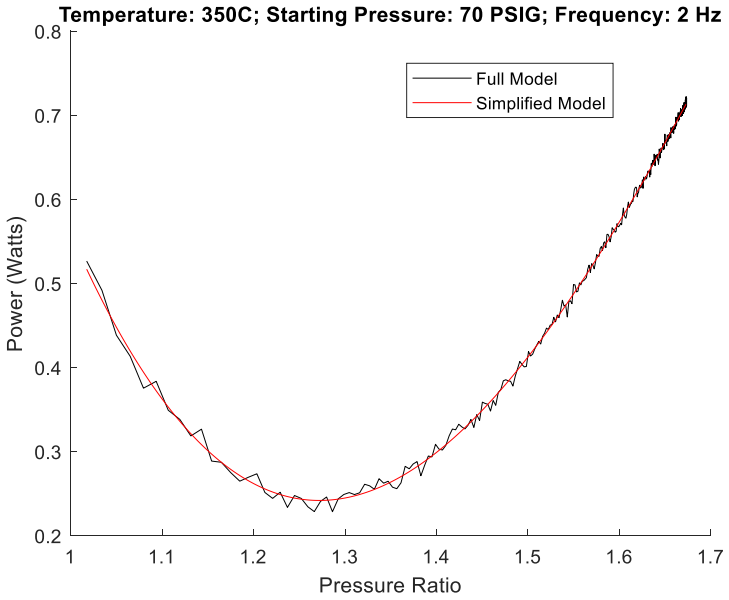

Fig. IV.16: Full, third-order model and simplified model approximation of the relationship between the power required to move the displacer piston (the displacer motor power) and the pressure ratio for a sample data set.

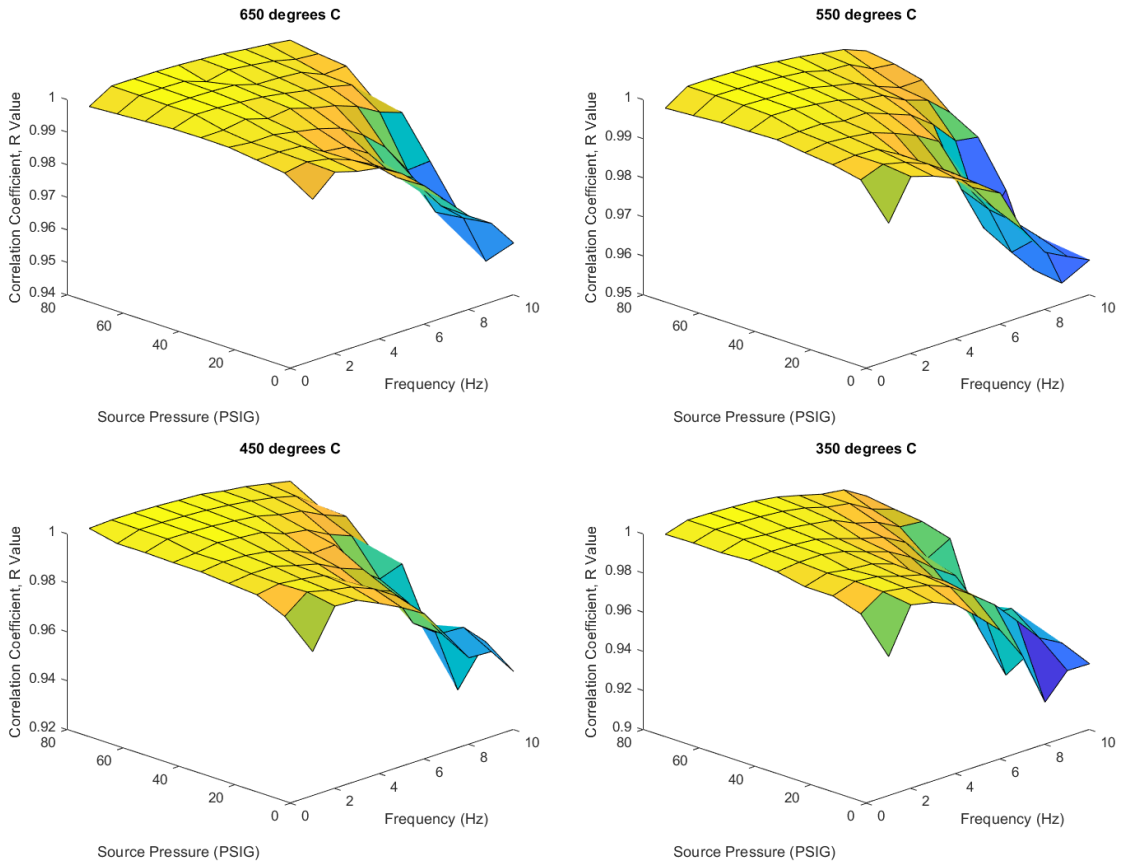

Fig. IV.17: Goodness-of-fit estimation of the displacer power vs. pressure ratio relationship between the full, third-order model and simplified model using the Pearson correlation coefficient, R, for various expansion-side temperature data sets of varying source pressures and displacer operational frequencies.

IV.6 Feasibility Study

Having demonstrated that the simplified model is an adequate estimation for the more-accurate, but limited third-order model for the purposes of studying the relationships between inputs and outputs, the simplified model can now be used to project the feasibility of a multi-stage system based on the existing geometry of the single-stage experimental prototype, in order to determine such a multi-stage system's requisite number of stages, the size of each stage (i.e., the number of parallel thermocompressor units within a stage, fixed in size in order to avoid introducing differences known to be present in the scaling of a Stirling device), and the frequency at which to run those stages given a desired mass flow, inlet and outlet pressure of the entire thermocompressor chain, and temperature of waste heat provided. A multi-stage Stirling thermocompressor's feasibility is validated, in this context, by its ability to utilize mid-grade waste

heat sources [1] to intake air at atmospheric conditions and raise its pressure to nominal industry standards (at least 80 psig cut-in pressure) using a reasonable number of stages and parallel units, and to output air at mass-flow levels comparable to existing air-compressors within motor-energy requirements that meet or exceed those of extant devices.

The feasibility study is conducted algorithmically: for a given set of specified parameters, including operating conditions (the source pressure and expansion side temperature), performance targets (the desired final pressure and output mass flow rate), operation limits (the maximum displacer frequency), and tunable variables (the target stage pressure ratio), Equations 2-4 are used to determine (1) the total number of in-series stages required to achieve the desired final pressure, (2) the number of units needed in parallel for each stage, (3) the operating frequency of each stage, and (4) the total motor energy required to achieve the performance targets, computed for each stage and in aggregate. Further analysis can optimize the algorithm's results in terms of the minimum number of stages or total units required, or the minimum motor power required for a "best-case" comparison against extant air compressor systems.

IV.6.1 Algorithm Parameters

The specifics of the feasibility algorithm are presented in the flowchart in Fig. IV.18. The algorithm was executed under variable operating conditions: the expansion side temperature varied from 350-650 degrees C (within the "mid-grade" temperature range for industrial waste heat [1]), in 100-degree-C increments. The source and target pressures remained constant (0 and 80 psig, respectively). And the displacer piston's theoretical operational frequency was capped at 10 Hz. Equation 2 was rearranged to solve for the operational frequency of a particular thermocompressor stage, and Equation 3 was used to solve for the maximum pressure ratio given a mass-flow rate of zero, the maximum potential operational frequency, the known expansion-side temperature and the known stage-specific source pressure.

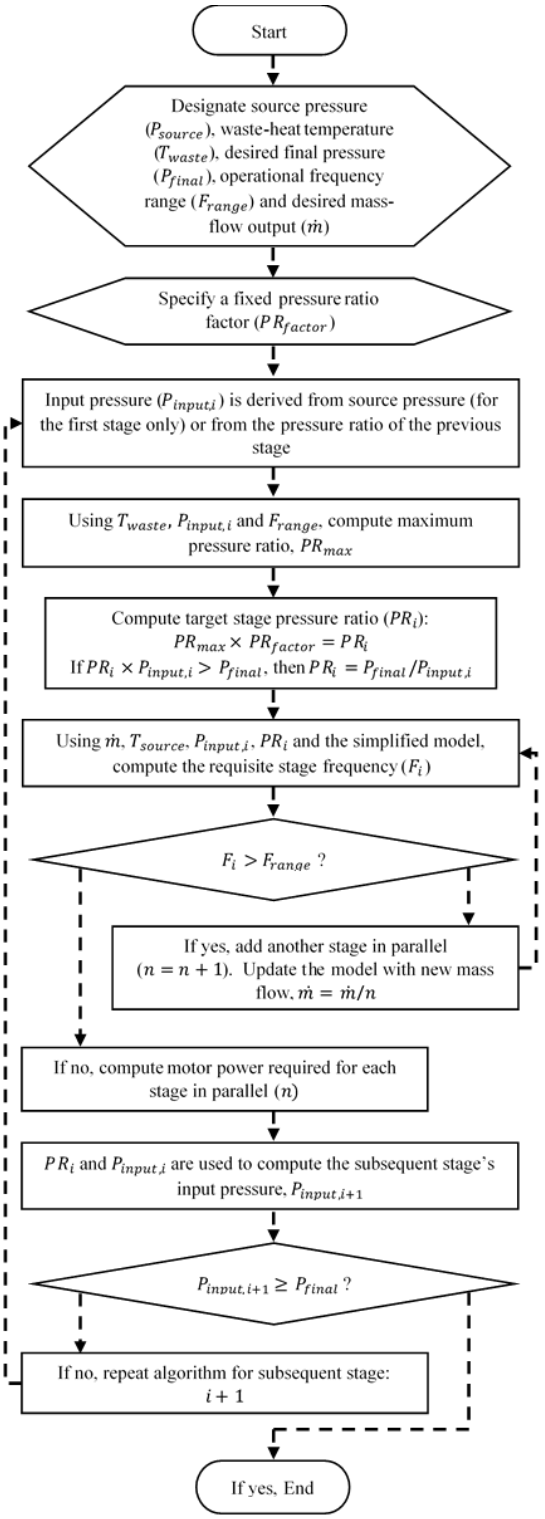

Fig. IV.18: Flow-chart for multi-stage thermocompressor analysis. For the specified operating conditions, operational limits, and performance targets, and using a desired pressure ratio factor (a percentage of a stage's maximum theoretical pressure ratio), the algorithm (1) computes the target pressure ratio for each stage, (2) computes the necessary displacer frequency required to sustain the target mass-flow rate given the target pressure ratio, (3) adds units in parallel should the

required frequency of a stage exceed operational limits, (4) computes the overall displacer piston power thus far required, and (5) repeats the process with a new inlet pressure specified by the previous' stage's inlet pressure and computed pressure ratio.

When Equation 2 was used to solve for a stage's particular operating frequency, it was necessary to provide a user-designated, target stage pressure ratio in order to solve the equation. A fixed "pressure ratio factor" was employed to automatically designate appropriate stage-specific pressure ratios for every stage. The pressure ratio factor is a constant percentage of the stage-specific maximum pressure ratio, which produces a variable target stage pressure ratio because a stage's maximum pressure ratio is dependent upon the aforementioned operating conditions. The pressure ratio factor varied from 1-99%, at 1% increments and yielded a multitude of plausible multi-stage thermocompressor configurations, which could be filtered down further to meet other criteria, such as minimum motor power required (computed using Equation 3) or minimum number of stages required.

The target mass-flow rates for the algorithm were derived from data produced by the Compressed Air and Gas Institute (CAGI) which publishes guidelines for pneumatic system designers when selecting an appropriate air compressor for an application. The data published by CAGI provides, among other tools, a back-of-the-envelope estimate for the amount of horsepower required to sustain peak and continuous flow demands at a given compressor's cut-in and cut-out pressure. For the 80-100 psig cut-in, cut-out pressure range, continuous mass-flow demands between 0 and 100 cubic feet per minute of air at 1 bar and 20 degrees C (0% relative humidity) were characteristic of compressors requiring motor power between 0.5 and 25 horsepower [65]. Consequently, the algorithm's desired output flow rate ranged from 0 to 100 g/s. The data presented in Figs. IV.19-IV.25 below show the results of the feasibility study and have been selected to reflect operating conditions whereby total required motor power required is minimized.

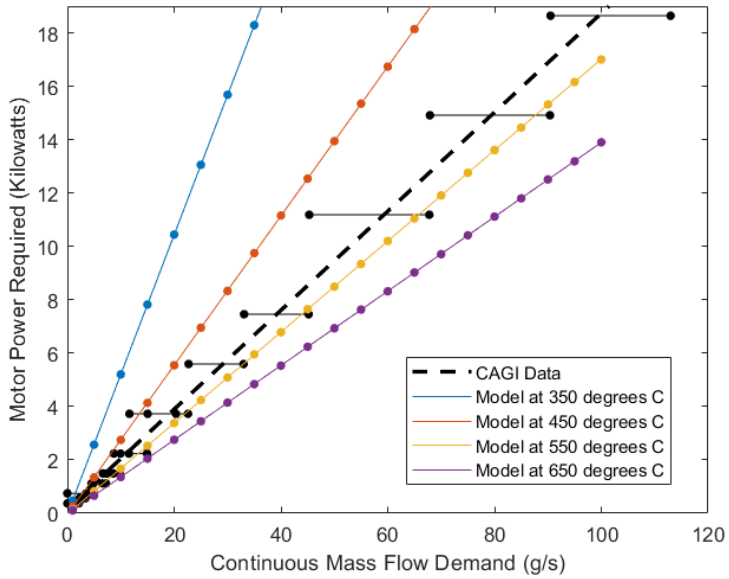

Fig. IV.19: Motor power required of multi-stage thermocompressor arrangements produced by the algorithm compared to the estimated motor power required of extant traditional air compressors of varying mass-flow demands. Estimated extant air compressor performance is derived from data published by CAGI (shown above, in black), with a superimposed trend line based on the estimated data. The modelled data presented represent arrangements requiring the least amount of motor power, given the algorithm's additional noted parameters including varying expansion-side temperature (as indicated).

Fig. IV.19 shows the estimated motor power required to produce compressed air at various continual mass flow demands for extant air compressors and for theoretical Stirling thermocompressor arrangements algorithmically-designed under varying input parameters, most notably expansion-side temperature and target stage pressure ratio. According to the algorithm, a multi-stage thermocompressor system comprised of series and parallel units similar to the prototype's geometry is likely to consume more motor energy than extant air compressors at lower expansion-side temperatures. At higher expansion-side temperatures, the motor power demand is reduced and is projected to be lower than traditional compressors, representing a net energy savings. The algorithm's results are consistent with general Stirling engines whose power output and efficiency increase with higher expansion-side temperatures The boundary expansion-side temperature is approximately 525 degrees C according to this study – multi-stage systems operating at temperatures below this threshold aren't likely to outperform traditional compressors in terms of necessary motor energy investment, though other advantages including the potential for low-noise, may be desirable. At low continuous mass flow demands, some lower expansion-

side temperature multi-stage arrangements may become more feasible. Motor power demand could also be reduced by using a lighter displacer piston (see Table IV.1).

The multi-stage algorithm results shown in Fig. IV.19 were evaluated at different user-defined pressure ratio factors, and plausible multi-stage thermocompressor arrangements optimized for minimal motor power required are shown. Fig. IV.20 below presents the optimal stage pressure ratio factors resulting in minimal motor power required for a specified continuous mass-flow demand at varying expansion-side temperatures. Generally speaking, employing higher user-specified pressure ratios would require fewer stages to achieve the minimum cut-in pressure, but would also sustain less overall mass flow. Lower pressure ratios can handle the power demand better, but require more stages to meet a target pressure. As the figure illustrates, for much of the mass-flow demand range under examination, the optimal stage pressure ratio factors closely adhere to specific values based on the selected expansion-side-temperature, though some variability is present at low mass-flow demand.

As Fig. IV.21 shows, the total number of stages required to achieve at least 80 psig cut-in pressure decreases as temperature increases, and the number of stages required is generally consistent across all mass-flow demand ranges. Stirling devices in general improve in efficiency and power output as the temperature difference between the expansion and contraction sides increases; similarly, the maximum pressure ratio increases with increased temperature for thermocompressors. At similar pressure ratio factors (Fig. IV.20) higher maximum pressure ratios result in fewer required stages. The feasibility study found that roughly 9, 7, 6, and 5 stages are required for multistage arrangements operating under expansion side temperatures of 350, 450, 550, and 650 degrees C, respectively, optimized for minimum requisite displacer motor power.

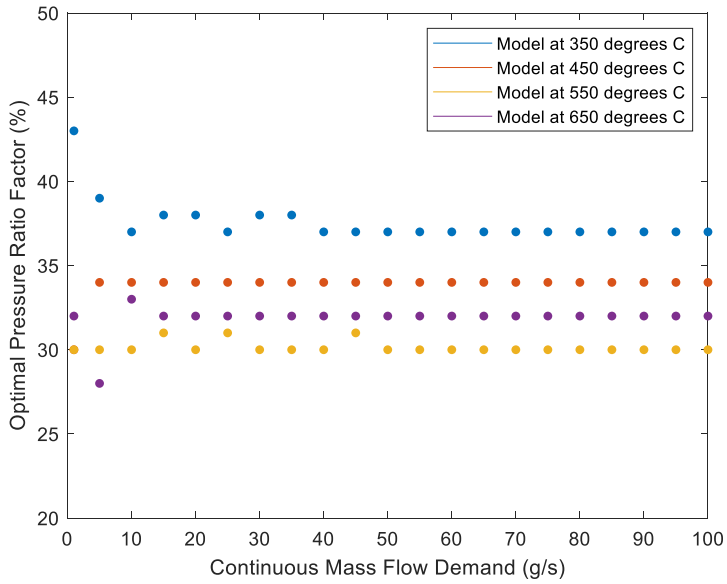

Fig. IV.20: Optimal stage pressure ratio factors of the algorithm's results displayed in Fig. IV.19. Optimal stage pressure ratio factors for expansion side temperatures of 350, 450, 550, and 650 degrees C approached defined limits of 37%, 34%, 30%, and 32%, respectively, for much of the continuous mass-flow demand range under examination, especially at higher flow demands.

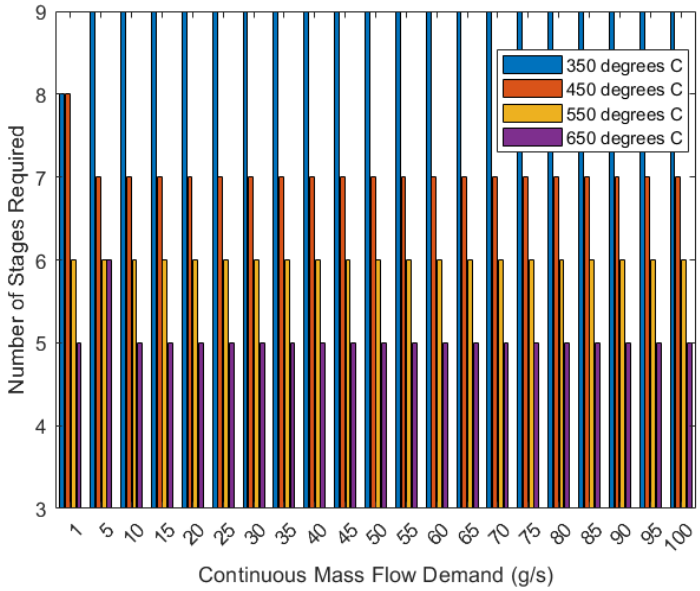

Fig. IV.21: Total number of stages required to achieve 80 psig for multi-stage thermocompressor arrangements given the algorithm's additional noted parameters including varying expansion-side temperature (as indicated), optimized for least motor power required for varying continuous mass-flow demands.

For each stage of the multistage device, multiple parallel thermocompressor units would be required if the mass-flow demand exceeds the output capacity of an individual thermocompressor within the given operational parameters, most notably the maximum displacer-piston frequency. In such a scenario, the algorithm adds more units in parallel to distribute the mass-flow demand until the identical performance of each unit is within operational constraints. This increase in the total number of required thermocompressor units highlights the essential tradeoff between employing thermocompressors or traditional air compressors – greater potential energy efficiency but a larger device footprint.

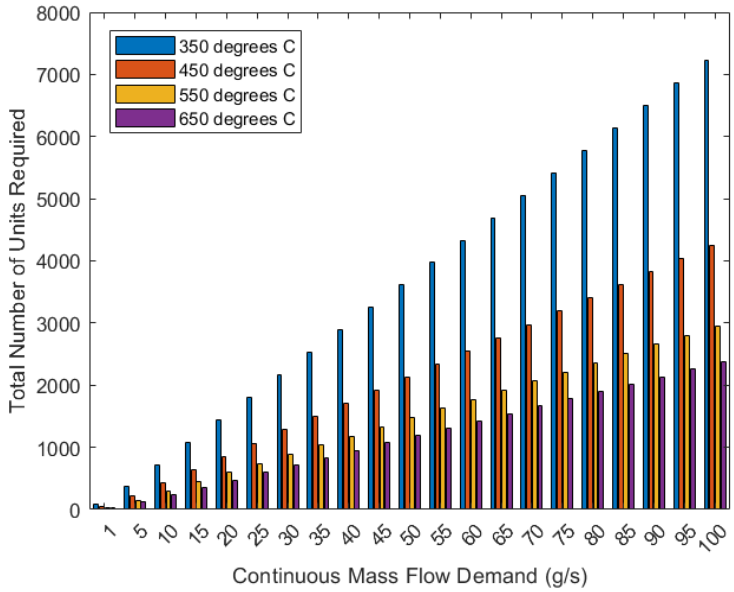

Fig. IV.22: Total number of thermocompressor units required to achieve 80 psig for multi-stage thermocompressor arrangements, optimized for least motor power required using the algorithm and parameters specified including varying expansion-side temperature (as indicated), for a range of continuous mass-flow demands.

Fig. IV.22 shows the total number of thermocompressor units required according to the multi-stage algorithm for the mass flow demand range specified, for different expansion-side temperatures. Not only are more stages required for lower-expansion-side-temperature arrangements (Fig. IV.21), but the total number of units in parallel or in series is also greater, consistent with the general premise that Stirling device performance increases at greater temperature differentials. Consequently, the total number of thermocompressor units may exceed allowable space or cost; at lower mass flow demands and higher expansion-side temperatures,

however, the total number of units required may be more feasible (Fig. IV.23). Using thermocompressor stages of varying geometry would also potentially lower the device's footprint.

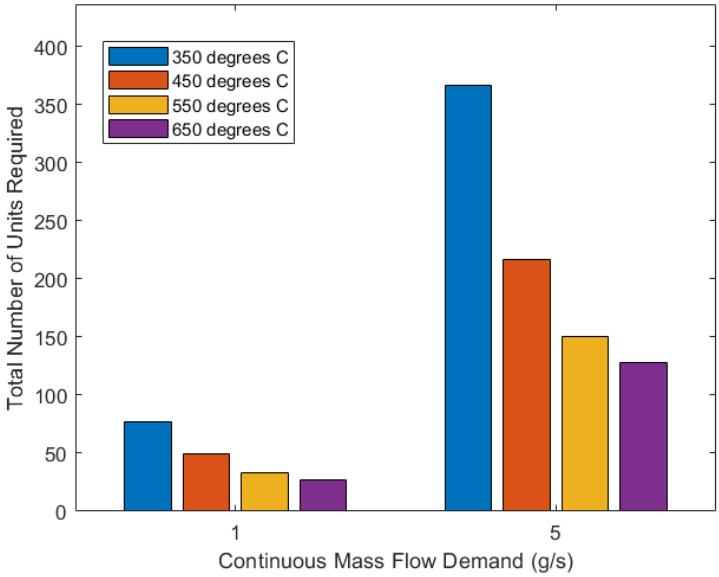

Fig. IV.23: Total number of thermocompressor units required to achieve 80 psig for multi-stage thermocompressor arrangements, optimized for least motor power required using the algorithm and parameters specified including varying expansion-side temperature (as indicated), for a selected, minimal range of continuous mass-flow demands.

While Fig. IV.22 provides a sum total of all units, parallel and in-series, required to meet continuous mass-flow demand and target minimum cut-in pressure, Fig. IV.24 shows a sample of how many units would be required in parallel for each stage in a selected arrangement. The general trend is that fewer units per stage are required at later stages of compression, consistent with general Stirling device performance whose power output increases at greater source pressures. Greater power output in thermocompressors means that fewer devices in parallel are necessary to manage the output flow demand. For the feasibility study, it's noted that even at the highest expansion-side temperature and the least mass-flow demand considered, no stage requires fewer than two units in parallel.

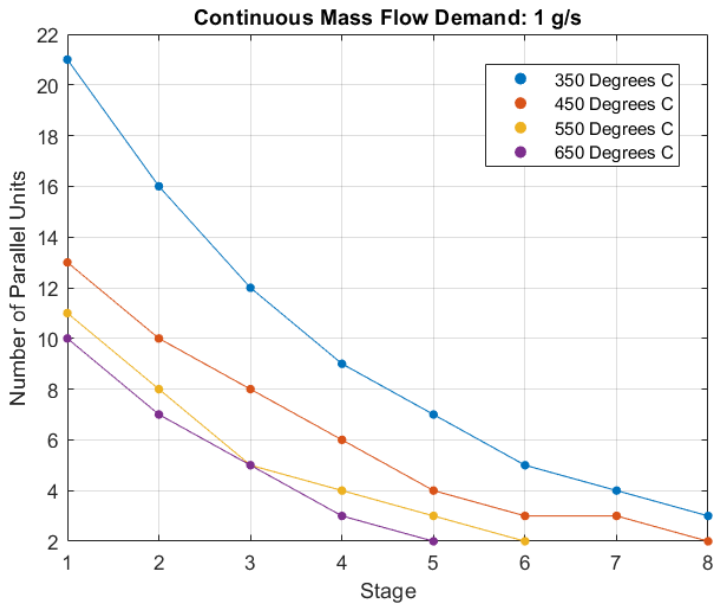

Fig. IV.24: Number of units in parallel for each stage of multi-stage thermocompressor arrangements of a selected mass-flow demand.

The algorithm is capable of computing not only the overall number of stages, units, and optimized maximum pressure ratio factor for a multi-stage arrangement, but also the specific operating frequency of the units at each stage. The operational frequency of each stage in a sample set of arrangements is illustrated in Fig. IV.25. As the figure shows, downstream stages required generally lower operating frequencies than upstream ones, owing to their overall greater efficiencies and power outputs associated with higher source pressures.

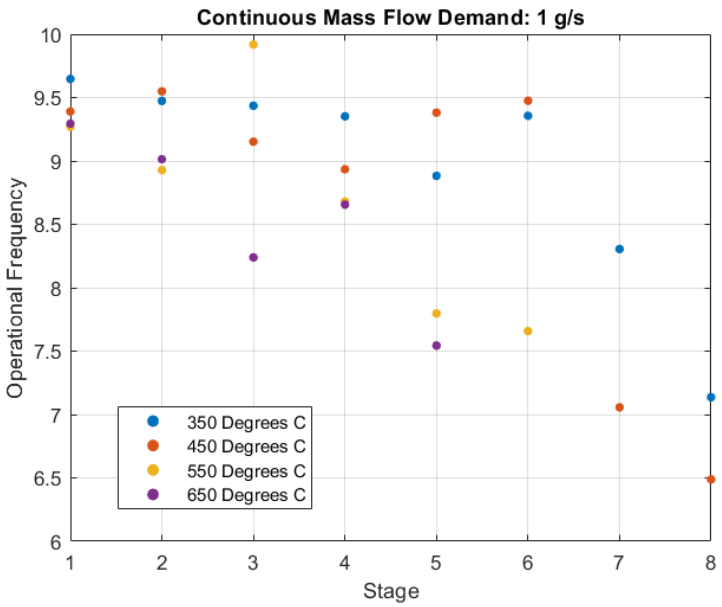

Fig. IV.25: Operational frequency of each stage of multi-stage thermocompressor arrangements for a selected mass-flow demand.

IV.7 Conclusions

The single-stage thermocompressor has been experimentally characterized using air and has demonstrated its ability to compress air from 25 psig to over 80 psig under 1-2 Hz sinusoidal and 1 Hz square-wave displacer motion profiles and 370 degrees C expansion side temperature. Under those operating conditions, the measured maximum pressure ratio varied between 1.6 and 2.1. The adapted third-order model was shown to closely predict these results. The third-order model was also simplified to provide an efficient way of evaluating the feasibility of a proposed multi-stage thermocompressor and to predict its performance when compared to extant, off-the-market traditional air compressors. The resulting algorithm predicts that moderate displacer power requirements and a reasonably low number of requisite parallel and in-series thermocompressor units in arrangements utilizing high expansion-side temperatures could make multi-stage Stirling thermoocmpressor's a viable alternative to traditional compressors. The outlook for adopting thermocompressors in industrial settings could benefit from greater geometric design flexibility, use of a lighter displacer piston in the current platform, and/or employing a higher range of temperature differences across the device.

Chapter V

Conclusion

This dissertation has provided a simple, first-principles-based model for predicting the performance of a Stirling thermocompressor, and validated that model under a variety of different experiments, utilizing different working fluids, expansion-side temperatures, starting pressures, in-series orifice restrictions, and displacer motion profiles. The model was consistently shown to accurately track the prototype's dynamics with little tuning required. Future work remains to validate the model at higher operating frequencies, particularly the regenerative channel's heat transfer estimation. Greater model clarity could also be achieved by means of a more accurate way of recording the temperature within the expansion side of the engine.

This work has also demonstrated that that controlled displacer piston concept offers a clear performance advantage for Stirling thermocompressors or other Stirling arrangements which operate at low frequency or have necessary dead volume. Though our device's linear motor could easily produce customized displacer motion paths, its speed limitations restricted the scope of our analysis, and it's left up to future designers to increase overall displacer frequency.

Finally, the multi-stage thermocompressor concept has been shown to be plausible given the prototype's geometry. At high expansion-side temperatures and high displacer frequencies, the model predicts that overall energy savings in pneumatics production could result if such a multi-stage device utilizing waste heat were adopted in certain industrial settings.

Appendix A

Look-up Tables for Summary Model Parameters for Chapter IV, Equation 2

α_1	Pressure (psig)								
Temperature (C)	**0**	**10**	**20**	**30**	**40**	**50**	**60**	**70**	**80**
350	-1.804E-05	-3.230E-05	-4.597E-05	-5.856E-05	-6.858E-05	-7.747E-05	-9.048E-05	-1.045E-04	-1.169E-04
450	-1.581E-05	-2.841E-05	-3.578E-05	-4.890E-05	-5.584E-05	-6.453E-05	-7.628E-05	-8.773E-05	-9.848E-05
550	-1.407E-05	-2.384E-05	-3.219E-05	-4.026E-05	-4.589E-05	-5.684E-05	-6.640E-05	-7.526E-05	-8.419E-05
650	-1.272E-05	-2.331E-05	-2.884E-05	-3.451E-05	-4.101E-05	-5.006E-05	-5.853E-05	-6.544E-05	-7.383E-05

α_2	Pressure (psig)								
Temperature (C)	**0**	**10**	**20**	**30**	**40**	**50**	**60**	**70**	**80**
350	-2.843E-06	-3.112E-06	-4.413E-06	-1.487E-05	-2.583E-05	-3.530E-05	-3.607E-05	-3.027E-05	-3.207E-05
450	-2.650E-06	-2.451E-06	-1.843E-05	-1.709E-05	-3.604E-05	-3.205E-05	-2.878E-05	-3.029E-05	-3.280E-05
550	-2.308E-06	-7.513E-06	-1.708E-05	-2.070E-05	-3.618E-05	-2.484E-05	-2.619E-05	-3.187E-05	-3.460E-05
650	-2.095E-06	-6.185E-07	-1.772E-05	-2.621E-05	-3.040E-05	-2.295E-05	-3.324E-05	-4.236E-05	-3.332E-05

α_3	Pressure (psig)								
Temperature (C)	**0**	**10**	**20**	**30**	**40**	**50**	**60**	**70**	**80**
350	2.703E-05	5.137E-05	7.604E-05	1.002E-04	1.259E-04	1.467E-04	1.718E-04	1.972E-04	2.214E-04
450	2.782E-05	5.205E-05	7.741E-05	1.016E-04	1.257E-04	1.459E-04	1.713E-04	1.972E-04	2.212E-04
550	2.836E-05	5.291E-05	7.725E-05	1.017E-04	1.231E-04	1.481E-04	1.732E-04	1.969E-04	2.211E-04
650	2.878E-05	5.317E-05	7.810E-05	1.010E-04	1.247E-04	1.488E-04	1.729E-04	1.971E-04	2.209E-04

α_4	Pressure (psig)								
Temperature (C)	**0**	**10**	**20**	**30**	**40**	**50**	**60**	**70**	**80**
350	-2.907E-07	3.400E-08	4.462E-07	2.396E-07	-4.705E-06	1.155E-05	9.255E-06	6.020E-06	3.706E-06
450	-6.485E-08	4.958E-07	-2.341E-06	-1.692E-06	-3.464E-06	1.217E-05	7.915E-06	4.733E-06	8.181E-06
550	-1.165E-07	-8.807E-07	-2.668E-06	7.883E-07	7.324E-06	6.760E-06	2.574E-06	7.334E-06	5.113E-06
650	8.993E-09	6.427E-08	-3.029E-06	1.916E-06	4.031E-06	3.242E-06	3.287E-06	4.605E-06	4.259E-06

Appendix B

Look up Tables for Summary Model Parameters for Chapter IV, Equation 4

1 Hz Frequency

β_1	Pressure (psig)								
Temperature (C)	**0**	**10**	**20**	**30**	**40**	**50**	**60**	**70**	**80**
350	-7.685E-02	-4.243E-01	-5.699E-01	-6.706E-01	-1.169E+00	-1.281E+00	-1.638E+00	-2.027E+00	-2.411E+00
450	-1.150E-01	-1.988E-01	-3.843E-01	-4.709E-01	-6.244E-01	-8.127E-01	-9.948E-01	-1.215E+00	-5.729E-01
550	-8.839E-02	-1.765E-01	-2.412E-01	-3.302E-01	-4.170E-01	-5.512E-01	-6.946E-01	-8.389E-01	-9.738E-01
650	-6.722E-02	-1.245E-01	-1.829E-01	-2.504E-01	-3.338E-01	-4.129E-01	-5.182E-01	-6.138E-01	-7.320E-01

β_2	Pressure (psig)								
Temperature (C)	**0**	**10**	**20**	**30**	**40**	**50**	**60**	**70**	**80**
350	5.604E-01	2.080E+00	2.917E+00	3.563E+00	5.715E+00	6.428E+00	8.068E+00	9.867E+00	1.162E+01
450	6.486E-01	1.176E+00	2.136E+00	2.675E+00	3.496E+00	4.483E+00	5.435E+00	6.567E+00	3.917E+00
550	5.271E-01	1.065E+00	1.500E+00	2.035E+00	2.571E+00	3.330E+00	4.130E+00	4.932E+00	5.697E+00
650	4.343E-01	8.229E-01	1.223E+00	1.656E+00	2.180E+00	2.682E+00	3.315E+00	3.900E+00	4.600E+00

β_3	Pressure (psig)								
Temperature (C)	**0**	**10**	**20**	**30**	**40**	**50**	**60**	**70**	**80**
350	-9.345E-01	-3.148E+00	-4.600E+00	-5.784E+00	-8.848E+00	-1.015E+01	-1.260E+01	-1.530E+01	-1.790E+01
450	-1.056E+00	-2.062E+00	-3.668E+00	-4.691E+00	-6.094E+00	-7.755E+00	-9.351E+00	-1.122E+01	-7.832E+00
550	-9.257E-01	-1.962E+00	-2.848E+00	-3.868E+00	-4.902E+00	-6.275E+00	-7.707E+00	-9.138E+00	-1.052E+01
650	-8.293E-01	-1.652E+00	-2.498E+00	-3.380E+00	-4.426E+00	-5.431E+00	-6.646E+00	-7.780E+00	-9.099E+00

β_4	Pressure (psig)								
Temperature (C)	**0**	**10**	**20**	**30**	**40**	**50**	**60**	**70**	**80**
350	4.311E-01	1.479E+00	2.252E+00	2.903E+00	4.325E+00	5.044E+00	6.224E+00	7.530E+00	8.770E+00
450	4.897E-01	1.056E+00	1.897E+00	2.475E+00	3.216E+00	4.088E+00	4.921E+00	5.885E+00	4.552E+00
550	4.452E-01	1.035E+00	1.553E+00	2.131E+00	2.719E+00	3.472E+00	4.251E+00	5.026E+00	5.778E+00
650	4.146E-01	9.056E-01	1.412E+00	1.927E+00	2.534E+00	3.113E+00	3.801E+00	4.441E+00	5.177E+00

2 Hz Frequency

β_1	Pressure (psig)								
Temperature (C)	**0**	**10**	**20**	**30**	**40**	**50**	**60**	**70**	**80**
350	-1.212E-01	-5.091E-01	-7.667E-01	-1.591E+00	-1.618E+00	-2.046E+00	-1.986E+00	-2.012E+00	-2.069E+00
450	-2.265E-01	-5.245E-01	-6.266E-01	-8.738E-01	-1.053E+00	-1.438E+00	-1.008E+00	-1.151E+00	-1.337E+00
550	-1.488E-01	-3.027E-01	-4.203E-01	-5.388E-01	-7.840E-01	-5.632E-01	-6.675E-01	-7.826E-01	-8.526E-01
650	-1.340E-01	-2.144E-01	-3.720E-01	-4.022E-01	-5.505E-01	-4.221E-01	-4.718E-01	-5.219E-01	-5.952E-01

β_2	Pressure (psig)								
Temperature (C)	**0**	**10**	**20**	**30**	**40**	**50**	**60**	**70**	**80**
350	9.498E-01	2.817E+00	4.291E+00	8.036E+00	8.527E+00	1.067E+01	1.097E+01	1.142E+01	1.202E+01
450	1.226E+00	2.838E+00	3.618E+00	4.978E+00	6.068E+00	8.082E+00	6.480E+00	7.410E+00	8.550E+00
550	9.211E-01	1.873E+00	2.681E+00	3.438E+00	4.856E+00	4.032E+00	4.749E+00	5.543E+00	6.106E+00
650	8.506E-01	1.462E+00	2.432E+00	2.773E+00	3.738E+00	3.254E+00	3.688E+00	4.125E+00	4.692E+00

β_3	Pressure (psig)								
Temperature (C)	**0**	**10**	**20**	**30**	**40**	**50**	**60**	**70**	**80**
350	-1.522E+00	-4.370E+00	-6.849E+00	-1.233E+01	-1.345E+01	-1.678E+01	-1.824E+01	-1.928E+01	-2.058E+01
450	-1.860E+00	-4.561E+00	-6.120E+00	-8.432E+00	-1.041E+01	-1.369E+01	-1.215E+01	-1.395E+01	-1.608E+01
550	-1.568E+00	-3.340E+00	-4.944E+00	-6.394E+00	-8.941E+00	-8.291E+00	-9.766E+00	-1.141E+01	-1.267E+01
650	-1.527E+00	-2.836E+00	-4.691E+00	-5.545E+00	-7.454E+00	-7.209E+00	-8.268E+00	-9.334E+00	-1.062E+01

β_4	Pressure (psig)								
Temperature (C)	**0**	**10**	**20**	**30**	**40**	**50**	**60**	**70**	**80**
350	7.354E-01	2.152E+00	3.474E+00	6.113E+00	6.828E+00	8.499E+00	9.751E+00	1.043E+01	1.126E+01
450	8.632E-01	2.290E+00	3.218E+00	4.463E+00	5.575E+00	7.282E+00	7.034E+00	8.114E+00	9.364E+00
550	7.748E-01	1.773E+00	2.719E+00	3.557E+00	4.972E+00	5.041E+00	5.947E+00	6.969E+00	7.789E+00
650	7.670E-01	1.560E+00	2.627E+00	3.179E+00	4.294E+00	4.524E+00	5.235E+00	5.953E+00	6.785E+00

3 Hz Frequency

β_1	Pressure (psig)								
Temperature (C)	**0**	**10**	**20**	**30**	**40**	**50**	**60**	**70**	**80**
350	-4.558E-01	-1.076E+00	-6.276E-01	-1.903E+00	-2.314E+00	-1.699E+00	-1.542E+00	-3.036E+00	-3.250E+00
450	-2.617E-01	-5.397E-01	-7.751E-01	-8.720E-01	-1.017E+00	-1.130E+00	-1.473E+00	-1.738E+00	-2.042E+00
550	-1.585E-01	-2.859E-01	-5.865E-01	-6.888E-01	-8.001E-01	-7.496E-01	-1.039E+00	-1.146E+00	-1.209E+00
650	-1.262E-01	-2.777E-01	-4.393E-01	-4.259E-01	-4.768E-01	-5.456E-01	-6.697E-01	-7.679E-01	-8.509E-01

β_2	Pressure (psig)								
Temperature (C)	**0**	**10**	**20**	**30**	**40**	**50**	**60**	**70**	**80**
350	2.173E+00	5.290E+00	4.226E+00	9.923E+00	1.196E+01	1.005E+01	9.999E+00	1.702E+01	1.827E+01
450	1.460E+00	3.082E+00	4.606E+00	5.420E+00	6.414E+00	7.350E+00	9.371E+00	1.094E+01	1.279E+01
550	1.035E+00	1.966E+00	3.707E+00	4.393E+00	5.304E+00	5.413E+00	7.213E+00	8.044E+00	8.636E+00
650	8.894E-01	1.916E+00	2.965E+00	3.096E+00	3.691E+00	4.282E+00	5.205E+00	5.984E+00	6.698E+00

β_3	Pressure (psig)								
Temperature (C)	**0**	**10**	**20**	**30**	**40**	**50**	**60**	**70**	**80**
350	-2.751E+00	-7.507E+00	-6.872E+00	-1.498E+01	-1.802E+01	-1.600E+01	-1.652E+01	-2.794E+01	-3.000E+01
450	-2.076E+00	-4.807E+00	-7.541E+00	-9.445E+00	-1.091E+01	-1.335E+01	-1.697E+01	-1.977E+01	-2.319E+01
550	-1.645E+00	-3.441E+00	-6.476E+00	-7.724E+00	-9.589E+00	-1.078E+01	-1.424E+01	-1.603E+01	-1.738E+01
650	-1.538E+00	-3.519E+00	-5.511E+00	-5.953E+00	-7.868E+00	-9.238E+00	-1.126E+01	-1.302E+01	-1.472E+01

β_4	Pressure (psig)								
Temperature (C)	**0**	**10**	**20**	**30**	**40**	**50**	**60**	**70**	**80**
350	1.216E+00	3.616E+00	3.739E+00	7.604E+00	9.162E+00	8.576E+00	9.139E+00	1.537E+01	1.653E+01
450	9.843E-01	2.469E+00	4.041E+00	5.404E+00	6.082E+00	7.924E+00	1.004E+01	1.166E+01	1.371E+01
550	8.249E-01	1.883E+00	3.584E+00	4.323E+00	5.485E+00	6.745E+00	8.856E+00	1.005E+01	1.095E+01
650	7.867E-01	1.942E+00	3.120E+00	3.452E+00	5.061E+00	5.985E+00	7.318E+00	8.505E+00	9.690E+00

4 Hz Frequency

β_1	Pressure (psig)								
Temperature (C)	**0**	**10**	**20**	**30**	**40**	**50**	**60**	**70**	**80**
350	-1.281E+00	3.443E-01	-1.296E+00	-9.147E-01	-2.401E+00	-3.964E+00	-3.775E+00	-5.449E+00	-5.347E+00
450	-5.242E-01	-4.088E-01	-1.352E-01	-7.157E-01	-1.225E+00	-1.836E+00	-1.796E+00	-2.427E+00	-2.833E+00
550	-1.280E-01	-4.471E-01	-6.901E-01	-6.851E-01	-4.247E-01	-1.180E+00	-1.269E+00	-1.544E+00	-1.524E+00
650	-1.858E-01	-2.727E-01	-4.679E-01	-3.476E-01	-5.264E-01	-7.130E-01	-8.417E-01	-9.122E-01	-1.072E+00

β_2	Pressure (psig)								
Temperature (C)	**0**	**10**	**20**	**30**	**40**	**50**	**60**	**70**	**80**
350	5.300E+00	-1.380E-01	7.311E+00	6.319E+00	1.318E+01	2.052E+01	2.046E+01	2.831E+01	2.832E+01
450	2.635E+00	2.788E+00	2.091E+00	4.867E+00	7.587E+00	1.122E+01	1.145E+01	1.497E+01	1.737E+01
550	9.626E-01	2.907E+00	4.370E+00	4.746E+00	3.583E+00	8.066E+00	8.817E+00	1.065E+01	1.087E+01
650	1.209E+00	2.046E+00	3.177E+00	2.811E+00	4.045E+00	5.524E+00	6.555E+00	7.207E+00	8.430E+00

β_3	Pressure (psig)								
Temperature (C)	**0**	**10**	**20**	**30**	**40**	**50**	**60**	**70**	**80**
350	-6.331E+00	-9.893E-02	-1.070E+01	-9.646E+00	-2.032E+01	-3.131E+01	-3.207E+01	-4.376E+01	-4.414E+01
450	-3.497E+00	-4.291E+00	-3.655E+00	-7.660E+00	-1.197E+01	-1.925E+01	-2.008E+01	-2.614E+01	-3.035E+01
550	-1.369E+00	-4.719E+00	-7.150E+00	-8.647E+00	-6.082E+00	-1.523E+01	-1.680E+01	-2.040E+01	-2.117E+01
650	-1.846E+00	-3.579E+00	-5.405E+00	-4.992E+00	-7.273E+00	-1.142E+01	-1.372E+01	-1.521E+01	-1.789E+01

β_4	Pressure (psig)								
Temperature (C)	**0**	**10**	**20**	**30**	**40**	**50**	**60**	**70**	**80**
350	2.725E+00	5.330E-01	5.643E+00	5.452E+00	1.113E+01	1.670E+01	1.766E+01	2.352E+01	2.406E+01
450	1.684E+00	2.399E+00	2.398E+00	4.433E+00	6.802E+00	1.148E+01	1.227E+01	1.576E+01	1.823E+01
550	7.274E-01	2.633E+00	4.022E+00	5.387E+00	3.740E+00	9.687E+00	1.077E+01	1.308E+01	1.380E+01
650	9.476E-01	2.056E+00	3.058E+00	3.015E+00	4.381E+00	7.680E+00	9.273E+00	1.033E+01	1.218E+01

5 Hz Frequency

β_1	Pressure (psig)								
Temperature (C)	**0**	**10**	**20**	**30**	**40**	**50**	**60**	**70**	**80**
350	2.152E-01	-9.177E-02	4.118E+00	2.675E+00	3.694E+00	-1.927E+00	-4.886E+00	-6.956E+00	-6.447E+00
450	-2.299E-02	-4.651E-01	1.451E+00	-1.813E+00	6.992E-01	-1.673E+00	-2.552E+00	-2.673E+00	-3.847E+00
550	-4.110E-01	-2.589E-01	-7.758E-01	-9.691E-01	-1.127E+00	-1.131E+00	-1.385E+00	-1.721E+00	-1.899E+00
650	-4.245E-01	-8.842E-02	-6.691E-01	-4.754E-01	-6.570E-01	-7.485E-01	-9.993E-01	-3.246E-01	-1.267E+00

β_2	Pressure (psig)								
Temperature (C)	**0**	**10**	**20**	**30**	**40**	**50**	**60**	**70**	**80**
350	4.839E-02	2.028E+00	-1.388E+01	-7.919E+00	-1.210E+01	1.204E+01	2.599E+01	3.599E+01	3.438E+01
450	6.066E-01	3.158E+00	-4.716E+00	1.032E+01	-1.106E+00	1.069E+01	1.568E+01	1.663E+01	2.291E+01
550	2.284E+00	2.082E+00	4.938E+00	6.343E+00	7.602E+00	8.091E+00	9.700E+00	1.199E+01	1.330E+01
650	2.472E+00	1.118E+00	4.207E+00	3.663E+00	5.079E+00	5.944E+00	7.773E+00	4.003E+00	9.915E+00

β_3	Pressure (psig)								
Temperature (C)	**0**	**10**	**20**	**30**	**40**	**50**	**60**	**70**	**80**
350	1.590E-01	-2.764E+00	1.765E+01	1.023E+01	1.645E+01	-1.832E+01	-3.937E+01	-5.463E+01	-5.271E+01
450	-4.193E-01	-4.319E+00	6.744E+00	-1.604E+01	2.204E+00	-1.765E+01	-2.635E+01	-2.800E+01	-3.843E+01
550	-3.008E+00	-2.967E+00	-7.453E+00	-1.077E+01	-1.340E+01	-1.483E+01	-1.759E+01	-2.218E+01	-2.465E+01
650	-3.663E+00	-1.521E+00	-6.390E+00	-6.641E+00	-9.737E+00	-1.173E+01	-1.562E+01	-6.046E+00	-2.013E+01

β_4	Pressure (psig)								
Temperature (C)	**0**	**10**	**20**	**30**	**40**	**50**	**60**	**70**	**80**
350	3.121E-01	1.955E+00	-6.373E+00	-3.013E+00	-5.661E+00	1.120E+01	2.192E+01	2.985E+01	2.946E+01
450	3.686E-01	2.497E+00	-2.284E+00	9.203E+00	9.418E-02	1.113E+01	1.629E+01	1.746E+01	2.329E+01
550	1.538E+00	1.811E+00	4.301E+00	6.774E+00	8.721E+00	1.007E+01	1.167E+01	1.482E+01	1.644E+01
650	1.934E+00	9.531E-01	3.640E+00	4.506E+00	6.751E+00	8.294E+00	1.106E+01	4.106E+00	1.421E+01

6 Hz Frequency

β_1	Pressure (psig)								
Temperature (C)	**0**	**10**	**20**	**30**	**40**	**50**	**60**	**70**	**80**
350	-4.667E-01	3.839E+00	2.863E+00	8.792E+00	6.156E+00	-5.679E+00	-7.862E+00	-5.795E+00	-9.344E+00
450	-1.803E+00	4.289E-01	1.483E+00	1.491E+00	1.140E+00	-2.293E+00	-3.353E+00	-3.028E+00	-4.488E+00
550	-7.003E-01	3.226E-01	-9.764E-01	-1.590E+00	-6.887E-01	-1.368E+00	-1.621E+00	-1.814E+00	-1.935E+00
650	-3.320E-01	-3.924E-01	-3.615E-01	-5.124E-01	-9.206E-01	-9.158E-01	1.297E+00	-1.160E+00	-1.220E+00

β_2	Pressure (psig)								
Temperature (C)	**0**	**10**	**20**	**30**	**40**	**50**	**60**	**70**	**80**
350	2.278E+00	-1.340E+01	-8.116E+00	-3.249E+01	-2.267E+01	2.919E+01	3.981E+01	3.081E+01	4.830E+01
450	8.151E+00	-8.660E-01	-4.220E+00	-5.074E+00	-3.250E+00	1.401E+01	1.990E+01	1.869E+01	2.674E+01
550	3.711E+00	-5.872E-01	5.688E+00	9.936E+00	5.345E+00	9.540E+00	1.128E+01	1.265E+01	1.372E+01
650	2.050E+00	2.772E+00	2.435E+00	3.923E+00	6.860E+00	7.087E+00	-4.739E+00	9.131E+00	9.725E+00

β_3	Pressure (psig)								
Temperature (C)	**0**	**10**	**20**	**30**	**40**	**50**	**60**	**70**	**80**
350	-1.640E+00	1.815E+01	1.026E+01	4.416E+01	3.320E+01	-4.216E+01	-5.828E+01	-4.470E+01	-7.218E+01
450	-1.043E+01	2.404E+00	6.236E+00	9.477E+00	7.247E+00	-2.189E+01	-3.186E+01	-2.998E+01	-4.372E+01
550	-4.828E+00	1.727E+00	-7.271E+00	-1.649E+01	-8.603E+00	-1.639E+01	-1.957E+01	-2.197E+01	-2.412E+01
650	-2.639E+00	-3.743E+00	-2.175E+00	-6.433E+00	-1.269E+01	-1.321E+01	1.039E+01	-1.731E+01	-1.837E+01

β_4	Pressure (psig)								
Temperature (C)	**0**	**10**	**20**	**30**	**40**	**50**	**60**	**70**	**80**
350	9.603E-01	-6.924E+00	-2.584E+00	-1.747E+01	-1.310E+01	2.319E+01	3.169E+01	2.555E+01	4.024E+01
450	5.012E+00	-6.445E-01	-1.541E+00	-3.520E+00	-2.168E+00	1.390E+01	1.984E+01	1.932E+01	2.733E+01
550	2.515E+00	-3.883E-01	4.156E+00	1.041E+01	6.530E+00	1.150E+01	1.367E+01	1.530E+01	1.700E+01
650	1.470E+00	2.274E+00	1.290E+00	4.751E+00	9.252E+00	9.901E+00	-4.420E+00	1.292E+01	1.367E+01

7 Hz Frequency

β_1	Pressure (psig)								
Temperature (C)	**0**	**10**	**20**	**30**	**40**	**50**	**60**	**70**	**80**
350	-1.106E+01	3.963E+00	-1.601E+00	1.450E+01	1.719E+01	-9.188E+00	-7.308E+00	-8.555E+00	-8.708E+00
450	3.106E-01	6.145E-01	-6.403E-01	3.404E+00	-1.248E+00	-4.044E+00	-3.095E+00	-3.384E+00	-4.201E+00
550	-1.024E+00	3.549E-01	-1.231E+00	2.594E+00	-1.031E+00	-1.745E+00	-1.509E+00	-1.803E+00	-2.756E+00
650	-1.084E-01	5.326E-01	-8.599E-01	1.955E+00	-5.344E-01	-8.118E-01	-1.083E+00	-1.223E+00	-1.375E+00

β_2	Pressure (psig)								
Temperature (C)	**0**	**10**	**20**	**30**	**40**	**50**	**60**	**70**	**80**
350	4.259E+01	-1.389E+01	1.019E+01	-5.587E+01	-6.835E+01	4.519E+01	3.849E+01	4.515E+01	4.608E+01
450	-7.753E-01	-1.178E+00	5.824E+00	-1.406E+01	8.588E+00	2.310E+01	1.905E+01	2.053E+01	2.538E+01
550	5.172E+00	-8.099E-01	6.885E+00	-1.169E+01	7.314E+00	1.150E+01	1.062E+01	1.269E+01	1.853E+01
650	1.051E+00	-1.773E+00	4.875E+00	-9.353E+00	4.372E+00	6.441E+00	8.355E+00	9.606E+00	1.093E+01

β_3	Pressure (psig)								
Temperature (C)	**0**	**10**	**20**	**30**	**40**	**50**	**60**	**70**	**80**
350	-5.169E+01	1.989E+01	-1.407E+01	7.754E+01	9.759E+01	-6.407E+01	-5.608E+01	-6.636E+01	-6.700E+01
450	2.581E+00	3.100E+00	-9.073E+00	2.494E+01	-1.187E+01	-3.552E+01	-2.951E+01	-3.092E+01	-3.933E+01
550	-6.469E+00	3.068E+00	-7.856E+00	2.236E+01	-1.104E+01	-1.815E+01	-1.669E+01	-2.056E+01	-3.104E+01
650	-7.497E-01	4.236E+00	-4.985E+00	1.917E+01	-6.448E+00	-1.066E+01	-1.415E+01	-1.674E+01	-1.951E+01

β_4	Pressure (psig)								
Temperature (C)	**0**	**10**	**20**	**30**	**40**	**50**	**60**	**70**	**80**
350	2.186E+01	-7.586E+00	8.919E+00	-3.203E+01	-4.153E+01	3.458E+01	3.262E+01	3.839E+01	3.912E+01
450	-8.603E-01	-5.472E-01	6.693E+00	-1.096E+01	8.907E+00	2.200E+01	1.997E+01	2.070E+01	2.609E+01
550	3.406E+00	-9.989E-01	4.554E+00	-1.049E+01	8.586E+00	1.291E+01	1.275E+01	1.566E+01	2.192E+01
650	6.671E-01	-1.684E+00	3.053E+00	-9.504E+00	5.721E+00	8.943E+00	1.118E+01	1.326E+01	1.553E+01

8 Hz Frequency

β_1	Pressure (psig)								
Temperature (C)	**0**	**10**	**20**	**30**	**40**	**50**	**60**	**70**	**80**
350	-7.840E+00	-7.439E-01	-1.351E+00	2.091E+01	-9.168E+00	-9.768E+00	-1.839E+01	-5.847E+00	-9.460E+00
450	-2.152E+00	1.168E+00	6.992E-01	1.360E+00	-1.754E+00	-1.997E+00	-2.405E+00	-4.561E+00	-4.904E+00
550	-1.210E-01	1.722E+00	2.020E+00	-1.951E+00	-7.544E-01	-5.274E-01	-1.245E+00	-2.397E+00	-1.822E+00
650	2.161E-01	1.576E+00	3.988E-01	-6.600E-01	-3.257E-01	-7.551E-01	-1.034E+00	-1.141E+00	-1.214E+00

β_2	Pressure (psig)								
Temperature (C)	**0**	**10**	**20**	**30**	**40**	**50**	**60**	**70**	**80**
350	2.947E+01	6.094E+00	1.055E+01	-7.951E+01	4.557E+01	4.857E+01	8.878E+01	3.333E+01	5.018E+01
450	9.293E+00	-3.668E+00	-9.996E-01	-5.189E+00	1.107E+01	1.331E+01	1.540E+01	2.677E+01	2.914E+01
550	1.168E+00	-7.046E+00	-9.004E+00	1.180E+01	5.956E+00	4.676E+00	9.189E+00	1.615E+01	1.325E+01
650	-6.680E-01	-7.023E+00	-1.762E+00	4.768E+00	2.945E+00	6.043E+00	7.951E+00	8.901E+00	9.776E+00

β_3	Pressure (psig)								
Temperature (C)	**0**	**10**	**20**	**30**	**40**	**50**	**60**	**70**	**80**
350	-3.315E+01	-6.645E+00	-1.516E+01	1.081E+02	-6.426E+01	-6.788E+01	-1.282E+02	-4.671E+01	-7.104E+01
450	-1.017E+01	7.902E+00	3.524E+00	1.413E+01	-1.424E+01	-1.855E+01	-2.106E+01	-3.925E+01	-4.308E+01
550	-4.019E-02	1.335E+01	1.867E+01	-1.736E+01	-7.632E+00	-4.322E+00	-1.239E+01	-2.475E+01	-1.923E+01
650	2.805E+00	1.371E+01	7.675E+00	-5.991E+00	-2.169E+00	-8.335E+00	-1.148E+01	-1.307E+01	-1.471E+01

β_4	Pressure (psig)								
Temperature (C)	**0**	**10**	**20**	**30**	**40**	**50**	**60**	**70**	**80**
350	1.372E+01	4.661E+00	1.061E+01	-4.390E+01	3.535E+01	3.775E+01	6.857E+01	3.045E+01	4.293E+01
450	4.782E+00	-2.647E+00	2.932E-01	-5.304E+00	1.094E+01	1.446E+01	1.635E+01	2.648E+01	2.938E+01
550	4.604E-01	-5.810E+00	-8.545E+00	1.205E+01	7.773E+00	6.052E+00	1.139E+01	1.893E+01	1.638E+01
650	-1.190E+00	-6.409E+00	-3.626E+00	5.495E+00	3.785E+00	8.258E+00	1.029E+01	1.170E+01	1.322E+01

9 Hz Frequency

β_1	Pressure (psig)								
Temperature (C)	**0**	**10**	**20**	**30**	**40**	**50**	**60**	**70**	**80**
350	3.130E-01	9.330E+00	2.141E+01	1.037E+01	-9.251E+00	-1.119E+01	-7.946E+00	-2.094E+00	-2.868E+00
450	2.664E+00	5.611E+00	-2.118E+00	-5.586E+00	3.072E-01	-2.873E+00	-1.558E+00	-3.650E-01	-3.725E+00
550	2.163E-01	4.178E+00	1.403E-01	-7.186E-02	2.472E-01	-6.744E-01	-1.949E+00	-9.604E-01	-3.252E+00
650	2.239E-02	1.888E+00	-9.840E-01	-3.218E-02	-9.637E-01	-8.165E-01	-1.032E+00	-1.438E+00	-1.279E+00

β_2	Pressure (psig)								
Temperature (C)	**0**	**10**	**20**	**30**	**40**	**50**	**60**	**70**	**80**
350	-1.072E+00	-3.275E+01	-8.392E+01	-3.904E+01	4.792E+01	5.471E+01	4.262E+01	1.566E+01	2.048E+01
450	-1.055E+01	-2.244E+01	1.355E+01	2.887E+01	8.118E-01	1.711E+01	1.084E+01	5.622E+00	2.337E+01
550	-2.465E-01	-1.851E+01	3.437E-01	1.902E+00	-1.390E-01	5.123E+00	1.304E+01	7.755E+00	2.112E+01
650	4.954E-01	-8.231E+00	6.544E+00	6.100E-01	6.836E+00	6.289E+00	8.211E+00	1.081E+01	9.921E+00

β_3	Pressure (psig)								
Temperature (C)	**0**	**10**	**20**	**30**	**40**	**50**	**60**	**70**	**80**
350	5.716E+00	4.381E+01	1.177E+02	5.960E+01	-6.820E+01	-7.457E+01	-5.853E+01	-1.592E+01	-2.371E+01
450	1.750E+01	3.500E+01	-1.964E+01	-4.025E+01	4.120E+00	-2.172E+01	-1.065E+01	-2.024E+00	-3.081E+01
550	2.538E+00	3.191E+01	3.389E+00	3.956E-01	5.754E+00	-2.406E+00	-1.709E+01	-6.635E+00	-3.031E+01
650	1.262E+00	1.618E+01	-8.755E+00	3.925E+00	-8.306E+00	-6.913E+00	-1.097E+01	-1.483E+01	-1.201E+01

β_4	Pressure (psig)								
Temperature (C)	**0**	**10**	**20**	**30**	**40**	**50**	**60**	**70**	**80**
350	-2.149E+00	-1.591E+01	-4.961E+01	-2.332E+01	3.915E+01	4.242E+01	3.672E+01	1.604E+01	2.171E+01
450	-7.321E+00	-1.454E+01	1.355E+01	2.360E+01	2.420E+00	1.687E+01	1.178E+01	8.357E+00	2.442E+01
550	-4.156E-01	-1.467E+01	2.343E-01	3.745E+00	7.397E-01	5.352E+00	1.524E+01	9.519E+00	2.367E+01
650	-1.698E-02	-7.125E+00	7.273E+00	-1.902E-02	8.401E+00	8.266E+00	1.192E+01	1.400E+01	1.228E+01

10 Hz Frequency

β_1	Pressure (psig)								
Temperature (C)	**0**	**10**	**20**	**30**	**40**	**50**	**60**	**70**	**80**
350	-4.472E+00	1.476E+01	3.100E+01	5.147E+00	5.232E+00	9.887E+00	1.442E+01	-3.039E+00	-3.807E+00
450	7.490E+00	2.762E+00	-1.735E+00	3.816E+00	1.491E+00	-9.646E-01	-2.050E+00	-3.992E-01	-2.426E+00
550	1.485E+00	-8.294E-02	1.430E+00	3.426E-01	-7.664E-01	-1.888E-01	-2.391E-01	-1.281E+00	-5.592E-01
650	1.247E+00	4.871E+00	-6.161E-01	2.320E-01	4.487E-01	-6.803E-02	-1.384E+00	-1.071E+00	-1.675E+00

β_2	Pressure (psig)								
Temperature (C)	**0**	**10**	**20**	**30**	**40**	**50**	**60**	**70**	**80**
350	1.792E+01	-5.395E+01	-1.202E+02	-1.516E+01	-1.684E+01	-3.589E+01	-5.804E+01	2.032E+01	2.386E+01
450	-3.082E+01	-8.731E+00	1.283E+01	-1.701E+01	-5.354E+00	7.148E+00	1.354E+01	5.938E+00	1.511E+01
550	-5.755E+00	2.403E+00	-5.881E+00	-1.152E+00	5.049E+00	2.075E+00	3.375E+00	9.524E+00	5.190E+00
650	-5.286E+00	-2.361E+01	4.500E+00	-7.947E-01	-2.113E+00	1.519E+00	1.005E+01	8.142E+00	1.228E+01

β_3	Pressure (psig)								
Temperature (C)	**0**	**10**	**20**	**30**	**40**	**50**	**60**	**70**	**80**
350	-1.773E+01	7.313E+01	1.648E+02	2.327E+01	2.819E+01	5.549E+01	9.359E+01	-1.963E+01	-2.325E+01
450	4.634E+01	1.502E+01	-1.912E+01	3.396E+01	1.654E+01	-1.972E+00	-1.283E+01	2.334E-01	-1.108E+01
550	1.116E+01	-1.899E+00	1.378E+01	9.048E+00	-8.155E-01	5.610E+00	2.729E+00	-7.233E+00	2.947E+00
650	1.072E+01	4.285E+01	-4.081E+00	7.316E+00	1.123E+01	4.551E+00	-1.151E+01	-6.269E+00	-1.372E+01

β_4	Pressure (psig)								
Temperature (C)	**0**	**10**	**20**	**30**	**40**	**50**	**60**	**70**	**80**
350	7.865E+00	-2.845E+01	-6.814E+01	-3.821E+00	-4.568E+00	-1.579E+01	-3.569E+01	1.949E+01	2.250E+01
450	-2.008E+01	-4.024E+00	1.522E+01	-1.304E+01	-3.088E+00	6.700E+00	1.481E+01	8.885E+00	1.438E+01
550	-4.227E+00	3.886E+00	-3.580E+00	-1.423E+00	5.002E+00	2.013E+00	5.345E+00	1.156E+01	5.371E+00
650	-4.271E+00	-2.058E+01	5.414E+00	-4.389E-01	-2.582E+00	2.401E+00	1.265E+01	9.482E+00	1.462E+01

Appendix C

List of Publications

A.C.1 Publications Relevant to Dissertation Work

Thomas, S. and Barth, E. J. (2022) Multi-Stage Stirling Thermocompressor: Experimental and Analytical Proof-of-Concept, ***In Preparation for Applied Energy***

Thomas, S. and Barth, E. J. (2022) Active Stirling Thermocompressor: Enthalpy, Efficiency and Dead Volume as a Function of Displacer Motion Profile, ***In Preparation for Applied Energy***

Thomas, S. and Barth, E. J. (2022) Active Stirling Thermocompressor: Modelling and Effects of Controlled Displacer Motion Profile on Work Output, ***Submitted to Applied Energy***

Thomas, S, and Barth, E J. (2019) *Stirling Thermocompressor: Lumped Parameter Modeling and Experimental impact of Displacer Motion Profile on Work Output*. Proceedings of the ASME/BATH 2019 Symposium on Fluid Power and Motion Control. ASME/BATH 2019 Symposium on Fluid Power and Motion Control. Longboat Key, Florida, USA. V001T01A040. ASME. https ://doi.org/10.1115/FPMC2019-1683

Thomas, S, and Barth, E J. (2017) *Multi-Stage Modeling of a Stirling Thermocompressor*. Proceedings of the ASME/BATH 2017 Symposium on Fluid Power and Motion Control, ASME/BATH 2017 Symposium on Fluid Power and Motion Control. Sarasota, Florida, USA. V001T01A060. ASME. https://doi.org/10.1115/FPMC2O17-4320

A.C.2 Other Publications

Howard, J. T., **Thomas, S**, Gallentine, J. C., and Barth, E. J. (2021) *Hydraulic Test Stand to Model Circulatory System Dynamics for Artificial Heart Evaluation. Proceedings of the ASME/BATH 2021 Symposium on Fluid Power and Motion Control. ASME/BATH 2021 Symposium on Fluid Power and Motion Control.* Virtual, Online. V001T01A052. ASME. https://doi.org/10.1115/FPMC2021-69806

Lli, M, Chen, Y, Slepian, M, Howard, J, **Thomas, S,** & Barth, E. (2021). Design, Modeling, and Experimental Characterization of A Valveless Pulsatile Flow Mechanical Circulatory Support Device. *Journal of Medical Devices. 15*. 10.1115/1.4049560.

Cummins, J. J., Nash, C. J., **Thomas, S.**, Justice, A., Mahadevan, S., Adams, D. E., and Barth, E. J. (2017) Energy conservation in industrial pneumatics: A state model for predicting energetic savings using a novel pneumatic strain energy accumulator, *Applied Energy, Volume 198,* Pages 239-249, lSSN 0306-2619, https://doi.org/10.1016/j.apenergy.2017.04.036.

Cummins, J., **Thomas, S**., Nash, C.J., Mahadevan, S., Adams, D., and Barth, E. (2017). Experimental evaluation of the efficiency of a pneumatic strain energy accumulator. *International Journal of Fluid Power, 18,* 167 - 180.

References

[1] Johnson, I., Choate, W. and Davidson, A. (2008). *Waste Heat Recovery. Technology and Opportunities in U.S. Industry*. U.S. Department of Energy Industrial Technologies Program, Laurel, MD. [online] Available at: <https://www1.eere.energy.gov/manufacturing/intensiveprocesses/pdfs/waste_heat_recovery.pdf> [Accessed 1 April 2022].

[2] Love, Lonnie, et al (2012) *Estimating the Impact (Energy, Emissions and Economics) of the U.S. Fluid Power Industry*. Oak Ridge National Laboratory, United States

[3] Stirling, R. (1816) *Regenerator and Hot Air Engines* (Patent No. 4081)

[4] Ernst, W. D. and Shaltens, R. K. (1997) Automotive Stirling Engine Development Project (MTI Report 91TR15) U.S. Department of Energy

[5] Radebaugh, R. (2004), *Refrigeration for Superconductors*, Proceedings of the IEEE, [online], https://doi.org/10.1109/JPROC.2004.833678 (Accessed July 29, 2021)

[6] Zayed, M. E., Zhao, J., Elsheikh, A. H., Li, W., Sadek, S., and Aboelmaaref, M. M. (2021) A comprehensive review on Dish/Stirling concentrated solar power systems: Design, optical and geometrical analyses, thermal performance assessment, and applications. *Journal of Cleaner Production, Volume 283*, 124664, ISSN 0959-6526, https://doi.org/10.1016/j.jclepro.2020.124664.

[7] Gaun, A. A. and Schmautzer, E. (2007) *Biomass-Fuelled Stirling Micro Combined Heat and Power Plants*, 2007 International Conference on Clean Electrical Power, pp. 429-432, doi: 10.1109/ICCEP.2007.384249.

[8] Schreiber, J. G. (2000) *Assessment of the Stirling power option for space science applications*, IEEE Aerospace Conference. Proceedings (Cat. No.00TH8484), pp. 39-46 vol.4, doi: 10.1109/AERO.2000.878363.

[9] Bush, V. (1939) *Apparatus for Compressing Gases* (U.S. Patent No. 2,157,229).

[10] McKellar, S. (2013). Negotiating Risk: The Failed Development of Atomic Hearts in America, 1967–1977. *Technology and Culture, 54(1)*, 1-39. Retrieved July 29, 2021, from http://www.jstor.org/stable/24468138

[11] Kornhauser, A.A. (1996) *Analysis of an idealized Stirling thermocompressor*, IECEC 96. Proceedings of the 31st Intersociety Energy Conversion Engineering Conference, Washington, DC, USA, pp. 1331-1336 vol.2, doi: 10.1109/IECEC.1996.553909.

[12] Wang, J., Xi, X., Luo, K., Chen, L., Wang, J., and Zhou, Y, (2019) Energy and exergy equilibrium analysis of a Stirling-type thermal compressor (STC) – the core part in thermal-driven Vuilleumier machines, *Energy Conversion and Management, Volume 199*, ISSN 0196-8904

[13] Yarger, D. J., et al., (2006) *Experimental Study of a Mesoscale Two-Phase Thermocompressor*, 4th International Energy Conversion Engineering Conference, San Diego, CA.

[14] Hofacker, M., et. al (2013) *Dynamic Simulation and Experimental Validation of a Single Stage Thermocompressor for Pneumatic Ankle-Foot Orthosis*, Proceedings of the 25th Symposium on Fluid Power and Motion Control, Sarasota, FL.

[15] Winkelmann, A. and Barth, E. J. (2016) Design, Modeling, and Experimental Validation of a Stirling Pressurizer With a Controlled Displacer Piston, *IEEE/ASME Transactions on Mechatronics, vol. 21, no. 3*, pp. 1754-1764, doi: 10.1109/TMECH.2015.2499706.

[16] Edwards, M. J. (2005) *Design, Modeling, and Performance of Miniature Reciprocating Thermocompressor.* [Masters of Science thesis, Department of Mechanical Engineering, Oregon State University, OR]

[17] Arques, P. (1997) *Piston movement in thermocompressor*, IECEC-97 Proceedings of the Thirty-Second Intersociety Energy Conversion Engineering Conference (Cat. No.97CH6203), Honolulu, HI, USA, pp. 1003-1008 vol.2, doi: 10.1109/IECEC.1997.661906.

[18] Blagin, E., Dovgyallo, A., and Uglanov, D.A. (2017) Numerical modeling of non-stationary processes in cryogenic mechanical thermocompressor. *International Journal of Mechanical Engineering and Robotics Research. 6.* 258-262. doi: 10.18178/ijmerr.6.4.258-262.

[19] Blagin, E., Dovgyallo, A., and Uglanov, D.A. (2017) *Study of Different Factors Influence on Thermocompressor Performance*. MATEC Web of Conferences. 108. 04001. 10.1051/ matecconf/201710804001.

[20] Pan, C., et al. (2017) Numerical Investigation on the Thermoacoustics Characteristics of Thermal Compressor for the Pulse Tube Cryocooler. *Applied Thermal Engineering, 123*: 234–242.

[21] Wang, J. et al. (2018) Thermal Analysis of Stirling Thermocompressor and Its Prospect to Drive Refrigerator by Using Natural Working Fluid. *Energy Conversion and Management, 177*: 280–291.

[22] Senft, J.R, (1993) *Ringbom Stirling Engines*, New York: Oxford University Press

[23] Karabulut, H., Okur, M., and Onur Ozdemir, A. (2019) Performance prediction of a Martini type of Stirling engine, *Energy Conversion and Management, Volume 179*, Pages 1-12, ISSN 0196-8904, https://doi.org/10.1016/j.enconman.2018.10.059.

[24] Zare, S. and Tavakolpour-Saleh, A. (2020) Free piston Stirling engines: A review. *Int J Energy Res. 44*: 5039– 5070. https://doi.org/10.1002/er.4533

[25] Tavakolpour-Saleh, A.R., Zare, S.H., and Bahreman, H. (2017) A novel active free piston Stirling engine: Modeling, development, and experiment, *Applied Energy, Volume 199*, Pages 400-415, ISSN 0306-2619, https://doi.org/10.1016/j.apenergy.2017.05.059.

[26] Masoumi, A.P., Tavakolpour-Saleh, A.R., and Rahideh, A. (2020) Applying a genetic-fuzzy control scheme to an active free piston Stirling engine: Design and experiment, *Applied Energy, Volume 268*, ISSN 0306-2619, https://doi.org/10.1016/j.apenergy.2020.115045.

[27] Briggs, M.H. (2016) *Improving Free-Piston Stirling Engine Power Density*, Glenn Research Center, Cleveland, OH, Tech. Mem. NASA/TM-2016-219144

[28] Gopal, V.K., Duke, R. and Clucas, D. (2009) *Active Stirling engine*, TENCON 2009 - 2009 IEEE Region 10 Conference, Singapore, pp. 1-6, doi: 10.1109/TENCON.2009.5395807.

[29] Gopal, V.K., Duke, R. and Clucas, D. (2010) *Design and development of a test rig to validate the concept of an Active Stirling Engine*, 2010 20th Australasian Universities Power Engineering Conference, Christchurch, pp. 1-6.

[30] Craun, M., and Bamieh, B. (2015). Optimal Periodic Control of an Ideal Stirling Engine Model. *ASME. J. Dyn. Sys., Meas., Control.*; *137(7)*: 071002. https://doi.org/10.1115/1.4029682

[31] Chen, N. C. J. and Griffin, F. P. (1983) *A Review of Stirling Engine Mathematical Models*, Oak Ridge National Laboratory, Oak Ridge, TN, ORNL/CON-135

[32] Walker, G. (1980) *Stirling Engines*, New York: Oxford University Press

[33] Urieli, I. and Berchowitz, D. M. (1984) *Stirling Cycle Engine Analysis*, Bristol: A. Hilger.

[34] Lin, W.-Y., Wu, X.-H., Yang, J.-L., and Yang, L.-W., (2013) Experimental study and numerical analysis of thermocompressors with annular regenerators, *International Journal of Refrigeration, Volume 36, Issue 4*, Pages 1376-1387, ISSN 0140-7007

[35] Blagin, E., Biryuk, V., Anisimov, M.Y., Shimanov, A.A., and Gorshkalev, A. (2018). *Parametric optimization of the MVC desalination plant with thermomechanical compressor*. IOP Conference Series: Materials Science and Engineering. 339. 012032. 10.1088/1757-899X/339/1/012032.

[36] Blagin, E., Shimanov, A.A., Uglanov, D.A., and Korneev, S.S. (2018). *Possibility of Thermomechanical Compressor Application in Desalination Plants.* IOP Conference Series: Materials Science and Engineering. 302. 012060. 10.1088/1757-899X/302/1/012060.

[37] Cheng, C.-H and Yu, Y.-J. (2010) Numerical model for predicting thermodynamic cycle and thermal efficiency of a beta-type Stirling engine with rhombic-drive mechanism, *Renewable Energy, Volume 35, Issue 11*, Pages 2590-2601, ISSN 0960-1481, https://doi.org/10.1016/j.renene.2010.04.002.

[38] Petersen, H. (1970). *The properties of helium: Density, specific heats, viscosity, and thermal conductivity at pressures from 1 to 100 bar and from room temperature to about 1800 K*. Risø National Laboratory. Denmark. Forskningscenter Risoe. Risoe-R No. 224

[39] Richer, E. and Hurmuzlu, Y. (2000). A High Performance Pneumatic Force Actuator System: Part I—Nonlinear Mathematical Model. *ASME. J. Dyn. Sys., Meas., Control*; *122(3)*: 416–425. https://doi.org/10.1115/1.1286336

[40] Hohenberg, G. (1979) *Advanced Approaches for Heat Transfer Calculations*, SAE Technical Paper 790825, https://doi.org/10.4271/790825.

[41] Bergman, T., Lavine, A., Incropera, F., and DeWitt, D. (2011) *Fundamentals of Heat and Mass Transfer. 7th ed*. New York: Wiley. p.8

[42] Daboussi, Z. (2004) *An inverter-based sensorless controller for free-piston Stirling engines*, 2004 IEEE 35th Annual Power Electronics Specialists Conference (IEEE Cat. No.04CH37551), Aachen, Germany, pp. 1707-1710 Vol.2, doi: 10.1109/PESC.2004.1355683.

[43] Zheng, P., Tong, C., Bai, J., Yu, B., Sui, Y., and Shi, W. (2012) Electromagnetic Design and Control Strategy of an Axially Magnetized Permanent-Magnet Linear Alternator for Free-Piston Stirling Engines, *IEEE Transactions on Industry Applications, vol. 48, no. 6,* pp. 2230-2239, doi: 10.1109/TIA.2012.2226858.

[44] Zheng, P., Yu, B., Zhu, S., Gong, Q. and Liu, J. (2014) *Research on control strategy of free-piston stirling-engine linear-generator system*, 17th International Conference on Electrical Machines and Systems (ICEMS), Hangzhou, pp. 2300-2304, doi: 10.1109/ICEMS.2014.7013882.

[45] Fang, H. W., Herold, K. E., Holland, H. M., and Beach, E. H. (1996) *A novel Stirling engine with am elliptic drive*, IECEC 96. Proceedings of the 31st Intersociety Energy Conversion Engineering Conference, Washington, DC, USA, pp. 1232-1237 vol.2, doi: 10.1109/IECEC.1996.553887.

[46] Lloyd, C. C. (2009) *A Low Temperature Differential Stirling Engine for Power Generation*, [Masters of Engineering thesis, Univ. of Canterbury, 2009]

[47] Wang, K., Sanders, S. R., Dubey, S., Choo, F. H., and Duan, F. (2016) Stirling cycle engines for recovering low and moderate temperature heat: A review, *Renewable and Sustainable Energy Reviews, Volume 62,* Pages 89-108, ISSN 1364-0321

[48] Thomas, S. and Barth, E. J. (2022) Active Stirling Thermocompressor: Modelling and Effects of Controlled Displacer Motion Profile on Work Output, ***Submitted to Applied Energy***

[49] Fischer, F., and Kuehl, H.-D. (2021) Analytical model for an overdriven free-displacer thermocompressor, *Applied Thermal Engineering, Volume 185*, ISSN 1359-4311

[50] Valenti, G., Valenti, A., and Staboli, S. (2019) Proposal of a thermally-driven air compressor for waste heat recovery, *Energy Conversion and Management, Volume 196*, Pages 1113-1125, ISSN 0196-8904, https://doi.org/10.1016/j.enconman.2019.06.072.

[51] Forman, C., Muritala, I.K., Pardemann, R., and Meyer, B. (2016) Estimating the global waste heat potential, *Renewable and Sustainable Energy Reviews, Volume 57*, Pages 1568-1579, ISSN 1364-0321, https://doi.org/10.1016/j.rser.2015.12.192.

[52] Tocci L, Pal T, Pesmazoglou I, and Franchetti B. (2017) Small Scale Organic Rankine Cycle (ORC): A Techno-Economic Review. *Energies. 2017*; 10(4):413. https://doi.org/10.3390/en10040413

[53] Oluleye, G., Jobson, M., and Smith. R. (2015) A hierarchical approach for evaluating and selecting waste heat utilization opportunities, *Energy, Volume 90, Part 1*, Pages 5-23, ISSN 0360-5442, https://doi.org/10.1016/j.energy.2015.05.086.

[54] Jouhara, H., Khordehgah, N., Almahmoud, S., Delpech, B., Chauhan, A., and Tassou, S. A. (2018) Waste heat recovery technologies and applications, *Thermal Science and Engineering Progress, Volume 6*, Pages 268-289, ISSN 2451-9049, https://doi.org/10.1016/j.tsep.2018.04.017.

[55] Liang, X., Wang, X., Shu, G., Wei, H., Tian, H. and Wang, X. (2015), A review and selection of engine waste heat recovery technologies using analytic hierarchy process and grey relational analysis, *Int. J. Energy Res.*, *39*, 453– 471, doi: 10.1002/er.3242

[56] Vittorini, D., Cipollone, R. (2016) Energy saving potential in existing industrial compressors, *Energy, Volume 102*, Pages 502-515, ISSN 0360-5442, https://doi.org/10.1016/j.energy.2016.02.115.

[57] Nourin, F. N., Espindola, J., Selim, O. M., and Amano, R. S. (2021). Energy, Exergy, and Emission Analysis on Industrial Air Compressors. *ASME. J. Energy Resour. Technol. 144(4)*: 042104. https://doi.org/10.1115/1.4051682

[58] Santos Mascarenhas, J., Chowdhury, H., Thirugnanasambandam, M., Chowdhury, T., and Saidur, R. (2019) Energy, exergy, sustainability, and emission analysis of industrial air compressors, *Journal of Cleaner Production, Volume 231*, Pages 183-195, ISSN 0959-6526, https://doi.org/10.1016/j.jclepro.2019.05.158.

[59] Saidur, R., Rahim, N.A., and Hasanuzzaman, M. (2010) A review on compressed-air energy use and energy savings, *Renewable and Sustainable Energy Reviews, Volume 14, Issue 4*, Pages 1135-1153, ISSN 1364-0321, https://doi.org/10.1016/j.rser.2009.11.013.

[60] Shi, Y., Cai, M., Xu, W. et al. (2019) Methods to Evaluate and Measure Power of Pneumatic System and Their Applications. *Chin. J. Mech. Eng. 32, 42*. https://doi.org/10.1186/s10033-019-0354-6

[61] U.S. Department of Energy (2001) *Assessment of the Market for Compressed Air Efficiency Services*, Office of Energy Efficiency and Renewable Energy, https://www.energy.gov/sites/prod/files/2014/05/f16/newmarket5.pdf

[62] Eichhammer, W. and Fleiter, T. (2012). *Energy efficiency in electric motor systems: Technology, saving potentials and policy options for developing countries*. United Nations Industrial Development Organization, Vienna

[63] Kosturkov, R., Nachev, V., and Titova, T. (2019) System Analysis and Opportunities for Optimization of Pneumatic Systems in Manufacturing Plants. *TEM Journal. Volume 8, Issue 3*, Pages 749-763, ISSN 2217-8309, DOI: 10.18421/TEM83-08.

[64] Zhang, B., Liu, M., Li, Y. and Wu, L. (2013) Optimization of an Industrial Air Compressor System, *Energy Engineering, 110:6*,52-64, DOI: 10.1080/01998595.2013.10753695

[65] Compressed Air and Gas Institute (2016). *Air Compressor Selection & Application – ¼ through 30 HP*. [online] CAGI. Available at: < https://www.cagi.org/pdfs/CAGIAirCompressorHP.pdf> [Accessed 25 April 2022].